



UNIVERSIDAD DE MURCIA

FACULTAD DE MEDICINA

Light Scattering Phenomena in Vision and in
Imaging

Fenómenos Asociados a la Difusión de la Luz
en Visión e Imágenes de la Retina

D. Dimitrios Christaras
2016

UNIVERSIDAD DE
MURCIA



Universidad de Murcia
Departamento de Física
Laboratorio de Óptica

**LIGHT SCATTERING
PHENOMENA IN VISION AND IN
IMAGING**

**FENOMENOS ASOCIADOS A LA
DIFUSION DE LA LUZ EN VISION
E IMAGENES DE LA RETINA**

Thesis presented at the Faculty of Medicine
of the University of Murcia by:

Dimitrios Christaras

To attain the degree of PhD from the University of Murcia.

Laboratorio de Óptica. Departamento de Física. Universidad de Murcia.
June 2016

Contents

Resumen	1
Summary	5
1 Introduction	9
1.1 A brief historical note	9
1.2 Descriptors of an optical system	12
1.2.1 The Point Spread Function	12
1.2.2 The Modulation Transfer Function	13
1.2.3 Rotational symmetry in the PSF	14
1.3 Anatomy of the Eye	16
1.3.1 The Optics of the Eye	16
1.3.2 Anatomy of the fundus	18
1.4 Optical image quality	22
1.4.1 Diffraction	22
1.4.2 Aberrations	23
1.4.3 Ocular Straylight	25
1.4.4 The CIE glare function for the standard observer	29
1.5 Straylight in Vision and Imaging	31
1.6 Overview of experimental methods	33
1.6.1 The Double-pass Method	33
1.6.2 Heterochromatic Flicker Photometry	34
1.7 Motivation of the thesis	35
2 Light diffusion in the fundus	37
2.1 The Monte Carlo simulation	37
2.2 A model of fundus reflectance	38
2.3 Photon packet propagation considerations	39

2.4	Fundus diffusion and wavelength	44
2.5	The effect of choroidal melanin	46
2.6	Scattering and fundus diffusion	48
3	Fundus Diffusion and Vision	53
3.1	Subject classification	53
3.2	Optical test	54
3.3	The effect of fundus diffusion in vision	59
3.4	Diffuse light and sensitivity	62
4	Scattering in Vision and Imaging	67
4.1	PSF approximation	67
4.1.1	The method of Optical Integration	67
4.1.2	PSF reconstruction strategies	69
4.1.3	Two-dimensional PSF reconstruction	75
4.1.4	Image Enhancement	76
4.2	A single-pass test	78
4.2.1	Experimental Setup	79
4.2.2	PSF of the scatter filter	81
4.2.3	Image enhancement	82
4.3	Double-pass	85
4.3.1	Experimental setup and procedure	85
4.3.2	Image registration	91
4.3.3	Subjects	93
4.3.4	PSF reconstruction	93
4.3.5	Scattering compensation	99
5	Scattering in MPOD	105
5.1	MPOD from reflectometry	105
5.2	MPOD with HFP	114
5.2.1	Experimental Setup	117
5.3	RE and HFP comparison	120
6	Conclusions	123
	Bibliography	125
A	Monte Carlo simulation	143
B	Camera calibration	145

C Scripts	149
C.1 Point Spread Function CIE simulation	149
C.2 Diffraction-limited MTF	150
C.3 Centroid	151
C.4 MPOD with HFP	151
D Pulse Width Modulation	155
Acknowledgments	157

List of Figures

1.1	Polar coordinates for the spatial (left) and frequency (right) domains	14
1.2	Cross-section of the human eye. Image taken from Encyclopaedia Britannica.	16
1.3	Transverse section of the cornea. Image taken from Bron et al..	17
1.4	Lens cross-section.	18
1.5	Photoreceptor mosaic at the fovea (a) and at the periphery (b). The bigger dots are peripheral cones and the smaller ones rods. Image by Dubra et al..	19
1.6	Cross-section of the Retina. Image by Kolb.	19
1.7	Section of the fovea of a rhesus monkey viewed at white (top), blue (middle), and green (bottom) light. The macular pigment appears dark in the middle image because of its high absorption at blue. Image by Snodderly.	20
1.8	Diffraction patterns for circular aperture (a) and rectangular aperture (b).	22
1.9	Radiance profile for diffraction from circular aperture (a) and rectangular aperture (b). In (b) the different colors represent the different dimensions of the rectangle.	23
1.10	(a) LCA and TCA in the human eye. Image taken from Bradley and Thibos. (b) Effect of LCA in diopters with respect wavelength.	24
1.11	Example PSFs showing the dependence of aberrations on pupil size. Image by Roorda.	25
1.12	Normalized absorption with respect to wavelength for the different ocular absorbers. Replotted from Berendschot et al. (2003) and based on data by van Kampen and Zijstra (1983), Snodderly et al. (1984b) and Gabel et al. (1978).	29

1.13	Scatter parameter for the CIE glare function given by eq. (1.22) with respect to age at $\theta = 3^\circ$	31
1.14	The effect of scattering in an image with high dynamic range, for no scattering (a), medium scattering (b) and high scattering (c).	32
1.15	The effect of scattering in an image with medium dynamic range, for no scattering (a), medium scattering (b) and high scattering (c).	32
1.16	One of the first double-pass systems, built in 1966. Light from slit S_1 is projected and the retina and its image is recorded through slit S_2 by the photomultiplier T.	33
2.1	Simple 4-layer model of the fundus used for the Monte Carlo simulation. The layers from top to bottom are: Photoreceptor Layer, RPE, Choroid and Sclera.	39
2.2	Flow chart of the Monte Carlo simulation describing photon packet propagation in the fundus.	42
2.3	The effect of photon packet number in the Monte Carlo simulation.	43
2.4	Photon fluence in the fundus at 550nm (left) and 650nm (right).	44
2.5	Simulated PSF for fundus diffusion at 550nm (green) and 650nm (red).	45
2.6	Simulated disk of 14 degrees diameters after being diffused in the fundus at 550nm (a) and 650nm (b).	46
2.7	Simulated intensities at the center with respect to disk radius at 550nm (a) and 650nm (b) for two different melanin values. The different colors represent different choroidal melanin values.	47
2.8	Simulated intensities at the center with respect to disk radius at 550nm and 650nm for two different melanin values. In red and black the low melanin value and the high melanin value at 650nm respectively. At 550nm the respective curves, in green and blue respectively, are practically indistinguishable.	47
2.9	Ratio of the PSF at red wavelengths to the PSF at green wavelengths. Gray area corresponds to 2 standard deviations. Plot retrieved from Ginis et al. (2013).	48
2.10	Simulated PSFs for fundus diffusion at 560nm (green) and at 650nm (red), and the CIE glare function (black).	49
2.11	Intensity at the center of the disk with respect to disk radius with fundus diffusion only (blue) and with fundus diffusion and lens scattering (red) at 560nm.	50

2.12	Intensity at the center of the disk with respect to disk radius with fundus diffusion only (blue) and with fundus diffusion and lens scattering (red) at 650nm.	50
3.1	Schematic of the optical setup used for the measurement of the fundus reflectance.	55
3.2	Aperture configuration at the pupil plane. The light enters through the top and is captured through the bottom.	56
3.3	Fundus reflection at the center of the projected disk for the two different groups at 560nm (a) and at 650nm (b).	58
3.4	Fundus reflection for two different wavelengths and for two different subject groups with respect to field size. At 560nm (circles) the two groups are indistinguishable, whereas at 650nm (triangles) the light colored iris group exhibits a much higher relative reflection.	59
3.5	Schematic of the psychophysical setup used to measure relative color sensitivity.	60
3.6	Schematic of the test field used in the psychophysical experiment.	60
3.7	Relative green to red sensitivity without the annulus vs. relative green to red sensitivity with the annulus for all subjects. Subjects with dark iris are depicted with brown triangles and subjects with light iris with blue squares.	62
3.8	Relative green to red sensitivity for the two groups for the test field without the annulus (triangles) and with the annulus (circles).	62
4.1	Single-pass (a) and double-pass configuration (b) for the projection of the uniform disks.	68
4.2	Example of a noisy PSF reconstruction (left) using the method of finite differences (blue line), where the real PSF is depicted in black and the normalized intensities used for the reconstruction (right).	70
4.3	Dependence of the Intensity curve and the PSF by the parameters of the model, n (top) and θ_0 (bottom).	71
4.4	(a) Single-pass (red) and double-pass (blue) glare function for a set of ages for fixed pigmentation. (b). Double-pass normalized intensities with the corresponding single-pass scatter parameter for fixed pigmentation.	73
4.5	An example of a fit using the glare function.	74
4.6	PSF (a) and MTF (b) reconstruction for 1023 (blue) and 1024 (red) points.	76

4.7	MTF reconstruction for odd (blue) and even (red) points, for high density sampling.	76
4.8	Ringling in picture after performing a deconvolution.	77
4.9	Diffraction limited MTF for a square aperture (red) and scattering MTF (green).	78
4.10	Experimental setup for the single-pass reconstruction of the PSF. L1, L2, L3 and L4 lenses, D1 aperture, M half mirror and PM (Pro Mist) a scattering media, simulating scattering in the eye.	79
4.11	Graphical User Interface (GUI) developed in MATLAB for the control of the setup.	80
4.12	An schematic explaining the acquisition parameters of the camera. The orizontal axis represents time.	81
4.13	Intensities at the center for different disk radii (left) and PSF profile (right) of Pro Mist 1, reconstructed with the method of optical integration.	82
4.14	Reconstructed 2d PSF for filter Pro Mist 1.	82
4.15	(a),(d),(g) Original images. (b),(e),(h) Captured images through Pro Mist 1. (c),(f),(i) Reconstructed images	83
4.16	Profile of the original (blue), reconstructed (black) and “scattered” (green) image of the cathedral from fig. 4.15.	84
4.17	Profile of the original (blue), reconstructed (black) and “scattered” (green) image, for letter E, black on white background (a) and white on black background (b) from fig. 4.15.	84
4.18	Experimental setup for the double-pass measurements. S, xenon lamp, F, wavelength filter, I, motorized iris with diffruser, D1 and D2 rectangular diaphragms conjugate to the pupil, Sh, mechanical shutter, HM, half mirror and BS, beam splitter. In light gray, the fixation subsystem with LC the LCoS and P, P’ linear polarizers.	86
4.19	A photo of the system. The subject’s position is at the top left.	87
4.20	Aperture configuration at the pupil plane. The light enters from the top and is captured through the bottom.	87
4.21	Photo of the fixation subsystem, where the led source, the two polarizers, a lens and the LC2000 can be seen (a) and photo of the 2-camera stereoscopic subsystem for high precision pupil alignment (b)	88
4.22	Pupil alignment using 2-camera the stereoscopic subsystem.	89
4.23	Calibration process for the 2-camera stereoscopic system, where the Region of Interest (ROI) is selected for each camera.	90

4.24	Graphical User Interface (GUI) developed in Matlab for the control of the setup.	91
4.25	Two misaligned images of the fovea at 450nm due to fixational eye movements(a),(b), the superimposed image of the two original images (c) , and the superimposed image of the two images after image registration (d). In blue and green the relative image displacement.	93
4.26	Four images taken during the search for the proper conditions: An acceptable image (a), an image with its center very close to a vein (b), a partially saturated image (c) and a blurred image (d).	95
4.27	A sequence of 9 disks projected on the retina. The central patch used for the reconstruction of the PSF is depicted in red.	95
4.28	Normalized intensity at the center of the projected disc with respect to disk radius in degrees at 450nm (a), 550nm (b), 632nm (c) and 800nm (d).	97
4.29	Reconstructed PSFs for subject D.C. at 450nm (blue), 550nm (green), 632nm (red) and 800nm (black).	98
4.30	Normalized intensities at the center of the projected disk with respect to disk radius at 550nm(green) and 450nm(blue) for subject J.M. (a) and L.H. (b). The squares represent actual experimental data and the lines the fitted intensity curves using the glare function.	98
4.31	Reconstructed PSFs at 550nm (green) and 450nm(blue) for subject J.M. (a) and L.H. (b).	99
4.32	Partial images (a),(b) and final image (c) after registration and summation of the partial images.	100
4.33	Scattering (blue) and diffraction limited MTF (red) of the system for subject D.C. at 450 nm (a) and the filter function in the frequency domain (b).	101
4.34	MTFs showing the effect of diffracton, high and low order aberrations and scattering.	101
4.35	A 6 degrees radius foveal image before (left) and after (right) scattering compensation at 450nm.	102
4.36	A 6 degrees radius image at about 8 degrees nasally before (left) and after (right) scattering compensation at 632nm.	102
5.1	Macular pigment absorption spectrum normalized at 455nm by Brown and Wald (1963).	106

5.2	Simplified fundus model used for the calculation of MPOD. The layers from top to bottom: Inner Limiting Membrane (ILM), Macular Pigment (MP), Photoreceptor Layer (Ph), Retinal Pigment Epithelium (RPE), Bruch's Membrane (BM) and Chorioid (Ch).	106
5.3	Transmission spectrum of bandpass filters peaking at 450nm (blue) and at 550nm (green) used for the measurement of the MPOD.	109
5.4	Low pass filter function in the Fourier domain for the elimination of higher frequencies.	109
5.5	Example of a fundus image before (a) and after (b) applying the filter function of fig. 5.4.	110
5.6	MPOD spatial distributions after scattering compensation for 4 subjects.	111
5.7	MPOD profile before (blue) and after (red) scattering compensation for the seven subjects.	112
5.8	OCT scan of the fovea. The foveal pit can be seen at the very center of the foveola.	113
5.9	Schematic of the experimental setup for the psychophysical calculation of MPOD.	117
5.10	A photo of the psychophysical setup where (4) is the main component - the screen with the test field and the background and (2) an aperture conjugate to the pupil controlling retinal illumination.	118
5.11	Graphical User Interface for the control of the HFP system.	118
5.12	Schematic of the circuit used to drive the high power LEDs.	119
5.13	Comparison of the MPOD using the Reflectance method after scattering compensation and the HFP method.	122
5.14	Comparison of the MPOD using the Reflectance method before scattering compensation and the HFP method.	122
B.1	Quantum Efficiency (QE) for LUCA R with respect to wavelength.	146
B.2	Monitor luminance measured at a site against gray levels.	146
B.3	Interpolation fits for 5 different exposure times.	147
D.1	Pulse Width Modulation example: Simulation of 3 different voltage values using different duty cycles.	156

List of Tables

3.1	Optical and physical parameters of the eye used for the Zemax simulation.	56
3.2	Mean green to red sensitivity and deviation for the two experimental conditions for all six subjects	61
3.3	Relative increase in the green to red sensitivity with and without the annulus (first column) and relative increase on the available light at the photoreceptors with field size for the two groups.	63
4.1	Optical characteristics of the bandpass filters.	94
4.2	Logarithm of the scatter parameter S at 3 degree for 7 subjects for the available wavelengths	99
5.1	MPOD values before and after scattering compensation as well as the relative change between the two measurements for seven subjects.	114
5.2	MPOD values for six subject using the HFP method.	120

List of Abbreviations

PSF	Point Spread Function
MTF	Modulation Transfer Function
OTF	Optical Transfer Function
PTF	Phase Transfer Function
LSF	Line Spread Function
MP	Macular Pigment
MPOD	Macular Pigment Optical Density
HFP	Heterochromatic Flicker Photometry
MC	Monte Carlo
SC	Stiles - Crawford
OCT	Optical Coherence Tomography
GUI	Graphical User Interface
RPE	Retinal Pigment Epithelium
ILM	Inner Limiting Membrane
PWM	Pulse Width Modulation

Resumen

Cuando la luz viaja a través del ojo para formar la imagen retiniana se ve afectada por los medios ópticos de forma que el objeto y la imagen nunca pueden ser idénticos. La luz se dispersa según una función, característica de cada sistema óptico, la función de dispersión de punto (PSF) que depende básicamente de tres fenómenos: la difracción, las aberraciones y el scattering, cada uno afectando la PSF de un modo distinto. La difracción, aunque en realidad es un fenómeno general que describe el cambio de dirección de la luz cuando encuentra un obstáculo físico, en la óptica fisiológica se refiere a la difracción de la luz en la pupila. Las aberraciones, por otro lado, describen cualquier desviación del sistema óptico perfecto, o cualquier desviación de la aproximación paraxial. En las últimas dos décadas, las aberraciones oculares de bajo y alto orden se han medido de manera efectiva y se han corregido con éxito utilizando la óptica adaptativa. Tanto la difracción como las aberraciones, afectan principalmente a la parte central de la PSF, que está relacionada con las características de alta frecuencia, o los detalles de la imagen. La difracción y las aberraciones degradan la imagen de la retina que afecta la agudeza visual y la sensibilidad al contraste.

El *scattering* se refiere a la dispersión de la luz debido a las estructuras de aproximadamente 10 micrómetros o menos, y afecta no solo a la zona central pero a la zona periférica de la PSF también. Por lo tanto, contrariamente a la difracción y las aberraciones, los efectos de la dispersión en la imagen afectan igual a las frecuencias más bajas, y se percibe como una pérdida de contraste que depende en gran medida del rango dinámico de la imagen, o de la presencia de fuentes de resplandor ("glare sources"). El scattering aumenta con la edad y especialmente en los pacientes con cataratas y puede conducir a una pérdida severa de contraste. La PSF afecta de la misma manera a la visión y a la formación de imágenes del fondo del ojo, a pesar de que la retina y los procesos que tienen lugar en nivel neural puedan compensar

parcialmente los errores de la visión.

El objetivo de esta tesis es estudiar el efecto del scattering en la visión y en la obtención de imágenes de la retina. El primer paso fue construir un modelo teórico del fondo de ojo y simular, usando técnicas Monte Carlo, la difusión de la luz en el fondo del ojo con diferentes longitudes de onda, y su dependencia con la pigmentación. Se demostró que existe una fuerte dependencia de la difusión en el fondo del ojo con la longitud de onda, con una reflectancia aproximadamente 10 veces más alta en longitudes de onda más largas. Además, se observó una dependencia de la difusión del fondo de ojo en los cambios con la pigmentación, únicamente para las longitudes de onda más largas, mientras que las longitudes de onda medianas no se vieron afectados. Además, la difusión en el fondo se comparó con el scattering producido en la óptica del ojo y el rango espacial de cada fenómeno. El estudio mostró que para longitudes de onda intermedias la difusión es dominante hasta aproximadamente 2 grados de ángulo visual, mientras que para las longitudes de onda más largas pueden dominar hasta los 4 grados. Se investigó el efecto de la difusión del fondo de ojo en la visión. En primer lugar, usando una técnica óptica, se cuantificó la luz difundida en el fondo del ojo para diferentes condiciones espaciales en verde (550 nm) y rojo (650 nm) midiendo la reflectancia del fondo de ojo para 6 sujetos agrupados según su pigmentación. Se encontró un aumento significativo en la reflectancia en los sujetos con más pigmentación para las longitudes de onda más largas, en línea con las simulaciones y estudios anteriores. En segundo lugar, se construyó un sistema psicofísico, basado en el método de Heterochromatic Flicker Photometry (HFP), para medir la sensibilidad en verde y rojo para dos condiciones espaciales distintas. Las medidas ópticas se compararon con las medidas psicofísicas donde se observó un aumento de la sensibilidad con la reflectancia del fondo de ojo, consistentes en todos los sujetos. Dado que la reflectancia del fondo de ojo depende de la pigmentación, los individuos de pigmentación baja muestran una sensibilidad al color rojo mayor.

En la otra parte de la tesis, se estudió el scattering en los medios oculares, centrandose en el efecto de la dispersión en la imagen del fondo. Para este propósito, un sistema óptico se construyó, basado en el principio de doble paso, capaz de adquirir imágenes del fondo ocular a diferentes longitudes de onda y tamaños de campo. El método completo se probó y validó primero en una configuración en paso simple, donde el scattering se introdujo por medio de filtros. La reconstrucción de la PSF completa se realizó en 7 sujetos utilizando el método de integración óptica suponiendo una PSF basada en la *CIE glare function*. Se registraron imágenes del fondo a diferentes longitudes de onda y la imagen original se reconstruyó aplicando un custom método de "enhancing" de contraste usando con la PSF reconstruida. Se demostró que

la compensación de scattering puede mejorar significativamente el contraste de la imagen. El nivel de mejora depende no sólo de la cantidad de scattering para la longitud de onda específica, sino también del rango dinámico de la imagen del fondo. Se encontró una mejora de alrededor del 10 % para la configuración específica.

El método de compensación de scattering se aplicó en el caso de la medida de la densidad óptica del pigmento macular (MPOD) usando imágenes retinianas. Según este método se tomaron dos imágenes de fondo de ojo, una a la longitud de onda donde el pigmento macular no absorbe y otra a una longitud de onda en el que muestra su pico de absorción y se extrajo la MPOD usando una fórmula matemática. El cálculo se hizo antes y después de aplicar el algoritmo de compensación de scattering para 6 sujetos y se midió una subestimación media de la MPOD de aproximadamente un 10 %.

Por último, para probar los resultados con un método ya conocido de MPOD se construyó un sistema adicional psicofísico, basado en el método de HFP, que está afectado únicamente a un pequeño grado de scattering. Se observó una buena correlación entre los dos métodos que aumenta cuando el scattering se compensa.

Summary

When light travels through the eye to form the retinal image, it is affected by the optical media in a number of ways, such that the object and image space can never be identical. The light is spread according to a function, characteristic of the system, called the Point Spread Function (PSF) and it depends on three main phenomena: diffraction, aberrations and scattering, each one of them with different effects. Diffraction, although in reality a very general effect describing essentially the redirection of the light when meeting an obstacle, in physiological optics usually refers to diffraction at the pupil. Aberrations, on the other hand, is a more general term describing any deviation from the perfect model, or any deviation from the paraxial approximation. In the last two decades, low and high order ocular aberrations have been successfully measured and corrected using adaptive optics. Both diffraction and aberrations affect mainly the central part of the PSF, that is related to the high frequency features, or the details of the image. Diffraction and aberrations degrade the retinal image affecting visual acuity and contrast sensitivity.

Scattering refers to the spreading of the light due to structures of about 10 microns or less, and it is not restricted to the central part of the PSF but affects its wide-angle parts as well. Therefore, contrary to diffraction and aberrations, scattering also affects low frequencies and it is perceived as a loss of contrast which depends heavily on the dynamic range of the image, or the presence of glare sources. Scattering increases with age and especially in cataract patients and can lead to a severe contrast loss. The PSF affects in exactly the same way, both vision and fundus imaging, although the retina and the processes taking place at a neural level can partially compensate the errors for vision.

The purpose of this thesis is to study the effect of scattering in vision and in fundus imaging. The first step was to build a theoretical fundus model

and quantify light diffusion in the fundus at different wavelengths and its dependence on the melanin pigmentation, simulating realistic pigmentation values found in a normal population. It was shown that there is a strong dependence of fundus diffusion on wavelength, with even 10 times higher reflectance or more at longer wavelengths. Moreover, a dependence of fundus diffusion was observed on changes in melanin pigmentation but only for longer wavelengths, whereas medium wavelengths were unaffected. Additionally, fundus diffusion was compared to scattering in the optical media and the spatial dominance of each phenomenon was studied. The study showed that for medium wavelengths diffusion is dominant to up to about 2 degrees of visual angle, whereas for longer wavelengths the domain of dominance increases to 4 degrees.

The effect of fundus diffusion in vision was investigated. Firstly, using an optical technique, diffused light in the fundus was quantified for different spatial conditions at green (550nm) and red (650nm) through the measurement of fundus reflectance for 6 subjects grouped according to their melanin pigmentation. There was a significant increase in reflectance at light pigmentation subjects for longer wavelengths, which was in line with previous simulations and studies. Secondly, a psychophysical setup based on the Heterochromatic Flicker Photometry (HFP) method was built and the green to red color sensitivity for two different spatial conditions was measured. The measurements of the optical system were then compared to the psychophysical ones where an increase in sensitivity with fundus reflectance was observed, consistent in all subjects. Consequently, since fundus reflectance depended on pigmentation, light pigmentation individuals have an increased red to green color sensitivity.

In the other part of the thesis, the focus was shifted towards the study of scattering in the ocular media, with the center of attention being the effect of scattering in fundus imaging. For this purpose, an optical setup was built based on the double-pass principle, capable of acquiring fundus images at various wavelengths and field sizes. The complete method was first tested and validated in a single-pass setup where scattering was introduced by a scatter filter. The reconstruction of the wide angle PSF was done for 7 subjects using the method of optical integration assuming a PSF based on the CIE glare function. Fundus images at different wavelengths were acquired for the subjects and the original intensity map of the image was reconstructed by applying a custom contrast enhancement method using the reconstructed PSF. It was shown that this scattering compensation technique can significantly improve the contrast of the image. The improvement depended not only on the amount of scatter for the specific wavelength but also on the dynamic range of the fundus. An improvement of about 10% was found for

the specific setup.

The scattering compensation method was applied in the case of the Macular Pigment Optical Density (MPOD) measurement using reflectometry. In this method two fundus images were taken, one at wavelength where macular pigment does not absorb and another at a wavelength where it shows its peak absorption and the MPOD was extracted using the pixel intensities of the two images. The calculation was done both before and after applying the scattering compensation algorithm for 6 subjects and an average MPOD underestimation of about 10% was observed.

Finally, in order to test the results against a proven MPOD measurement, a psychophysical setup was built, based on the HFP method, which is affected only to a small degree by scattering. A very good correlation between the two methods was observed and the agreement increased when scattering was compensated.

Chapter 1

Introduction

In this first chapter the most important physical quantities of an optical system will be discussed. Additionally, a general overview of the function of the eye will be presented and key quantities of the theory will be described.

The chapter starts by briefly explaining the Point Spread Function (PSF) and the Modulation Transfer Function (MTF) and their importance in an optical system. The chapter continues with a short presentation of the various structures that comprise the eye and it continues with the description of the various optical phenomena that take place in the eye. Intraocular scattering is more extensively discussed, since it is the main focus of this work.

1.1 A brief historical note

The eye and the human visual system have always been a subject of research for the natural scientist and have attracted the attention of many great scientists, and not without a good reason; about 80% of the information our brain receives passes through our eyes. Nevertheless, it took centuries for science to explain vision, and even today, it is not fully understood.

The Hellenistic approach to vision assumed that the vision involved an active interaction with the object, in the same way that the sense of touch functions. The strong background of the Greeks in geometry lead to some geometrically consistent theories of vision, most famous being that of Euclid as described in *Optika*, the first rigorous, mathematical theory of vision. Euclid's theory, however, was based in *extramission*, or the eye's emission of light¹ to the object. The first complete *intramission* attempt to describe

¹Euclid, Plato, and later Ptolemy, they all believed that there is a fire burning deep into the eye, emitting light to the objects . Similar views for the "power" of the eye still

vision, where the eye had solely the role of the detector, was elaborated by Aristotle in which he dismissed the contact nature of vision and hypothesized that there is a medium between the object and the eye which is moved by the object's color and consequently reaches the eye and is sensed².

Nevertheless, and despite its failure to correctly explain the visual phenomena, the Hellenistic tactile approach to vision remained the dominant theory for almost 2000 years. It wasn't until about 1000 A.D. when an Arab scientist, Alhazen, combining the rigorous geometrical approach from Euclid and Ptolemy with Aristotle's intromission theory, came up with a realistic description of the visual function. Alhazen's approach along with Kepler's theory of retinal image paved the way for modern physiological optics and visual science³.

But even centuries later, when the function of the eye was better understood and there was by then a more compact theory explaining the basics of vision, the eye never ceased to amaze the natural scientist. In one of the most influential scientific books of all times, *On the Origin of Species*, Charles Darwin describes the eye as an *organ of extreme perfection and complication* that at a first glimpse makes natural selection seem absurd (Darwin, 1859). I quote from the source:

Can we believe that natural selection could produce, on the one hand, organs of trifling importance, such as the tail of a giraffe, which serves as a fly-flapper, and, on the other hand, organs of such wonderful structure, as the eye, of which we hardly as yet fully understand the inimitable perfection?[...] To suppose that the eye, with all its inimitable contrivances for adjusting the focus to different distances, for admitting different amounts of light, and for the correction of spherical and chromatic aberration, could have been formed by natural selection, seems, I freely confess, absurd in the highest possible degree. Yet reason tells me, that if numerous gradations from a perfect and complex eye to one very imperfect and simple, each grade being useful to its possessor, can be shown to exist; if further, the eye does vary ever so slightly, and the variations be inherited, which is certainly the case; and if any variation or modification in the organ be ever useful to an animal under changing conditions of life, then the difficulty of believing that a perfect and complex eye could be

exist in some religions.

²The famous Democritus and Epicurus believed in intromission too, amongst others.

³Surprisingly, Kepler understood right the image formation from the cornea and lens but him too, erroneously believed in extramission.

formed by natural selection, though insuperable by our imagination, can hardly be considered real.

The eye for Darwin, was both the weakest and the strongest point of his brilliant theory of evolution. On the one hand its carefully-designed structure and its highly sophisticated function made it unbelievable to be the result of something as "naive" as evolution, and not the result of a precise and intelligent design⁴. On the other hand, by simply observing the great variety of visual systems in nature, from the very complex one to a simple binary photo-detector, and how conveniently each system serves the particular organism, evolution became the most fit candidate.

To prove his point, Darwin presented a scenario of a very simplistic first "eye", consisting of solely two cells: a photoreceptor cell and a pigment cell. The photoreceptor cell would absorb the incident light and the pigment cell would absorb the light from one side making the eye capable of detecting orientation. In Darwin's theory, this scenario was the result of a purely stochastic event due to random gene variations - what we now know as mutations, and through the process of natural selection could eventually lead to more advanced visual systems. The case of the human eye was of such complexity that it took scientists more than a century to elaborate a more complete theory for the evolution of the eye, based on hard scientific evidence.

Indeed, the eye is incomparable to any other organ; robust optical design, a mechanism to control the amount of light entering, the ability to rotate and to focus on demand, and a complicated retina, capable of detecting a wide spectrum of light and turning it into electrical signals. These electrical signals are then channeled to the brain to be processed. The size and arrangement of the photoreceptors is nicely tuned with the optics, providing both protection from aliasing and good spatial resolution down to an impressive 30 cycles per degree at the fovea (Smith and Atchison, 1997). Three different photoreceptor classes called cones can give a color depth of about 10 million colors and along with a fourth class, the rods, achieve an impressive dynamic range of almost 11 log units (Stockman and Sharpe, 2006), more than what most modern cameras can achieve. Our highest resolution region, the fovea, is cleverly protected from the high energy blue light by a carefully placed pigment, called macular pigment, which rapidly vanishes in the periphery (Snodderly et al., 1984b).

Despite its impressive capabilities, the eye is far from being perfect; it has a number of functional problems, the most common of them being myopia

⁴Darwin's skeptics and creationists quote this very specific phrase to attack the evolution theory.

or hyperopia, with more than one third of the population suffering from either illness. And it is caused neither by injury nor by disease; it is simply caused by the fact that the eye does not have the correct axial length. On top of that, our eyes age prematurely; by the age of 40 we start losing the functionality of our crystalline lens and focusing on closer objects becomes difficult Koretz et al. (1989), and by the age of 50 the eye is no longer capable of accommodating (Atchison, 1995; Charman, 2008).

In addition to normal aging, there are thousands of diseases affecting all parts of the eye, like cataract, glaucoma, age-related macular degeneration, retinal detachment, diabetic retinopathy and hypertension retinopathy just to name a few. Hence, the study of the eye goes beyond our urge to understand the physics of this complex organ or the evolution; there is a far more urgent need for effective diagnosis and treatment for the numerous diseases of the eye. There is a strong need for medical apparatuses for an objective and efficient characterization of the optical quality of the eye, but also for the early and precise diagnosis of ocular diseases. The fundus camera, the Photorefractor, the Scanning Laser Ophthalmoscope, the Macular Densitometer, the Optical Coherence Tomography scanner, are only a few of the devices used in Ophthalmology, and there is a constant demand for new and more precise techniques. Technology has been translated from different fields of science and applied for the better imaging of the fundus, with the best example being that of the Adaptive Optics technique, which was first used in astronomy and later became a powerful ophthalmological tool.

Yet, there is another reason that makes the study of the eye, and especially its fundus of absolute importance: a number of systemic diseases, such as hypertension, diabetes and arteriosclerosis, can be manifested at the ocular fundus, and many of them can be diagnosed long before their symptoms appear to the rest of the system. But there is more to it. The formation of the image onto the retina and the consequent detection of light is only the very first step of the complicated process of vision. The spatial and temporal characteristics of vision and color detection and in general the perceptual and cognitive study of vision is truly important for a better understanding of, not only vision, but also the human brain and human nature in general.

1.2 Descriptors of an optical system

1.2.1 The Point Spread Function

Every optical system is characterized from its Point Spread Function (PSF): the light distribution of a point source in the object space after going through

the optics of the system. As the name suggests, this measures the "spread" of this point in the image space. The amount, but also the type of spreading is used to measure the quality and the performance of an optical system.

Assuming an infinitesimal two-dimensional point source $s(x, y) = \delta(x, y)$ and by defining the effect caused by the system \mathbf{T} , the PSF will be

$$PSF(x, y) = \mathbf{T}(\delta(x, y)) \quad (1.1)$$

Now, let $f(x, y)$ describing an intensity distribution of an object. In the image space its distribution $g(x, y)$ will be given by the convolution of the object space intensity distribution with the system's PSF

$$g(x, y) = PSF(x, y) \otimes f(x, y) \quad (1.2)$$

Image formation can then be mathematically described through a convolution process. Consequently, an ideal system would have a $PSF(x, y) = \delta(x, y)$, and the intensity distribution in the image space and in the object space would be identical.

The PSF integrates to unity, so that it expresses the *normalized* intensity distribution

$$\int_0^{2\pi} \int_0^{\infty} PSF(r, \theta) r dr d\theta = 1 \quad (1.3)$$

There are 3 physical phenomena, macroscopic and microscopic, that dictate the shape of the PSF: Diffraction, Aberrations and Scattering. These phenomena will be explained in more details later in the chapter.

1.2.2 The Modulation Transfer Function

Let u and v be the frequency variables conjugate to the spatial variables x and y respectively. The Optical Transfer Function (OTF) can be defined as the Fourier transfer of the PSF

$$OTF(u, v) \equiv \mathcal{F}\{PSF(x, y)\} \quad (1.4)$$

The OTF is generally a complex function, with both a magnitude and phase component

$$OTF(u, v) \equiv H(u, v) = |H(u, v)|e^{-i\theta(u, v)} \quad (1.5)$$

The magnitude of the OTF $|H(u, v)|$ is called Modulation Transfer Function (MTF) and its phase $\theta(u, v)$ Phase Transfer Function (PTF). The OTF describes the complete response of the system to harmonic functions, for example a sinusoidal pattern. The MTF can then be described as the amplitude response of the system to these harmonic functions and it is equivalent to the

ratio of the initial contrast with the final contrast. The importance of the MTF as an optical descriptor lies in the fact that that expresses both contrast (modulation) and resolution. In physiological optics the MTF is usually normalized to unity and the frequency is expressed in cycles per degree. The PTF, on the other hand, expresses the phase shift induced by the system in each harmonic function and, despite the fact that its effect is in some cases detrimental, it is less frequently used as an optical quality descriptor.

1.2.3 Rotational symmetry in the PSF

As will be seen in chapter 4 rotational symmetry of the PSF is assumed. Rotational symmetry can greatly simplify the PSF approximation and make mathematical manipulations possible.

Let $\mathcal{F}\{f(x, y)\}$ be the 2D Fourier Transform defined as

$$F(u, v) \equiv \mathcal{F}\{f(x, y)\} = \int_{-\infty}^{\infty} \int_{-\infty}^{\infty} f(x, y) e^{-i(ux+vy)} dx dy \quad (1.6)$$

where x, y and u, v are the Cartesian coordinates in the spatial and frequency domain respectively. Introducing polar coordinates in both the spatial and

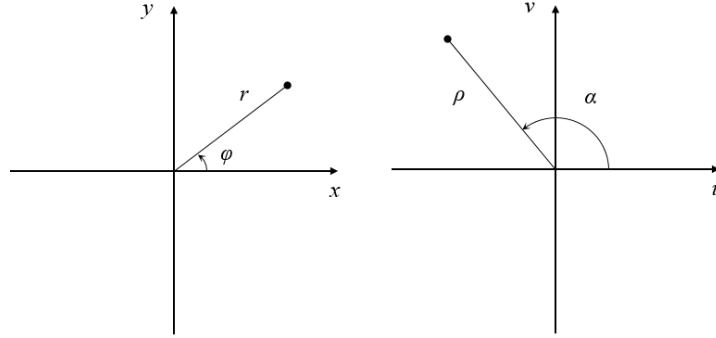


Figure 1.1: Polar coordinates for the spatial (left) and frequency (right) domains

the frequency domain (see fig. 1.1)

$$x = r \cos \phi \text{ and } y = r \sin \phi \quad (1.7)$$

$$u = \rho \cos \alpha \text{ and } v = \rho \sin \alpha \quad (1.8)$$

$$dx dy = r dr d\phi \quad (1.9)$$

where the r in eq. (1.9) is simply the determinant of the Jacobian for the transformation from Cartesian to polar coordinates. The quantity $ux + vy$ in

the exponential now becomes

$$\begin{aligned} ux + vy &= r\rho(\cos\phi\cos\alpha + \sin\phi\sin\alpha) \\ &= r\rho\cos(\phi - \alpha) \end{aligned} \quad (1.10)$$

Substituting eq. (1.10) in (1.6) one gets

$$F(\rho, \alpha) = \int_{-\pi}^{\pi} \int_0^{\infty} f(r, \phi) e^{-ir\rho\cos(\phi-\alpha)} r dr d\phi \quad (1.11)$$

By simply changing the order of integration eq. (1.11) becomes

$$F(\rho, \alpha) = \int_0^{\infty} f(r)r \int_{-\pi}^{\pi} e^{-ir\rho\cos(\phi-\alpha)} d\phi dr \quad (1.12)$$

where it was also assumed that $f(r, \phi) = f(r)$ since it is rotationally symmetric.

Without the loss of generality, one can pick a polar coordinate system (ρ, α) such that the ρ vector lies on the $\alpha = 0$ axis, and consequently $F(\rho, \alpha) = F(\rho)$. Setting $\alpha = 0$ and after some simple algebra the integral over ϕ in eq. (1.12) becomes

$$\int_{-\pi}^{\pi} e^{-ir\rho\cos(\theta)} d\theta = 2 \int_0^{\pi} \cos(r\rho\cos\theta) d\theta = 2\pi J_0(r\rho) \quad (1.13)$$

where $J_0(x)$ is the zeroth-order Bessel function and the fact the parity of the trigonometric functions was used. Plugging the last result into eq. (1.12) one gets

$$F(\rho) = 2\pi \int_0^{\infty} r f(r) J_0(r\rho) dr \quad (1.14)$$

Similarly one can show that

$$f(r) = \frac{1}{2\pi} \int_0^{\infty} \rho F(\rho) J_0(r\rho) d\rho \quad (1.15)$$

Relations eq. (1.14) and eq. (1.15) are called zeroth order Hankel transforms, and two very important results emerge from them:

- The Fourier transform of a rotationally symmetric function has no phase component and therefore is always real.
- The Fourier transform of a rotationally symmetric function is also rotationally symmetric.

Since OTF is defined as the Fourier transform of the PSF, for a rotationally symmetric PSF, the OTF is real and rotationally symmetric and identical to the MTF. This result is very important and it allows to perform certain manipulations of the PSF as it will be seen later in chapter 4.

1.3 Anatomy of the Eye

The adult eye is a spherical structure with a diameter of roughly 24mm, coupled with six muscles which allow to perform an almost perfect rotation. There are three elements with a key role in the eye's function: the cornea and the lens, mutually responsible for the image formation, and the retina, responsible for the image detection and transmission of the signal to the brain. A number of structures, such as the iris, the choroid, the vitreous and the sclera, have a supportive role in the eye function, for example providing nutrition and protecting the retina (Trier, 2006; Nickla and Wallman, 2010). A diagram with the main structures in the eye is shown in fig. 1.2

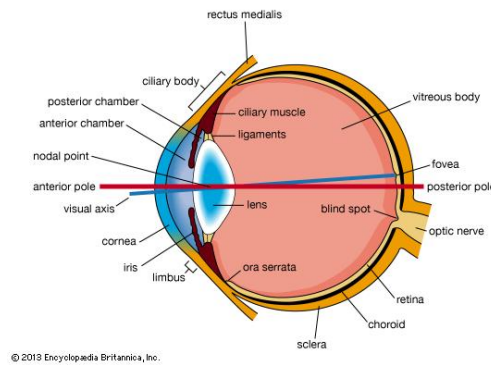


Figure 1.2: Cross-section of the human eye. Image taken from Encyclopaedia Britannica.

1.3.1 The Optics of the Eye

Compared to non-biological optical systems the eye from the optical point of view is far from being complex. The formation of the image of an object is done through two lens-like elements; the cornea and the crystalline lens. The iris has a supportive optical role, acting as a variable circular diaphragm. Due to a slight misalignment of the cornea and the lens the visual axis and the optical axis do not coincide and therefore the image of an object lying on the optical axis will be created at about 4 degrees off-axis, on a location on the retina called the fovea (Artal and Tabernero, 2008), as shown in fig. 1.2.

The cornea is a transparent, avascular meniscus shaped lens, with an outer surface curvature of about 8mm and an average of about 0.5mm central thickness, responsible for roughly one third of the refraction happening in the eye. It has a refractive power of about 48 diopters, when surrounded by air, and a refractive index of 1.376. Behind the posterior surface of the cornea the chamber formed by the posterior cornea and the anterior lens is filled

with aqueous humor, a water-like liquid, with a refractive index of 1.336, that reduces the effective refractive power of the cornea to about 42 diopters (Atchison and Smith, 2000; Asbell and Brocks, 2010). The cornea consists of five layers: The epithelium, the bowman's membrane, the stroma, Descemet's Membrane and the endothelium (Bron et al., 1998). The internal structure of the cornea is seen in fig. 1.3. The Stroma, which makes up for about 90% of the total volume of the cornea, has a very tightly organized structure, necessary for maintaining the cornea's transparency.

The cornea is covered by a water-like structure, called tear film. The tear film's function is to normalize any corneal irregularities thus playing an important role in the quality of the image, although its function is often underestimated.

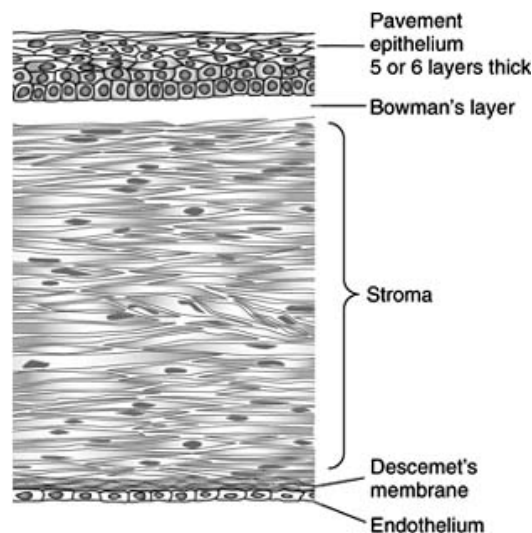


Figure 1.3: Transverse section of the cornea. Image taken from Bron et al..

The second refractive element of the eye, the lens, is a transparent avascular structure, positioned right behind the iris and is a mass of non-uniform cellular tissue lying within an elastic capsule. It is composed by onion-like layers of fiber cells, stretching from the anterior pole to the exterior pole, as seen in fig. 1.4. The fiber cells' density increases moving towards the nucleus, leading to a variable refractive index within the body of the lens which peaks at the center of the lens, and has an average of about 1.42 (Atchison and Smith, 2000).

The lens has the unique ability to rapidly change its shape with the help of the ciliary muscles, making it possible to focus from the infinity to an impressive distance of 10cm, which translates to a change in power of about 16 diopters, without any signs of fatigue. This extraordinary function of the

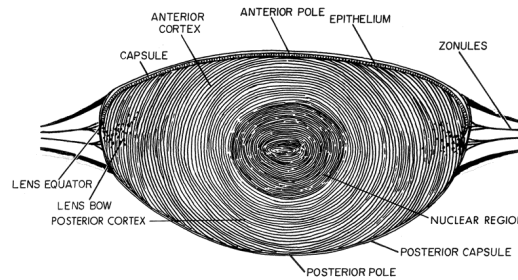


Figure 1.4: Lens cross-section.

optical system is not flawless however; accommodation is lost gradually with age leading to a significant loss of accommodation already at the age of 40 (Atchison, 1995).

Finally, posterior to the lens lies the vitreous body filled with the vitreous humor, a liquid optically identical to the aqueous humor.

1.3.2 Anatomy of the fundus

The ocular fundus, is a skin-like structure, consisting of a number of different layers. The different fundus layers can be classified in two main groups: the structure responsible for vision called the retina and the deeper fundus layers which have primarily a supportive role to the retina.

The Retina

The structures responsible for light detections are the photoreceptor cells, forming part of the retina. They contain a light-sensitive protein called opsin, the molecule that makes vision possible. The photoreceptors come in two types; the cones, found primarily at the central part of the retina, responsible for color vision, and the rods which increase at the periphery, responsible mainly for low light vision. Cones come in three classes; the Long (L), the Medium (M) and the Short (S), with peak sensitivities at long, medium and short wavelengths respectively, as their name suggests. The exact percentage of L,M and S cones varies greatly amongst individuals (Carroll et al., 2002; Stockman and Sharpe, 2000; Hofer et al., 2005). An example of a cone mosaic is shown in fig. 1.5.

The retina has an average thickness of about 0.5 millimeter with its inner structure shown in fig. 1.6. Surprisingly, photoreceptors do not come first in the light path in the retina, but rather last, with the light traveling the entire retina before being detected. This "inverted" structure has been the subject of many studies and has been considered a major imperfection of the

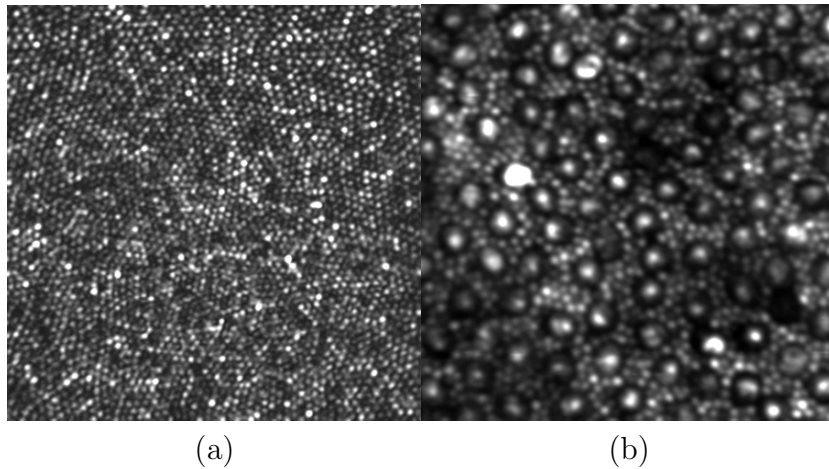


Figure 1.5: Photoreceptor mosaic at the fovea (a) and at the periphery (b). The bigger dots are peripheral cones and the smaller ones rods. Image by Dubra et al..

human eye. Recently, a study has shown, however, that Muller cells in the retina act as waveguides for the mid-long wavelengths and scatter the shorter wavelengths, improving this way vision (Labin et al., 2014).

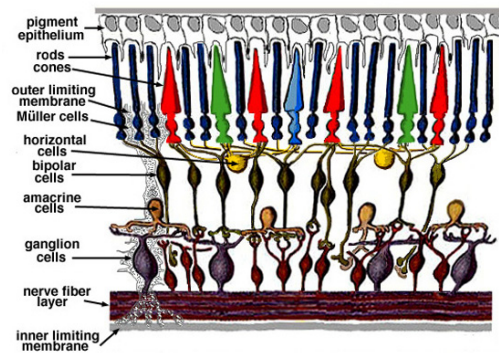


Figure 1.6: Cross-section of the Retina. Image by Kolb.

Though oversimplified, the retinal function can be described briefly in the following steps: detection at the photoreceptors, transmission to the bipolar cells, from there to the ganglion cells and finally transmission through the optic nerve.

The retina, apart from the elements related to light detection, is also comprised of layers that have a protective role, namely the Inner Limiting Membrane (ILM), Bruch's Membrane and the Retinal Pigment Epithelium (RPE).

The RPE is a melanin-containing mono-layer that lies between the photoreceptors and choroid and, though it doesn't participate directly in vision, has an essential role in the correct function of the retina. Firstly, due to its highly melanin content, it absorbs light exiting the photoreceptors, thus reducing scattering (Bok, 1993). Additionally, it controls the flow of fluid and nutrients from the blood to the retina and vice versa (Steinberg, 1985) and it participates in pigment regeneration.

The Macular Pigment

The Macular Pigment (MP) is a collective name for the substances lutein and zeaxanthine (Bone et al., 1985; Landrum and Bone, 2001; Bone et al., 1993), found exclusively at the fovea, at the axons of the cone photoreceptors (Snodderly et al., 1984a), and it acts as a highly blue absorbing filter, with a peak absorption at about 460nm (Brown and Wald, 1963). Zeaxanthine and lutein belong to the carotenoid family and they are not synthesized by our system but are rather supplied directly from our diet (Hammond et al., 1997b), found in foods like spinach, the orange pepper and maize. There are several studies showing a strong correlation between the intake of those specific carotenoids and the increase in the MP optical density (Aleman et al., 2001; Berendschot et al., 2000; Landrum et al., 1997; Hammond et al., 1997a). Due to its dietary dependence, it shows a great variation amongst individuals (Wooten and Hammond, 2002; Bone and Sparrock, 1971) and there doesn't seem to be a correlation with age (Delori et al., 2001; Berendschot and van Norren, 2005; Bone et al., 1988).

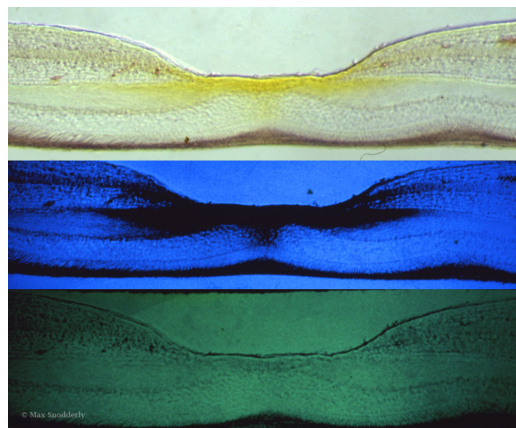


Figure 1.7: Section of the fovea of a rhesus monkey viewed at white (top), blue (middle), and green (bottom) light. The macular pigment appears dark in the middle image because of its high absorption at blue. Image by Snodderly.

Though its complete role is still under investigation, there is strong evidence of its role primarily in the protection of the retina and secondarily in the correct function of vision. There is growing evidence on the protective role of the MP against high energy - short wavelength light which can have photo-oxidative effects on the cell (Snodderly, 1995; Kirschfeld, 1982). It is clear that the MP also has a positive effect in vision, since it filters the blue light and reduces the effect of chromatic aberration in the fovea (Reading and Weale, 1974). Limited evidence also show some correlation between visual acuity and macular pigment, as well as contrast sensitivity and macular pigment, though as the authors of these particular studies point out, it needs further investigation (Wooten and Hammond, 2002; Loughman et al., 2010a). Additionally, recent studies have shown a correlation between macular pigment optical density and cognitive function in older people Feeney et al. (2013); Vishwanathan et al. (2014)

Finally, there has been a number of studies in the last two decades pointing to a direct correlation between the MPOD and the Age-related Macular Degeneration (AMD) (Snodderly, 1995; Beatty et al., 2001, 1999; Tan et al., 2008; Loane et al., 2008; Algvere et al., 2006), one of the leading causes of blindness in the western world (Klein et al., 1995, 1999; Klaver et al., 2001), suggesting that an increase in the intake of carotenoids has a positive effect on the prevention of AMD.

Deeper fundus layers

In the current work, deeper fundus layers are collectively called the choroid and the sclera, or else the fundus elements that are not part of the retina.

The choroid is one of the most highly vascularized tissues of the body and traditionally viewed as the structure responsible for providing nutrients and oxygen to the outer layers of the retina. Along with the ciliary body and the iris, they form the uvea. The choroid is comprised of blood vessels, melanocytes, fibroblasts, resident immunocompetent cells and supporting collagenous and elastic connective tissue. The melanin in the choroid, has an entirely different origin of the melanin in the the RPE and is related to skin and iris pigmentation. Choroidal melanin, similarly to skin melanin, has been found to be highly variable amongst individuals, whereas the RPE melanin is constant amongst the healthy population (Weiter et al., 1986), since the RPE is part of the neural retina.

The sclera, surprisingly, is made of the same building block as the cornea, the collagen fibrils. The lattice arrangement of the collagen is what makes the cornea transparent and the sclera opaque. Sclera's main function is to protect the eye, to hold the extraocular muscles, to maintain the eye's

spherical shape, and acts as a channel for the vessels and nerves.

1.4 Optical image quality

1.4.1 Diffraction

Diffraction describes the deviation of the from geometrical optics when light is obstructed by an obstacle or an opening, such as a slit or a sharp edge and it is caused by the wave nature of light. A very common example of diffraction is when observing the shadow cast by an object, where the edges are always smeared out. In physiological optics, the term diffraction is usually used to describe diffraction at the pupil, although in reality diffraction is the underline, physical cause for other optical phenomena as well.

In the case of diffraction from an aperture, the intensity pattern of the PSF depends on the size and the shape of the aperture, as seen in the examples in fig. 1.8, corresponding to a circular aperture of 5mm and a rectangular aperture of 5mm by 2.5mm for 500nm light.

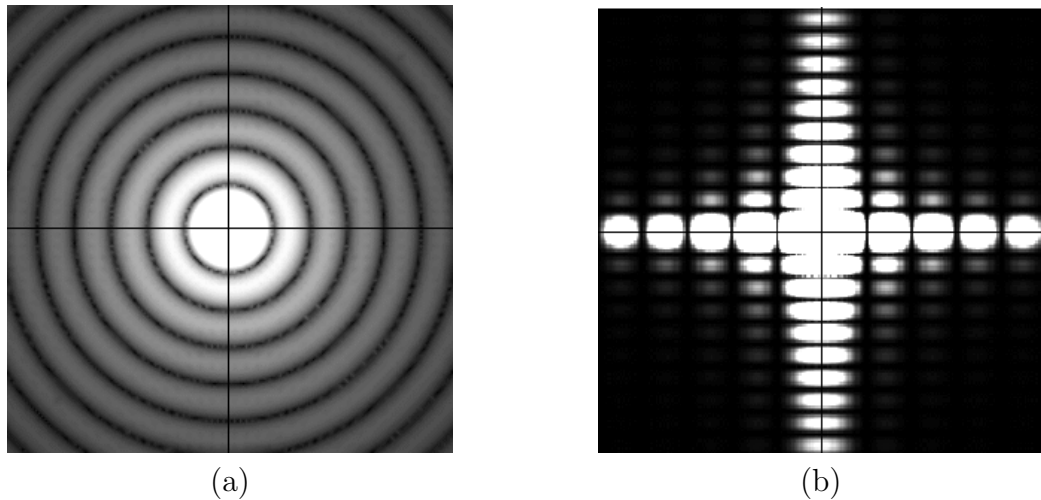


Figure 1.8: Diffraction patterns for circular aperture (a) and rectangular aperture (b).

In imaging systems such as cameras, telescopes or in the case of the human eye diffraction can be calculated using the Fraunhofer (far-field) approximation, where the image plane lies far away from the aperture. It can be shown that for a circular aperture of radius r the intensity is proportional to

$$I(\theta) = I_o \left(\frac{2J_1 \left[\frac{1.22\pi r \sin(\theta)}{\lambda} \right]}{\frac{1.22\pi r \sin(\theta)}{\lambda}} \right)^2 \quad (1.16)$$

where θ the angle between the x and z axes and J_1 is the Bessel function of first order. For the case of a rectangular aperture of width A and height B the intensity is given by the relation

$$I(\theta, \phi) = I_o \frac{\sin(\alpha)^2}{\alpha^2} \frac{\sin(\beta)^2}{\beta^2} \quad (1.17)$$

where $\alpha = \frac{\pi A \sin(\theta)}{\lambda}$, $\beta = \frac{\pi B \sin(\phi)}{\lambda}$ and θ and ϕ the angles between the x and z axes and the y and z axes, respectively. The radiance profiles are shown in fig. 1.9.

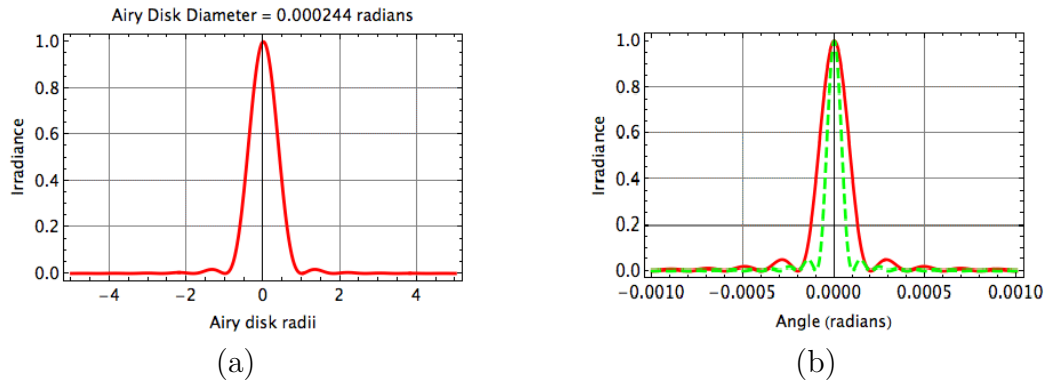


Figure 1.9: Radiance profile for diffraction from circular aperture (a) and rectangular aperture (b). In (b) the different colors represent the different dimensions of the rectangle.

The equations show the strong dependence of diffraction on the size of the aperture and on the wavelength. The size of the airy disk is the lowest solution of equation eq. (1.16), that is $\theta = \frac{1.22\lambda}{2r}$. From the above, for pupil diameters between 1mm and 7mm, it is clear that for the case of the eye diffraction affects only the very central part of the PSF, limiting its effect no more than 3 minutes of arc for the extreme case.

1.4.2 Aberrations

The eye, being an biological organ, is not optically perfect. On the contrary it suffers from significant optical aberrations, both monochromatic and polychromatic, symmetrical and asymmetrical that can severely deteriorate image quality. The most optically significant monochromatics aberrations are defocus, astigmatism, coma and spherical aberration, whereas the polychromatic aberrations can be either longitudinal or transverse.

Chromatic aberrations in the eye are caused by the fact that the refractive index of the eye's optics is wavelength dependent, and can be of two types:

Longitudinal Chromatic Aberrations (LCA) and Transverse Chromatic Aberrations (TCA). In LCA the difference in the refractive power causes shorter wavelength to focus earlier than longer wavelengths, whereas in the case of TCA, unequal refractive compensation at lens surfaces cause a lateral shift of the image, as seen in fig. 1.10(a). The dependence of defocus in diopters on wavelength due to LCA is shown in fig. 1.10(b). From fig. 1.10(b) it is clear that assuming that the wavelength where LCA is zero at 560nm for the average eye, the curve is steeper when moving towards the shorter region of the spectrum, and therefore LCA is stronger for shorter wavelengths. LCA can severely affect the PSF, in the same way that defocus does, whereas TCA simply displace the image and have no effect on the PSF.

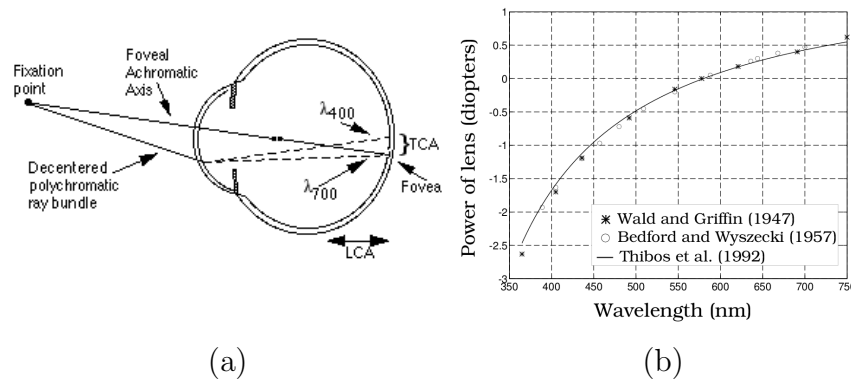


Figure 1.10: (a) LCA and TCA in the human eye. Image taken from Bradley and Thibos. (b) Effect of LCA in diopters with respect wavelength.

Monochromatic aberrations are caused by the curvature of the optics, local deformations of the surfaces and media non-uniformity and describe any deviation from the paraxial approximation. The most common representation for monochromatic aberrations in physiological optics is the Zernike polynomial representation (Noll, 1976), which describes the shape deformation of a plane wavefront when travelling through the eye. Each term Z_n^m , also called mode of the polynomial, corresponds to a specific type of irregularity and it is accompanied by a coefficient c_n^m expressing the magnitude of the specific term/irregularity. Its absolute value corresponds to the RMS wavefront error.

Eye's aberrations depend on pupil diameter, increasing significantly with it, as seen in fig. 1.11. In order to achieve diffraction limited imaging in the eye, the pupil needs to be less than 2mm.

Zernike modes are categorized in low-order, for radial order $n < 3$, and high-order, for radial order $n \geq 3$. The lower the radial order, the more

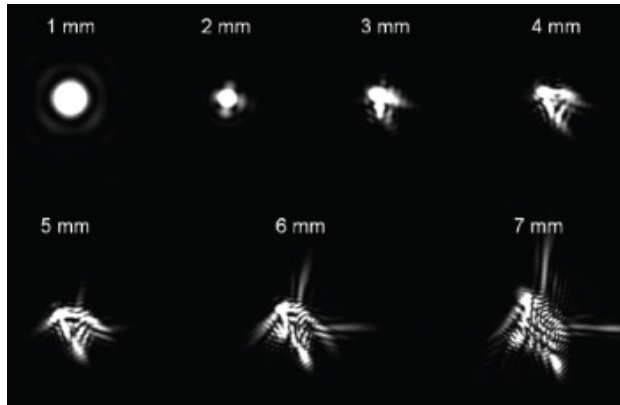


Figure 1.11: Example PSFs showing the dependence of aberrations on pupil size. Image by Roorda.

central the part of the PSF affected by it.

1.4.3 Ocular Straylight

Ocular straylight, often found as intraocular scattering or disability glare, is a term describing elastic scattering of light, occurring in the lens, the cornea and the fundus and affects the Point Spread Function (Van den Berg et al., 2010), in a completely different way than the aberrations and diffraction at the pupil. Scattering essentially redistributes light from the peak of the PSF equally to its outskirts.

Assuming that multiple scattering is negligible in the eye, the total straylight is the sum of the straylight at every part of the eye

$$S(\theta)_{total} = S(\theta)_{cornea} + S(\theta)_{lens} + S(\theta)_{fundus} + S(\theta)_{wall} \quad (1.18)$$

with the cornea, the lens and the fundus with the wall contributing approximately one third each of the total straylight according to Van den Berg et al. (2010), though the fundus contribution depends heavily on wavelength and is restricted to the more central part of the PSF.

Scattering in the ocular media

Scattering occurs due to micro-scale anomalies of the optics at a spatial domain of approximately the same order as the wavelength. It occurs primarily at two sites in the eye; the cornea and the lens, with approximately equal contribution in young healthy eyes (Van den Berg et al., 2010). In both cases, the physical cause is considered to be local variations in refractive in-

dex, however, the actual structures responsible for these fluctuations in the refractive index are not fully determined.

A useful observation that can help in the identification of the structures responsible for the scattering in the ocular media is the fact that the size of the scattering structure has a direct effect on the scattering angle. This dependence derives directly from Maxwell's equations and it is generally called Mie solution, or Mie scattering, and it describes the scattering of the electromagnetic radiation from spherical particles. Depending on the particles size in comparison to the wavelength the scattering phenomenon can be described by either the Rayleigh approximation, the Rayleigh-Gans-Debye approximation, or the Mie approximation.

In the Rayleigh approximation, or Rayleigh scattering, particles need to be sufficiently small, approximately a tenth of the wavelength (Van De Hulst, 2003). Scattering has a strong wavelength dependence $1/\lambda^4$ and is proportional to $1 + \cos^2 \theta$. That means that it is stronger for shorter wavelengths and it is higher at 0 and 180 degrees.

In the Rayleigh-Gans-Debye approximation, an additional restriction is applied; the refractive index of the scattering particle needs to be close to that of the surrounding, or more specifically, the difference between the refractive indexes multiplied by a dimension of the particle is smaller than the wavelength (Van De Hulst, 2003). This approach is generally valid for particles bigger than the Rayleigh approximation. The scattering angle is smaller and the dependence on wavelength weaker, depending on the size of the particle and the refractive index.

Mie scattering, though being the solution to Maxwell's equations is applicable to any scale, historically is defined as light scattering for particles at the order of the wavelength and bigger. There is no wavelength dependence and the scattering angle is lower.

From the qualitative description of the various scattering approximations, it is understood that different structures in the optics scatter at different angles, and therefore in order to properly identify the scatterers one needs to carefully study the scattering spatial pattern and combine it with physiological data on the size of the structures.

There has been a number of theories attempting to explain corneal scattering (Aurell and Holmgren, 1953; Bettelheim, 1977; Maurice, 1957; Goldman and Benedek, 1967; Farrell et al., 1973; Vaezy and Clark, 1991; Boote et al., 2005). One of the main difficulties was that in vivo experiments were not conclusive and in vitro experiments do not necessarily correspond correctly to the real phenomena due to the immense change in the conditions.

Since the corneal stroma occupies the 90% of the total cornea's thickness, it is natural to assume that the inner structure of this layer is responsible for

corneal scattering. The collagen fibrils in the stroma were early identified as the structures responsible for the optical and biomechanical properties of the cornea, but the actual mechanisms are not yet clear. Current understanding of corneal scattering suggests that corneal transparency depends on the packing of the collagen fibrils, but also on the fibril diameter (Boote et al., 2005). Moreover, corneal swelling and scarring can cause the creation of lakes amongst the otherwise tightly packed fibrils leading to a significant increase in scattering (Meek et al., 2003; McCally et al., 2007). Corneal scattering does not appear to have a strong wavelength or age dependence, though changes in the collagen structure have been reported affecting mostly the biomechanical properties of the cornea (Daxer et al., 1998). Finally, corneal scattering can be severely affected by diseases (Meek et al., 2003).

Explaining scattering in the lens has not proven to be easy either, with in vivo experiments not being able to effectively measure the effect of lenticular forward scattering⁵. Microscopic findings from electron micrographs have revealed a number of scattering candidates such as cytoplasmic protein aggregates, fiber cells, multilamellar bodies (MLB), or refractive index differences between fiber cells and the gaps between them (Benedek, 1984, 1971; Hemenger, 1988; Gilliland et al., 2004). In vitro scattering experiments with donor lenses and based on the Rayleigh-Gans-Debye approximation suggested that the structures responsible for the forward scattering must be approximately $1.4 \mu m$ in diameter, excluding smaller particles randomly placed in the lens like proteins, and suggesting fiber cells multilamellar bodies as the most possible candidates, with the later to show an increase in cataract patients (Costello et al., 2007; Gilliland et al., 2001). Lens scattering, contrary to corneal scattering, has a strong dependence on age (Van den Berg et al., 2010) and wavelength (Ginis et al., 2013).

Fundus diffusion

Similarly to scattering in the ocular media, fundus diffusion happens due to micro-changes in the refractive index. The deeper fundus layers and the retina, however, contrary to the eye's optics, are not transparent and light is absorbed depending on its wavelength. Moreover, due to the stratification of the fundus, specular and diffuse reflections can also occur at the interface between the different layers.

Light after going through the optical media it travels through a number

⁵In literature high angle scattering is usually referred to as *backward* scattering or backscattering, whereas low angle scattering as *forward* scattering. Many of the most common ophthalmic instruments used for cataract diagnosis, observe only the back-scattered light.

of layers in the retina and the deeper fundus until it meets the sclera, the last boundary of the eye. Within those layers, as described in page 18, lie elements that show specular reflection, diffusion reflection, absorption and scattering. The main reflectors are

- the Inner Limiting Membrane (ILM) which exhibits both diffuse and specular reflection (Gorrand and Delori, 1999).
- the nerve fiber layer, showing a strong wavelength and directional dependence (Knighton et al., 1989; Knighton and Huang, 1999).
- the photoreceptor layer, showing a characteristic directional dependence in reflectance, known as the Stiles-Crowford effect (Stiles, 1937)
- the Retinal Pigment Epithelium (RPE) which is considered the main reflector in the fundus (Hee et al., 1995; Puliafito et al., 1995).
- the Sclera which exhibits a weak, decreasing dependence on wavelength (Delori and Pflibsen, 1989).

There are four main absorbers in the fundus with the absorption spectra shown in fig. 1.12. More specifically

- the Macular Pigment (MP), located exclusively in the fovea absorbing strictly shorter wavelengths Snodderly et al. (1984b).
- the melanin, found in the choroid and the RPE with a strong wavelength dependence, decreasing monotonically with wavelength. Absorption has been found to have a $\lambda^{-4.5}$ dependence approximately (Gabel et al., 1978) though other studies have shown a weaker dependence (Geeraets et al., 1962). As mentioned earlier RPE melanin shows no correlation to skin or iris melanin, contrary to choroidal melanin which shows a great racial dependence with its density varying up to 1.3 log units for different subjects (Weiter et al., 1986).
- the hemoglobin, located primarily in the choroid. Oxygenated hemoglobin shows a characteristic absorption spectrum, absorbing mainly for middle wavelengths (Berendschot et al., 2003) as seen in fig. 1.12.
- the visual pigment, though it does not usually affect reflectance measurements due to bleaching Delori and Pflibsen (1989).

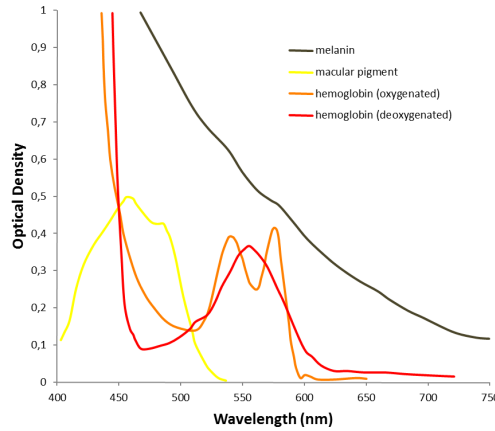


Figure 1.12: Normalized absorption with respect to wavelength for the different ocular absorbers. Replotted from Berendschot et al. (2003) and based on data by van Kampen and Zijstra (1983), Snodderly et al. (1984b) and Gabel et al. (1978).

1.4.4 The CIE glare function for the standard observer

IJspeert et al. (1990) in his paper defines the straylight function as the peripheral part of the the PSF. Indeed, straylight has a low contribution to the PSF at small angles and dominates at angles over 3 degrees depending on the wavelength (Ginis et al., 2012; Van den Berg et al., 2010). Additionally, due to the nature of scattering, rotational symmetry of the PSF is assumed, so that the spatial dependance can be expressed with a single angle θ . The normalization for the rotationally symmetric PSF becomes

$$\int_0^{\frac{\pi}{2}} 2\pi\theta PSF d\theta = 1 \quad (1.19)$$

where the integration limits are between 0 and $\pi/2$ assuming that practically the entire energy of the beam lies in the "forward" scattering region.

Despite the fact that the exact contribution of scattering in the PSF cannot be easily expressed analytically due to the high complexity of the phenomenon, a $1/\theta^2$ dependance had been already suggested by Holladay (1926) and Stiles (1929) in the late 20s. A more complete study of glare and how it affects the PSF was carried out by Vos (1984) and with the follow up studies done by IJspeert et al. (1990), Van den Berg (1991) and Ijspeert et al. (1993) a number of empirical formulas describing the different angle ranges of the PSF were suggested (Vos and Van den Berg, 1999).

The first and simplest formula they presented was the age-adapted Stiles-Holladay formula which was essentially the original relation multiplied by an

age dependent factor (AF)

$$PSF(\theta) = \underbrace{\left[1 + \left(\frac{A}{70}\right)^4\right]}_{AF} \frac{10}{\theta^2} \quad (1.20)$$

where A the age dependent multiplication factor. The age-adapted Stiles-Holladay formula, despite its simplicity, has proven to be a very good approximation of the PSF between 3 and 30 degrees, but fails to describe the more central and the outskirts of the PSF (Vos and Van den Berg, 1997).

Vos and Van den Berg (1997) identified the different structures responsible for straylight and isolated the age and pigmentation dependence in each one of this structures. The PSF for straylight was assumed to have three terms; a basis, an age dependent and a pigmentation dependent

$$PSF(\theta) = PSF(\theta)_{base} + \left(\frac{A}{70}\right) PSF(\theta)_{age} + p \cdot PSF(\theta)_{pigm} \quad (1.21)$$

Assuming that the corneal contribution has no age or pigment dependence, the lenticular has no pigment dependence and the fundus and wall depend on both age and pigmentation, they fitted each part separately based on psychophysical data by Vos and Boogaard (1963) for the cornea, in-vitro data by Van Den Berg and Ijspeert (1995) for lens scattering and attributing smaller the central part to diffraction and aberrations (Ijspeert et al., 1993). The resulted expression for the complete straylight PSF, often found as glare function, reads

$$\begin{aligned} PSF_{CIE} = & [1 - (0.08 (A/70)^4)] \\ & \left[\frac{9.2 \times 10^6}{[1 + (\theta/0.0046)^2]^{1.5}} + \frac{1.5 \times 10^5}{[1 + (\theta/0.045)^2]^{1.5}} \right] \\ & [1 + 1.6(A/70)^4] \left\{ \left[\frac{400}{1 + (\theta/0.1)^2} + 3 \times 10^{-8} \times \theta^2 \right] \right. \\ & \left. + p \left[\frac{1300}{[1 + (\theta/0.1)^2]^{1.5}} + \frac{0.8}{[1 + (\theta/0.1)^2]^{0.5}} \right] \right\} \\ & + 2.5 \times 10^{-3} \times p [sr^{-1}] \end{aligned} \quad (1.22)$$

where θ the angle in degrees, A the age and p a pigmentation coefficient, taking values 0, 0.5 and 1 for black, brown and light eyes respectively.

It needs to be emphasized once again that the above relation is empirical, based on different data and a number of assumptions had to be made. Nevertheless, it has proven to be a good approximation for the standard observer

and a well-behaved function, appropriate to fit experimental straylight data as will be shown in later chapters.

For clinical applications, the PSF is not a practical quantity, so a new quantity called the straylight parameter was defined as

$$S(\theta) = \theta^2 PSF(\theta) \quad (1.23)$$

Often the logarithm of the above quantity is used. As an example, S against the age is shown in fig. 1.13 for $p=0.5$ where there is a quartic dependence of the scattering parameter on the individual's age.

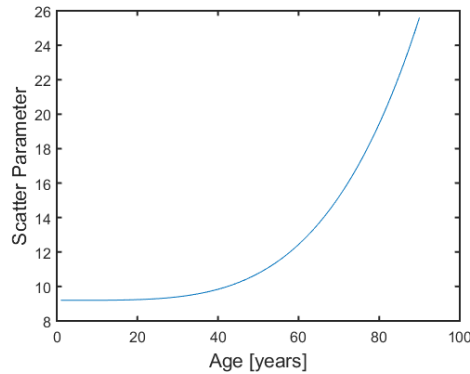


Figure 1.13: Scatter parameter for the CIE glare function given by eq. (1.22) with respect to age at $\theta = 3^\circ$.

1.5 Straylight in Vision and Imaging

The effect of scattering in vision and in fundus imaging is very different than that of aberrations, due to the fact that scattering affects also the wide angle part of the PSF. While the most central part of the PSF, up to about 1.2 arcmin, is responsible for visual acuity and up to about a third of a degree for contrast sensitivity where diffraction and aberrations are dominant, scattering only becomes dominant after about 1 degrees (Van den Berg et al., 2010). Scattering in vision is perceived as a veil of light covering the entire image and it depends strongly on the dynamic range of the image. One of the most common conditions where straylight occurs is in night driving where the presence of the bright headlights from the opposite vehicle in a dark surrounding causes a severe loss of detail, depending on the optical media of the individual's eye. Straylight has a very weak effect on visual acuity and relatively weak effect on contrast sensitivity but affects strongly contrast

sensitivity in the presence of glare (Van den Berg et al., 2010), where visual function is tested with the respect to the intensity of a glare source.

The effect of straylight in vision is shown in fig. 1.14(a)-fig. 1.14(c) where the effect of different amounts of scattering is shown for the same image, illustrating a night driving scenario. The darker features of the image depending on the amount of scattering can suffer a significant contrast loss, due to the presence of a glare source, such as the headlights of the car. Features closer to the bright light source are affected, as it can be seen in fig. 1.14(c) where the turn sign on top of the car is no longer visible, whereas the identical turn sign in the middle of the image remains visible.

The importance of the dynamic range, or the presence of a *glare source* in the scenery is shown in fig. 1.15(a)-fig. 1.15(c), where, although the scattering media were the same as in fig. 1.14 the effect is significantly lower.

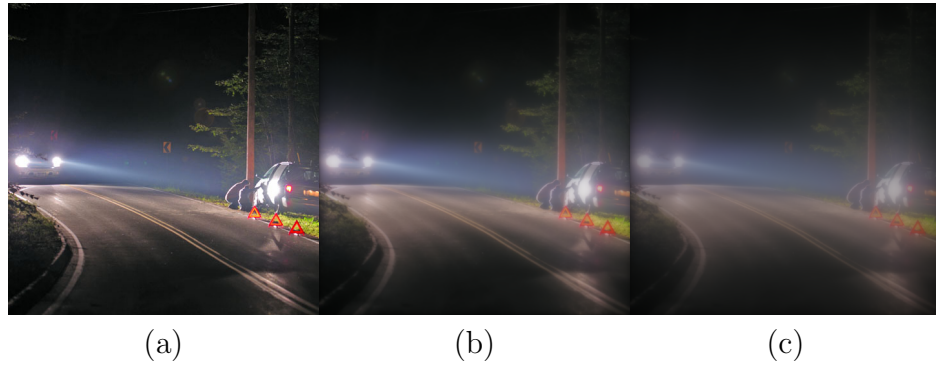


Figure 1.14: The effect of scattering in an image with high dynamic range, for no scattering (a), medium scattering (b) and high scattering (c).

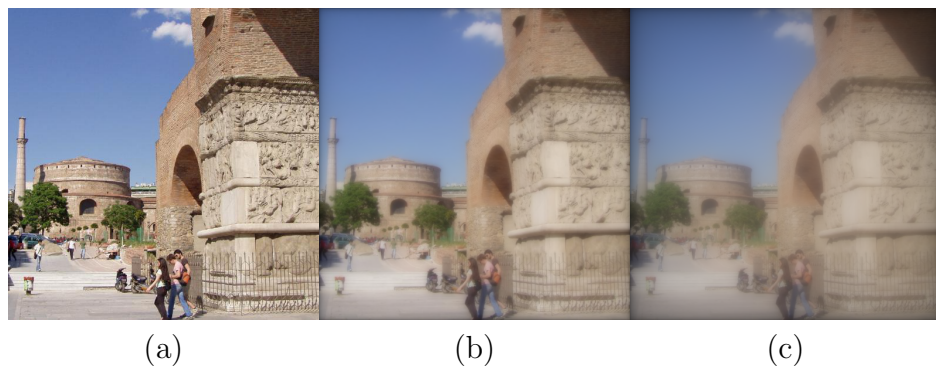


Figure 1.15: The effect of scattering in an image with medium dynamic range, for no scattering (a), medium scattering (b) and high scattering (c).

Similarly, intraocular scattering affects light exiting the fundus, like in the case of fundus photography. In cases of subjects suffering from cataract

severe scattering can lead to important detail loss and the fundus image can suffer greatly.

1.6 Overview of experimental methods

1.6.1 The Double-pass Method

The double-pass method is a simple, yet ingenious method for the optical characterization of the eye. It was introduced for the first time more than half a century ago by the french scientist Flamant in her doctoral thesis (Flamant, 1955) with its principle of operation based on Helmholtz's ophthalmoscope. Since then, it has been extensively used for the study of the retinal image quality and the MTF of the human eye (Campbell and Gubisch, 1966; Artal et al., 1995b; Santamaría et al., 1987; Williams et al., 1994; Iglesias et al., 1998; Coletta et al., 2003; López-Gil and Artal, 1997; Bueno and Artal, 1999; Losada and Navarro, 1998), the study of intraocular scattering (Artal et al., 2011; Ginis et al., 2012, 2013, 2014), but also for the study of the fundus and its pigments (Christaras et al., 2015; Saad et al., 2010; Delori and Pflibsen, 1989; Hammer et al., 2003; O'Brien et al., 2013; Bour et al., 2002). The technique is based on the recording of an image of a pattern, usually a point source, after it is reflected on the retina, thus passing twice through the optics of the eye. By analyzing the recorded image, one can extract important optical metrics of the eye such as the Modulation Transfer Function (MTF), the Point Spread Function (PSF) and the Line Spread Function (LSF). An example of a double-pass system, one of the first double-pass systems ever built, by Campbell and Gubisch in 1966 is shown in fig. 1.16, used to reconstruct the LSF of the eye.

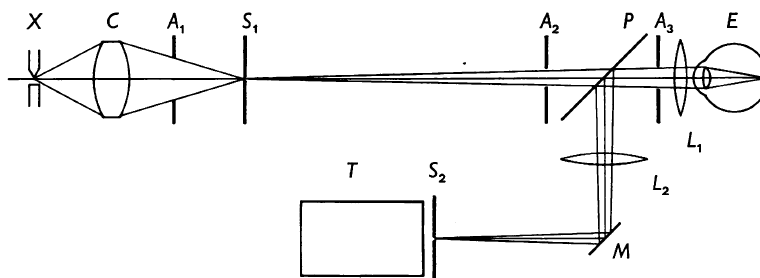


Figure 1.16: One of the first double-pass systems, built in 1966. Light from slit S_1 is projected and the retina and its image is recorded through slit S_2 by the photomultiplier T .

In the late 80s, Santamaría et al. (1987) managed to reconstruct the 2-

dimensional OTF and the PSF of human eyes using the double-pass technique and shortly after that, Artal et al. (1988) in continuation to the latter study, managed to retrieve the ocular aberrations from the PSF data. In the following years, the double-pass technique formed the basis for novel techniques with more important that of adaptive optics, which has now become the standard for high resolution, high quality imaging of the fundus (Fernández et al., 2001; Hofer et al., 2001; Fernández et al., 2006; Choi et al., 2006).

Additional attention, however, needs to be taken when using the double-pass method, especially when studying non symmetrical aberrations. An important aspect that needs to be taken into account for the proper characterization of the quality of the optics, is the symmetry of the optical setup. In a study by Artal et al. (1995b), the authors, based on the inconsistency of the PSFs calculated by the subjective and the objective methods, concluded that, in a symmetrical setup, odd aberrations such as coma are canceled in the second pass, thus always producing a symmetric aerial double-pass PSF. In a following study the authors showed how to break the system's symmetry, in order to avoid that effect (Artal et al., 1995a). Nevertheless, it needs to be pointed out, that despite the effect on the PSF, the MTF of the system is not affected by the double-pass effect. That being said, when studying symmetric phenomena (such as straylight; see following chapter) the configuration of the system doesn't affect the measurement.

1.6.2 Heterochromatic Flicker Photometry

There is a number of psychophysical methods and procedures to measure the human spectral sensitivity. The Heterochromatic Flicker Photometry (HFP) technique, is one of the most well established and extensively used technique for the measurement of the spectral sensitivity of the visual system, and along with the Minimally Distinct Border (MDB) and the Heterochromatic Modulation Photometry (HMP) is considered to give the more reliable results (for a review see (Lennie et al., 1993)). The HFP method dates back to the early 1900s and is coined to Frederick Ives and apart from the study of the spectral sensitivity has been used for more than three decades in the measurement of the Macular Pigment Optical Density (MPOD) (Werner et al., 1987; Bone and Sparrock, 1971; Hammond et al., 1997b; Beatty et al., 2001; Bone and Landrum, 2004; Snodderly, 2004; Tsika et al., 2011). A number of commercial HFP based apparatus like the MPSII(QuantifEye;Tinsley Precision Instruments Ltd., Croydon, Essex, UK) or the more recent Macuscope (Macuvision Europe Ltd., Lapworth, Solihull, UK) are well established in the clinical evaluation of MPOD.

In the HFP technique a disk of a specific diameter alternates between

two different colors with a fixed frequency. The radiance of one of the two colors is variable and controllable by the subject, whereas the other color is kept fixed. When the luminance⁶ of the two lights becomes equal, the field, depending on the flicker frequency, no longer flickers or exhibits minimal flickering.

In HFP the alternating test field is superimposed on a appropriate background. The choice of the color and intensity of the background has been shown that it can affect greatly the responses and consequently alter the results, and it has to be chosen according to the quantity under examination (Eisner and Macleod, 1981; Stockman et al., 1993; Kaiser and Comerford, 1975). By cleverly selecting the color background, one can selectively exclude or include particular cone classes and eliminated any possible sources of fluctuations in the measurements (Sun et al., 2001). In macular pigment studies for instance, a blue background is often used in order to prevent the rods and s-cones from participating in the detection (Loughman et al., 2010b; Snodderly, 2004).

1.7 Motivation of the thesis

The present thesis essentially tries to tackle the optical phenomenon of intraocular scattering both from the visual perspective and the clinical one. In the first part of this work, simulations were carried out in order to understand the behavior of the ocular fundus for different parameters, like wavelength and pigmentation, as well as to explore the spatial domain of dominance of scattering occurring at different parts of the eye. Based on the results of the theoretical analysis, two different experiments were set up, one to study the visual effect of fundus diffusion and a second one to study the effect of straylight in fundus imaging and come up with the method that could compensate for that scattering. Finally, as a practical example, the method of scattering compensation in fundus imaging was applied in the macular pigment measurement.

⁶Not to be confused with radiance. Luminance, is the the radiance weighted by the spectral sensitivity of the human visual system

Light diffusion in the fundus

In this chapter, a theoretical study of fundus diffusion is done using the Monte Carlo simulation. The simulation of light propagation in the fundus was based on a simplified 4-layer fundus model and physiological data from previous studies. The effect of scattering in the optics was introduced to the simulations and the two phenomena were studied qualitatively. More specifically, the objectives of this chapter were the following:

- The simulation of the effect of fundus diffusion and how different pigment densities affect the back-scattered from the fundus light.
- A comparison of the effect on the point spread function of fundus diffusion and scattering and an estimation of the critical angle where scattering becomes dominant.

2.1 The Monte Carlo simulation

Monte Carlo method, also known as the random sampling method, was introduced in 1940 by Stanislaw Ulam and John von Neumann, for the study of neutron propagation in matter (Metropolis and Ulam, 1949; Metropolis, 1987) and it became one of the most important tools in physics ever since.

Although there is not a single definition for the MC method, an appropriate definition in this case would be the following: a stochastic model in which the value of a physical quantity is related to the expected value of a single random variable or a number of random variables. The core of the Monte Carlo method is the way these expectation values are estimated: by averaging a number of samples where the random variables are represented by random numbers following its distribution. From the above, one can see

that there are two main parameters that would affect greatly how accurate the simulation is: the correct choice of random variables and the number of samples averaged. The method can be used in both stochastic phenomena like the propagation of a particle through matter, and non-stochastic phenomena where the problem conditions make the Monte Carlo approximation the only feasible way to tackle the problem.

Monte Carlo simulations have been used extensively in skin research, modelling light propagation in the various layers of skin (Golshan et al., 2011; Patwardhan et al., 2005; Simpson et al., 1998; Kirillin et al., 2010), but also in cancer therapy to calculate the correct dose applied to a specific tumor (Fippel and Soukup, 2004; Sechopoulos et al., 2008). In physiological optics, a number of studies using the Monte Carlo algorithm for the estimation of optical properties of the ocular fundus and the simulation of light propagation in the fundus have been carried out (Preece and Claridge, 2002; Orihuela-Espina et al., 2003; Hammer et al., 1995; Guo and Tan, 2015).

2.2 A model of fundus reflectance

The objective of this study was to simulate the propagation of photons in the ocular fundus, and more specifically to estimate the distribution of the back-scattered light from the deeper fundus layers. For that purpose a simplified 4-layer model of the fundus was considered, where photons could either be absorbed or scattered. The model comprised of the Photoreceptor Layer, the Retinal Pigment Epithelium (RPE), the Choroid and the Sclera, and taking into account both scattering and absorption in each layer we computed the back-scattered light at each point at the surface of the retina. An schematic of the model is shown in fig. 2.1. In order to take into account reflections happening at the interfaces where the light meets the retina and exits the sclera, two more layers were introduced with the appropriate refractive indexes, which represented the vitreous before the retina and the tissue after the sclera.

For each layer an absorption coefficient μ_a and a scattering coefficient μ_s were defined, as well as a thickness and a refractive index. The absorption and the scattering coefficient had a strong dependence on the wavelength. The highest dependence on wavelength was due mostly to the two main absorbers in the fundus, the melanin and the hemoglobin (see chapter 1). Finally, an additional parameter g was introduced to describe anisotropy of scattering in the media.

Furthermore, and in order to keep the model relatively simple, two assumptions were made: a. the Stiles-Crawford (SC) effect was neglected and

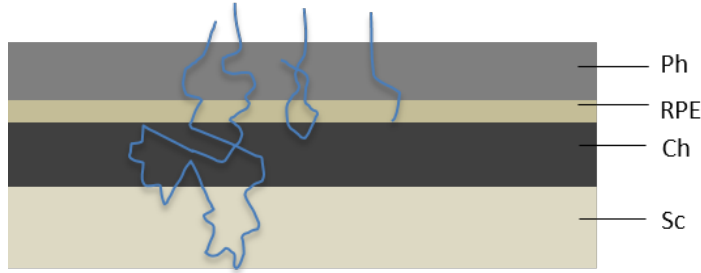


Figure 2.1: Simple 4-layer model of the fundus used for the Monte Carlo simulation. The layers from top to bottom are: Photoreceptor Layer, RPE, Choroid and Sclera.

b. diffusion was considered isotropic, i.e. the phenomenon is rotationally symmetric.

Finally, it needs to be underlined that diffusion in the fundus can also be studied analytically. A general analytical study for light propagation in turbid-media can be found in Kienle and Patterson (1997). However, the calculation for a multi-layered tissue like the fundus is highly non-trivial. A comparison of an analytical and a Monte Carlo method for the study of fundus light diffusion can be found in Ramachandran et al. (2004).

2.3 Photon packet propagation considerations

In order for the simulation to accurately approximate the physical quantities, all physical aspects of photon propagation in the multi-layered tissue need to be taken into account. Below the most important rules of the simulation are shortly described. A more in depth description can be found in Wang and Jacques (1992).

- **Specular Reflection** For the simulation, the photon, or more precisely the photon packet, was always introduced orthogonally to the tissue with an initial weight W equal to 1. When the photon packet meets the interface between the vitreous and the photoreceptor layer it can either be specularly reflected or transmitted. The specular reflectance for naturally polarized light can be derived directly from the Fresnel equations and it reads

$$R_{sp} = \left(\frac{n_1 - n_2}{n_1 + n_2} \right)^2 \quad (2.1)$$

where n_1 and n_2 the refractive indexes of the two media. The new photon weight W' now naturally becomes

$$W' = 1 - R_{sp} \quad (2.2)$$

with the photon packet being "lighter" by $W - W'$.

- **Step size** Another essential parameter for the simulation is the step size, the numerical equivalent of the mean free path. Instead of choosing a fixed step size, which could vastly affect the results of the simulation, a different approach was followed: The step size followed Beer's law with a probability distribution proportional to $e^{-(\mu_a + \mu_s)\Delta s}$. It reads

$$\Delta s = \frac{\ln \xi}{\mu_t} \quad (2.3)$$

where ξ a random variable, uniformly distributed between 0 and 1 and $\mu_t = \mu_a + \mu_s$ expressing the total interaction.

- **Photon moving** The moving of the photon in the three dimensional space is done following the equations

$$x' = x + \mu_x \Delta s \quad (2.4a)$$

$$y' = y + \mu_y \Delta s \quad (2.4b)$$

$$z' = z + \mu_z \Delta s \quad (2.4c)$$

where $\mu_{x,y,z}$ the directional cosines.

- **Photon absorption and scattering** After the introduction of the photon packet into the tissue, at each step it is split into two parts; a fraction of the packet is absorbed and what is left interacts. The absorption fraction, or else the amount of deposited weight at each step is given by the formula

$$\Delta W = W \frac{\mu_a}{\mu_s + \mu_a} \quad (2.5)$$

and the resulting weight will be $W' = W - \Delta W$. The photon packet with weight W' undergoes scattering with a deflection angle θ given by the relation

$$\cos \theta = \begin{cases} \frac{1}{2g} \left[1 + g^2 - \left(\frac{1 - g^2}{1 - g + 2g\xi} \right)^2 \right], & g > 0 \\ 2\xi - 1 & g = 0 \end{cases} \quad (2.6)$$

where ξ a random variable. The azimuthal angle ψ is distributed uniformly in the $[0, 2\pi)$ interval

$$\psi = 2\pi\xi \quad (2.7)$$

- **Reflection at the boundary/interface** In order to account for reflection at the boundary, the step size Δs is computed with respect to the distances from the upper and lower boundaries. Similarly, the effective step size is adjusted accordingly to account for reflection at the interface. Additionally, internal reflection is also taken into account depending on the angle of incidence at the interface. The internal reflection is calculated using the Fresnel equations and, again, the photon weight is adjusted accordingly as above.
- **Photon termination** There is a number of phenomena that can happen and lead to the termination of the photon packet. It can be reflected out of the tissue or get transmitted entirely through the full depth of the tissue and escape. For a photon in the tissue, ideally termination happens when the photon weight becomes 0. Nevertheless, for very low weights, very little information about the propagation is acquired and it makes the simulation more expensive computationally without adding any useful information. A very straightforward solution to overcome that was to set a lower limit for the weight such that when a photon packet reached that limit was considered fully absorbed. However, such a solution would violate conservation of energy and would skew the absorption profile. In order to deal with that, a technique called roulette was applied, giving to each photon packet reaching that limit once chance in m of surviving with a new weight $m \cdot W$ or the weight is set to zero and the propagation is terminated.

The flowchart in section 2.3 depicts the algorithm for the Monte Carlo simulation in multi-layered tissue, following the rules described above. Briefly, first the photon packet is initialized, then the distance to the first interaction event is determined and it is compared to the distance to the boundary. If it hits the boundary then the unfinished step is stored and the photon moves directly to the boundary where it either gets reflected or transmitted. In the opposite case the photon moves a step and the absorption and scattering operations act upon it. In any case (reflection, transmission, absorption/scattering) the photon weight is calculated. If it is higher than a preset value then the new step size is calculated and the process repeats, whereas in the opposite case, the photon goes through the roulette procedure where if it survives the new step size is calculated and the propagation repeats. In case the photon does not survive the roulette a new photon packet is created and is propagated through the media. The process repeats until all photon packets are propagated through the tissue.

The simulation was done using a C program which simulates the propagation of light in the tissue for multi-layered tissue developed by Wang and

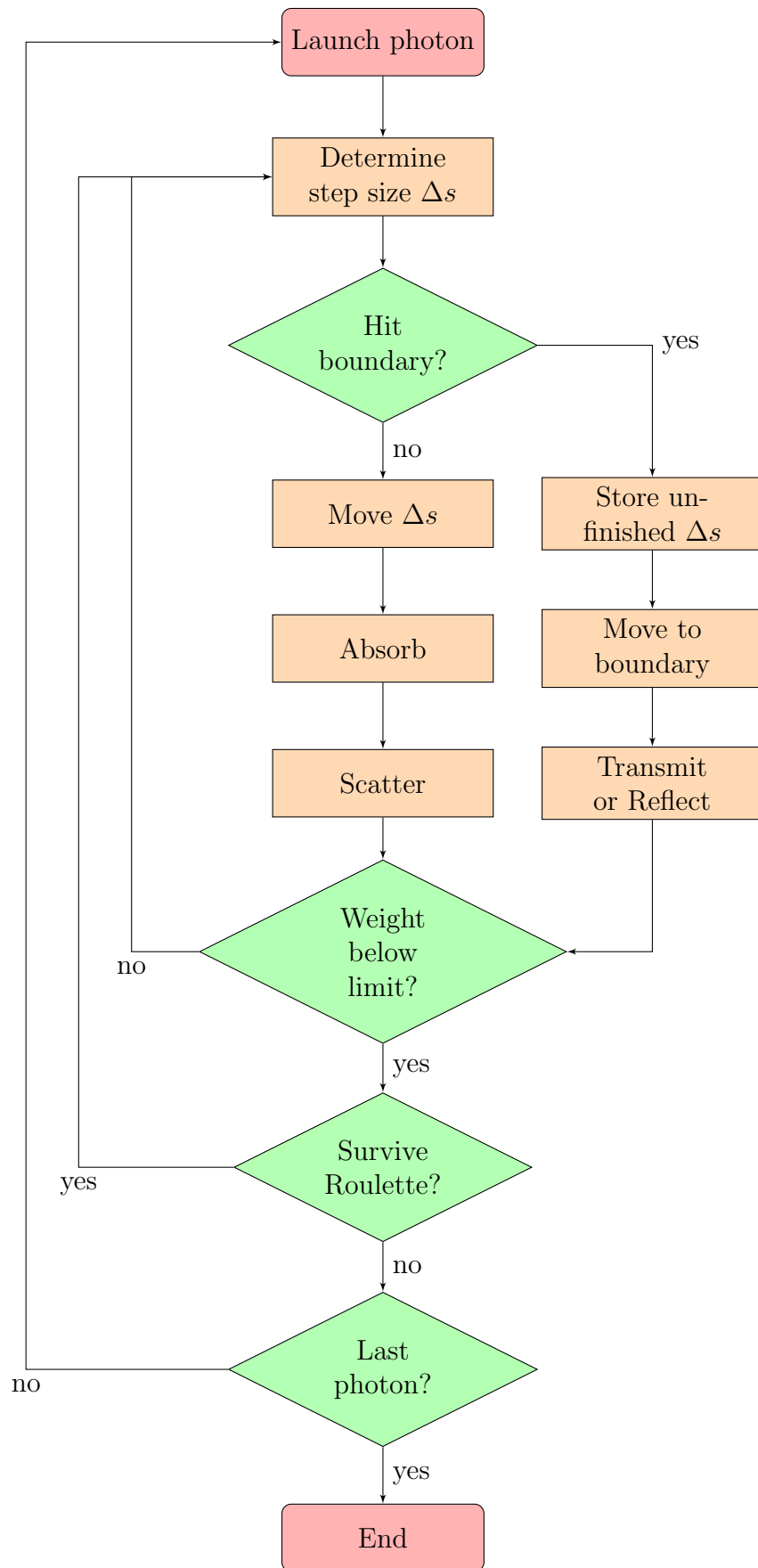


Figure 2.2: Flow chart of the Monte Carlo simulation describing photon packet propagation in the fundus.

Jacques (1992). MATLAB wrappers were developed for the presentation of the results and the convolution of the resulting PSF of the fundus with the projected image. The values for the coefficients used in the simulation were taken from Hammer et al. (1995), which were extracted through the ex-vivo measurement of the transmittance and the reflectance of isolated layers of the fundus and the application of the inverse Monte Carlo simulation. Hammer's study is probably the single one that studies both the absorption and scattering coefficient for 4 different layers of the ocular fundus.

The simulation also depended on the definition of the grid parameters and the photon number. Depending on the minimum thickness of the layer, an appropriate grid step on the transverse (z-axis) direction was set. Fortunately, due to the immense computational power of today's computers, even with an entry-level laptop it was possible to perform various simulations for very large number of photon packets and for various grid parameters and see how they affect the results¹.

The effect of the number of photons in the simulation can be seen in fig. 2.3, where 4 different photon packets number are presented with the rest of the parameters being identical. As expected the noise is inverse proportional to the number of photon packets.

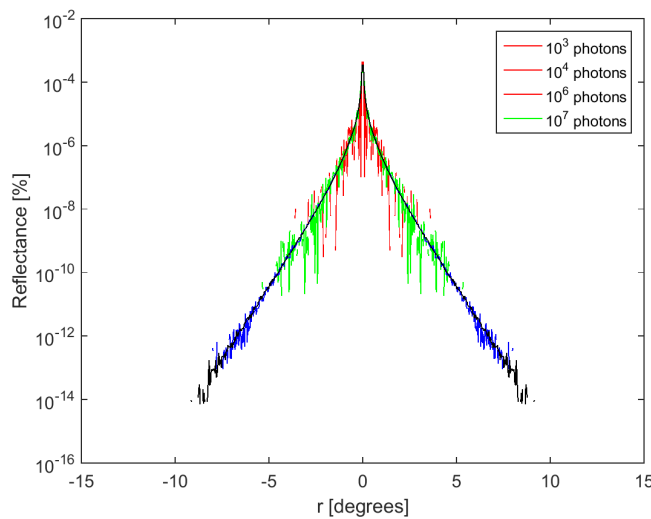


Figure 2.3: The effect of photon packet number in the Monte Carlo simulation.

¹To put this into perspective, Hammer et al. (1995) in their work stated that every simulation with about 100.000-500.000 photons lasted about 4 hours, whereas a simulation with 10.000.000 with an ordinary low-end laptop lasted only a few minutes.

Depending on the spatial resolution desired, the grid spacing on the plane parallel to the retinal plane needs to be set accordingly. Note, however, that the total reflectance does not depend on that, but for a higher spatial resolution a higher number of photon packets is needed. Additionally, the program stores the exit angle a of the photon packet. The appropriate resolution in the angle domain is set by defining the parameter da which is given by dividing the maximum angle ($\pi/2$) to the number of points in the angle domain. The coordinate system for the simulation is therefore defined by 3 coordinates: the normal to the fundus, the parallel to the fundus and the angle from the normal. Figure 2.4 shows a 2D visualization of photon fluence in the fundus at 550nm and 650nm.

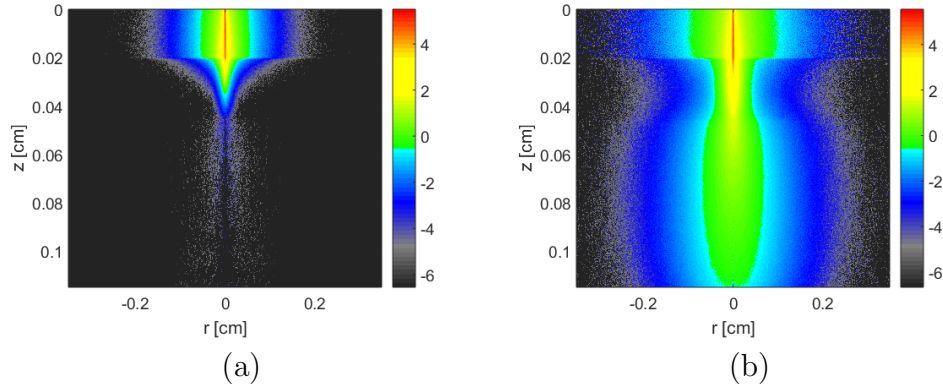


Figure 2.4: Photon fluence in the fundus at 550nm (left) and 650nm (right).

The fluence in fig. 2.4, represents the probability probability per unit length, can be expressed through the relation

$$\phi(z, r) = \frac{A(z, r)}{\mu_a} \quad (2.8)$$

where $A(z, r)$ the absorption in the 2 dimensional grid. Even with a simple observation of the fluence at 550nm with that at 650nm one can qualitatively observe that fundus diffusion at 550nm is much lower compared to that at 650nm, at every single one of the four simulated layers. This is a direct result of the absorption spectra of the pigments, as seen in fig. 1.12 on 29.

2.4 Fundus diffusion at different wavelengths

The objectives of this simulation were the following: firstly, to compare fundus diffusion at the two different wavelengths and secondly to test the effect

of changes in melanin pigmentation in fundus diffusion for the same wavelengths, by increasing the amount of choroidal melanin. The latter aims to simulate the different choroidal melanin levels found amongst the population. To put this into a more realistic perspective, the first part studied changes in diffusion for two different wavelengths for a single individual, whereas the second changes in diffusion amongst the population, based on their iris pigmentation.

For that purpose, four different simulations were run for four different sets of coefficients. In order to study the effect of choroidal melanin changes, the absorption coefficient of the choroid was increased by a factor of 2 for the above wavelengths. Although the doubling of the absorption was rather arbitrary, it has been shown that choroidal melanin concentrations amongst individuals exhibit indeed such variability (Koblova et al., 2005; Wakamatsu et al., 2008). Nevertheless, the objective was primarily to see the relative effect in the PSF for the two wavelengths, rather than the absolute effect in fundus reflection. The coefficients used for the study along with all the parameters of the simulation can be found in appendix A where the complete input file is shown.

The simulated PSFs for fundus diffusion at 550nm and 650nm are shown in fig. 2.5, where at high angles the PSF for 650nm is 3 orders of magnitude higher than that for 550nm.

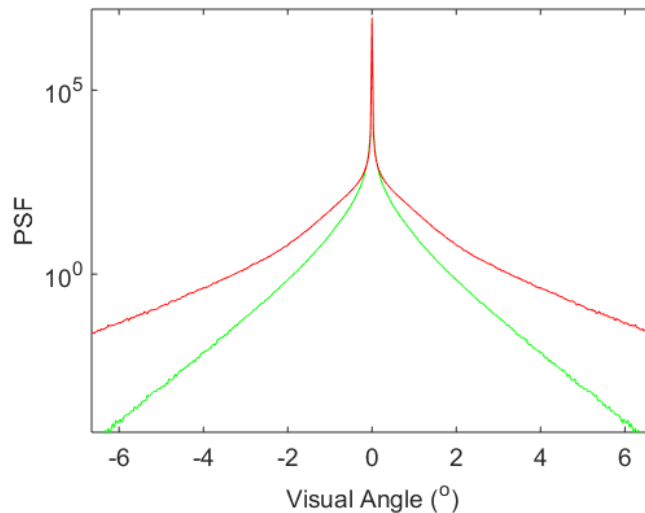


Figure 2.5: Simulated PSF for fundus diffusion at 550nm (green) and 650nm (red).

In order to simulate a more realistic scenario and be able to compare the simulated results with actual experimental data, a convolution of the simu-

lated PSFs with a series of uniform disks of various diameters was applied. By doing that the study of the effect is now far more clearer than simply examining the simulated PSFs. Two examples of such an operation is shown in fig. 2.6(a) and fig. 2.6(b) where the simulated PSF at 550nm and at 650nm were convoluted with a uniform disk of 7 degrees radius.

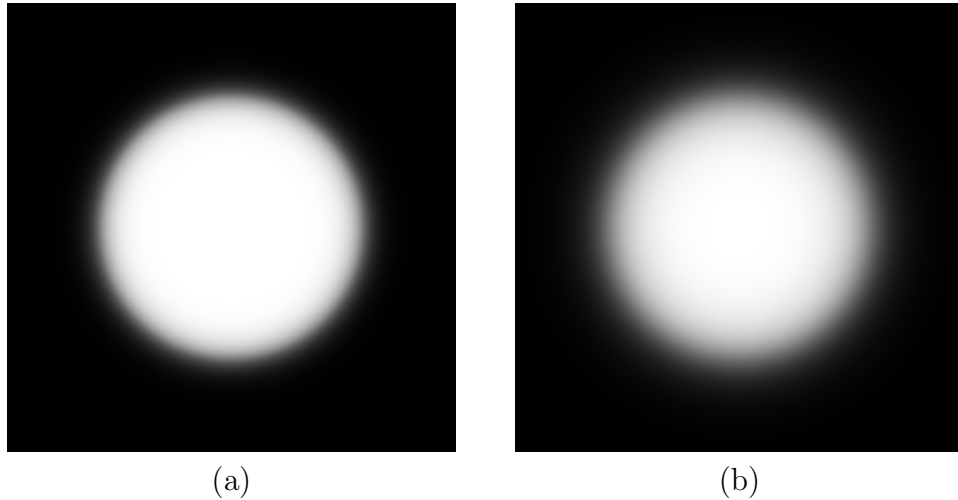


Figure 2.6: Simulated disk of 14 degrees diameters after being diffused in the fundus at 550nm (a) and 650nm (b).

2.5 The effect of choroidal melanin

The effect of fundus diffusion was simulated at 550nm and 650nm for two different values of the absorption coefficient of the choroid for a sequence of 20 uniform disks ranging from about 10 minutes of arc to 7.34 degrees and the intensity at the center of each disk was measured and plotted against its size in fig. 2.7(a) and fig. 2.7(b), for 550nm and 650nm respectively. This result yields an important piece of information on the spatial behavior of straylight and, as will be shown in the next chapter, it can be used to extract the wide-angle PSF of a system.

From fig. 2.7 one can see that the effect of the higher choroidal absorption in fundus diffusion is clearer for bigger fields up to a certain degree where the curve exhibits a plateau and the effect does no longer contribute. Consequently the effect scattering has on the back-scattered light depends on the the field size.

All four different cases depicted in fig. 2.7(a) and fig. 2.7(b) can be seen in fig. 2.8. This result, is one of the two main results of the simulations and

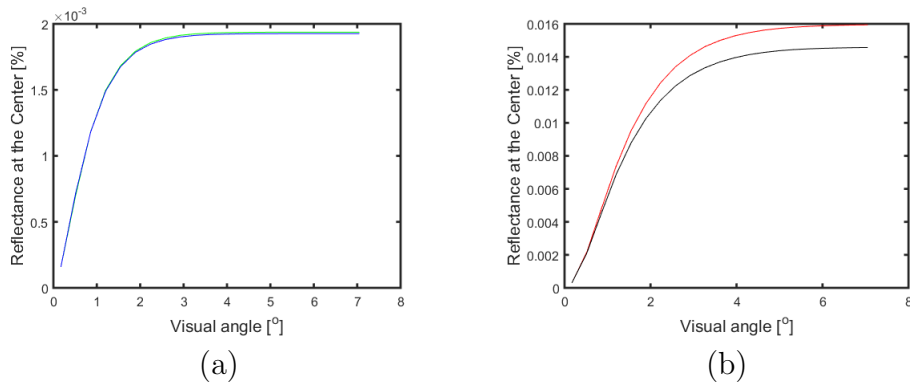


Figure 2.7: Simulated intensities at the center with respect to disk radius at 550nm (a) and 650nm (b) for two different melanin values. The different colors represent different choroidal melanin values.

later on it will be measured experimentally based on the fundus reflectance measurements of actual subjects.

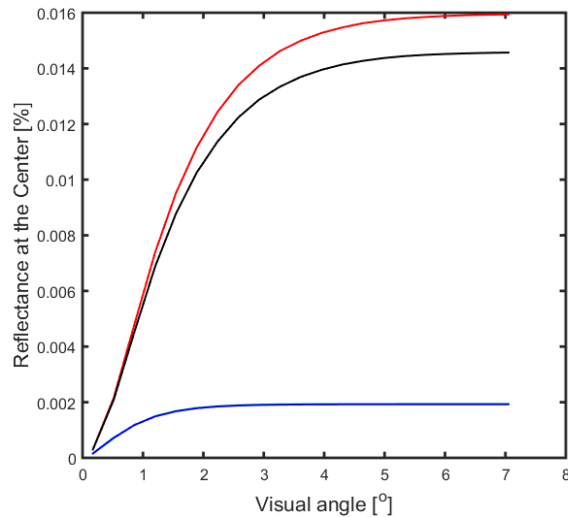


Figure 2.8: Simulated intensities at the center with respect to disk radius at 550nm and 650nm for two different melanin values. In red and black the low melanin value and the high melanin value at 650nm respectively. At 550nm the respective curves, in green and blue respectively, are practically indistinguishable.

2.6 Separating scattering in the ocular media and diffusion at the fundus

As seen in chapter 1, there are four main optical phenomena contributing to the PSF: diffraction, aberrations, fundus diffusion and scattering in the optics, hereby referred to simply as scattering. Diffraction and aberrations affect the very central of the PSF, whereas diffusion in the deeper fundus layers and scattering become important after 1 degrees. Scattering, at almost all wavelengths, starts becoming dominant over 3 degrees as shown by Ginis et al. (2013), where the ratio of the PSF at red to the PSF at green is plotted against the angle. The corresponding figure can be seen in fig. 2.9.

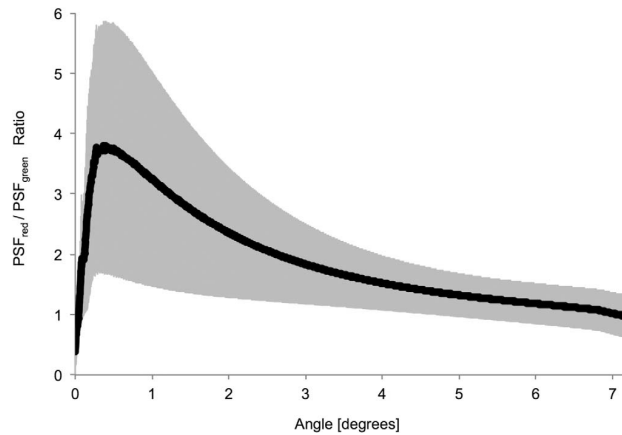


Figure 2.9: Ratio of the PSF at red wavelengths to the PSF at green wavelengths. Gray area corresponds to 2 standard deviations. Plot retrieved from Ginis et al. (2013).

Distinction between the scattering and the diffusion part of the PSF is not trivial and depends heavily on wavelength, since diffusion can be one order or more higher within the visible spectrum as the simulations have shown us.

A straight-forward way to study the range of impact of the two phenomena is to compare the PSF of scattering with that of fundus diffusion for a particular wavelength though the simulations. This is shown in fig. 2.10 where the simulated PSFs using the MC algorithm for 550nm and 650nm and the PSF_{CIE} for $A=40$ and $p=1$ are plotted. From fig. 2.10 one can easily see fundus diffusion falls rapidly after about 2 degrees for 550nm, whereas for 650nm the decrease starts happening at almost 4 degrees.

Another way that could highlight the domain of dominance is the examination of the intensities at the center of disk of increasing field size and the finding of the field size where the contribution of scattering at the intensity

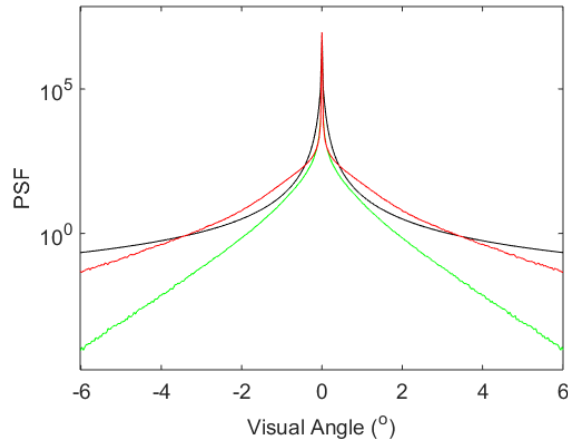


Figure 2.10: Simulated PSFs for fundus diffusion at 560nm (green) and at 650nm (red), and the CIE glare function (black).

at the center starts becoming significant. The above test was done using the simulated disks from section 2.5 before and after being convoluted twice² with the PSF_{CIE} (see section 1.2.1) in order to simulate the double pass of the light in the eye. The fundus effect contribution in the PSF_{CIE} was taken to be negligible. It needs to be noted here that technically, in order to correctly simulate the effect one needs to convolute the initial disk with the scatter PSF, then with the fundus diffusion PSF, and lastly, perform a correlation with the scatter PSF, expressing this way the geometrical inversion of the initial image-disk. However, due to the nature of scattering and fundus diffusion, the PSF is assumed to be rotationally symmetric, and thus correlation and the convolution are identical.

In fig. 2.11 the intensity at the center with only fundus diffusion present and the intensity at the center with both fundus diffusion and scattering are plotted against the disk radius at 550nm. In figure fig. 2.12 the same quantities are plotted for 650nm. In the figures, in order to stretch out the effect of scattering, and to make more clear the angle where the effect of scattering becomes dominant, a small y-offset was introduced at the total curve to compensate for the light lost. This way, one can directly observe the effect of scattering by finding where the total curve diverges from the diffusion curve. It is clear from the plots that at 550nm fundus diffusion stops being important at about 2 degrees, significantly earlier than at 650nm where the high transmittance of the fundus permits light even for the very

²The order of the convolution is of no importance, due to the commutative and associative property of convolution.

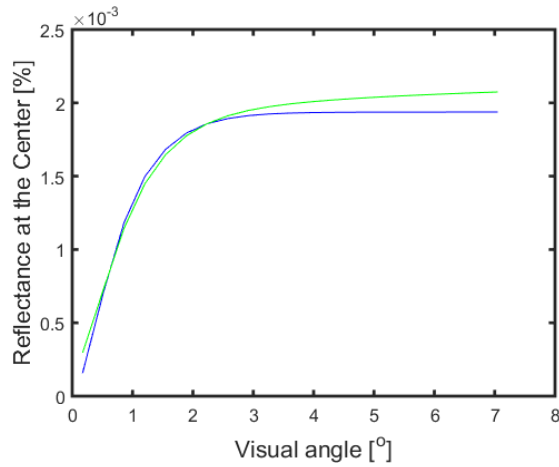


Figure 2.11: Intensity at the center of the disk with respect to disk radius with fundus diffusion only (blue) and with fundus diffusion and lens scattering (red) at 560nm.

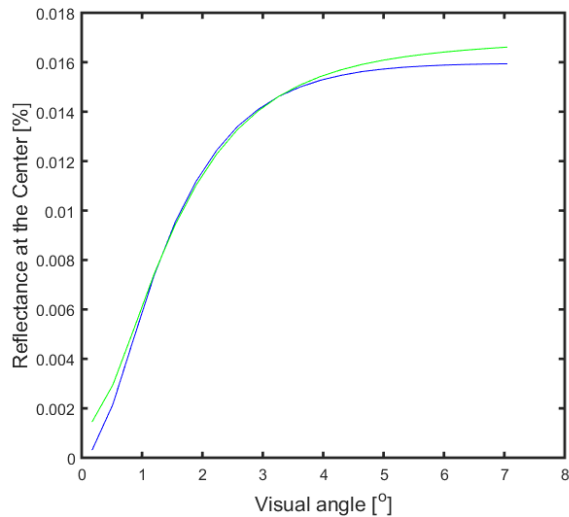


Figure 2.12: Intensity at the center of the disk with respect to disk radius with fundus diffusion only (blue) and with fundus diffusion and lens scattering (red) at 650nm.

outskirts of the disk to contribute to the intensity at the center of the disk.

From the two plots two main observations can be made:

- At 560nm scattering becomes relevant only after 2 degrees, whereas at 650nm at about 4 degrees. That essentially means that, at longer wavelengths, any scattering effect under 4 degrees is masked, at least partially, by fundus diffusion.
- In lens scattering measurements, it is preferable to use shorter wave-

length in order to minimize the effect of fundus diffusion. Yet, even at short wavelengths, in order to come to a valid observation about scattering one needs to examine solely the change in the PSF after at least 3 degrees.

Chapter 3

Fundus diffused light and its effect in vision

This chapter focuses on two main topics:

- The investigation of the spatial and spectral characteristics of diffuse light in the fundus, based on experimental data extracted using a double-pass setup. This was done through the study of the increase of diffuse light at a central retinal patch when uniform bright discs of different field sizes were projected on to the fundus for two different wavelengths (560nm and 650nm). The setup was based on the double-pass principle, for the optical measurement of the reflected light from the fundus (Ginis et al., 2012, 2013; Zagers et al., 2002). Since diffusion depends on wavelength, different wavelength results in changes in the relative intensity of the central patch when measured optically.
- The study of fundus diffusion in vision, and more specifically on color sensitivity. The Heterochromatic Flicker Photometry (HFP) method was used at the same spectral and spatial conditions with the optical setup in order to determine if this relative increase in diffuse light is associated with a proportional increase in sensitivity.

The results of this chapter were published in Christaras et al. (2015)

3.1 Subject classification

Six subjects, all Caucasians, with normal trichromatic vision, between 28 and 52 years old participated in the study. Their mean age was 36.3 and the standard deviation 10. Three of the subjects were classified as dark eyed (two

dark brown and one light brown) and three as light eyed (two blue and one green). The classification was done by simple iris observation in two groups -light eyes and dark eyes, and, though simple and naive, in healthy subjects is always consistent with the iris melanin amounts, with brown iris eyes exhibiting always much higher amounts of melanin than blue and especially green (Koblova et al., 2005). Since one of the main absorbers in the fundus is melanin, difference in melanin pigmentation amongst individuals must affect fundus diffusion (see chapter 2). As mentioned in the introduction, though the RPE melanin is relatively constant in the population, choroidal melanin varies significantly (Weiter et al., 1986). And since the iris and the choroid are both part of the same anatomical layer, the uvea, the iris color gives a rough estimate of the amounts of choroidal melanin.

Scattering of the subjects was measured to be within the normal range and similar between all subjects. The experiment followed the tenets of the Declaration of Helsinki. Informed consent was obtained from the subjects after they were fully informed about the nature of the measurements.

3.2 Spectral and spatial characterization of the fundus

For the optical characterization of the fundus a setup based on the double-pass principle was built. A schematic diagram of the double-pass setup for the optical measurements is depicted in fig. 3.1. It consisted of a xenon lamp (S) as light source and a liquid crystal spatial light modulator (LC2002; Holo-eye, Berlin-Adlershof, Germany) conjugate with the retina, which was used to produce uniform white discs. A selectable bandwidth tunable optical filter (LCWS; Meadowlark Optics, Inc., Frederick, CO) was used to select the two different wavelengths: 560nm (FWHM=45) and 650nm (FWHM=30). The image of each disc projected onto the retina was recorded after a double passage through the eye through a beamsplitter (BS), by an electron multiplying charge-coupled device camera (EMCCD Luca; Andor, Belfast, UK). The camera's response to light was taken into account based on a calibration performed in a separate experiment. The calibration of the camera can be found in appendix B.

The subject's head was stabilized at the appropriate position using a bite-bar and the alignment of the pupil was done using a commercial CMOS camera located conjugate to the pupil plane through a beam splitter (BS). Pupil alignment was done by achieving the sharpest pupil image at the CMOS pupil camera.

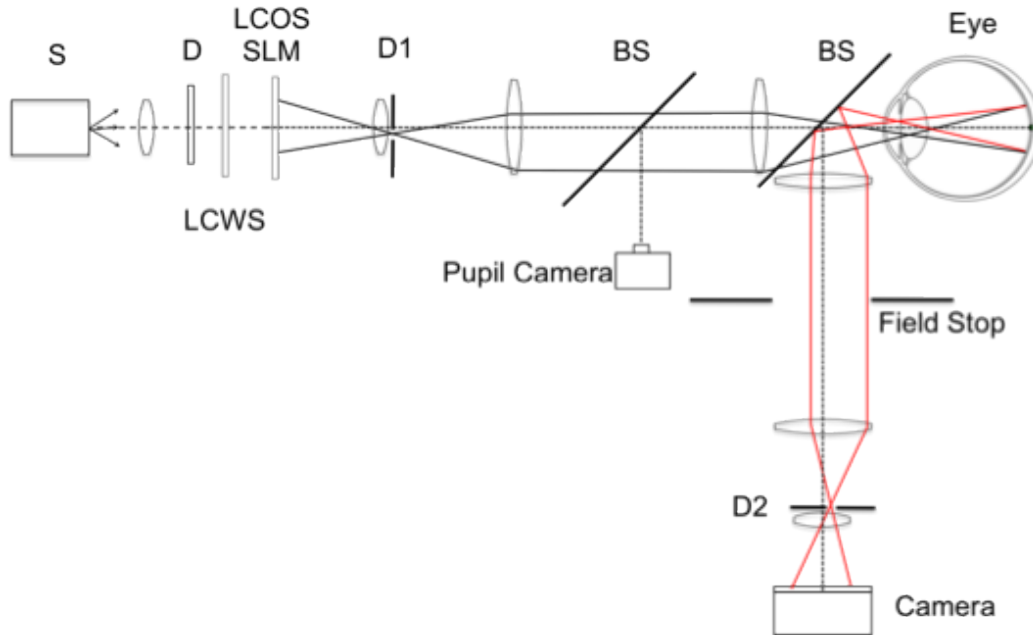


Figure 3.1: Schematic of the optical setup used for the measurement of the fundus reflectance.

Two circular diaphragms, D1 and D2, of diameter equal to 1.8 mm, both conjugated to the pupil plane, were displaced transversely to each other so that the upper part of the pupil was used for illumination (first pass, illumination pathway, black in fig. 3.1) and the lower part for imaging (second pass, imaging pathway, red in fig. 3.1). Using this trick we were able to eliminate the contamination due to back-scattered light from the cornea and the lens. In order to find the appropriate configurations for the diaphragms in the pupil plane, the optical setup with a model eye was simulated in Zemax. The minimum separation of the diaphragms depended on two things: the maximum field size and the characteristics of the eye. The parameters of and a schematic of the model eye along with the pupil configuration can be seen in table 3.1 and fig. 3.2 respectively.

The size of the diaphragms was chosen such that kept aberrations to a minimum. An artificial eye with a spectrally flat diffuse reflector with 99% reflectivity between 350 to 1500nm (SM05CP2C; Thorlabs Inc) acting as the retina was used for the calibration and all reflectance measurements were normalized with respect to that.

In the optical experiment a sequence of 40 uniform disks, from 0.18° to 7.28° radius, was projected onto the retina and the reflected light from the fundus was recorded by the EMCCD camera. The fixation point of the tar-

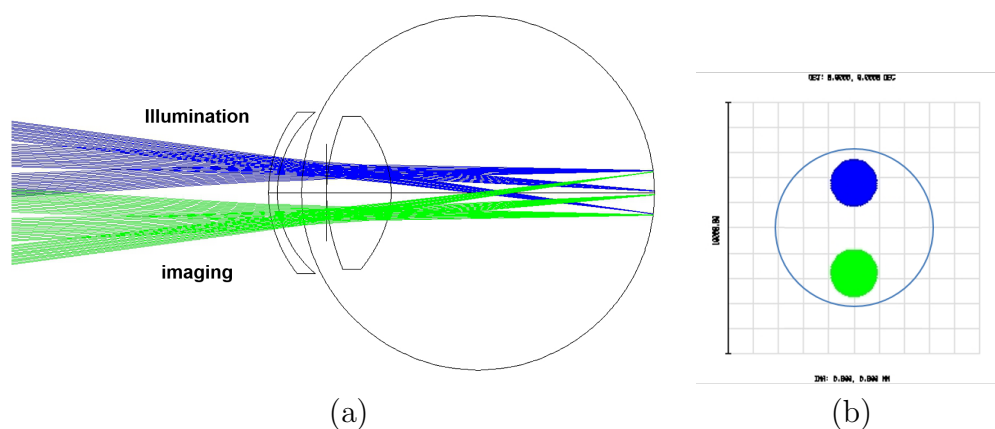


Figure 3.2: Aperture configuration at the pupil plane. The light enters through the top and is captured through the bottom.

Table 3.1: Optical and physical parameters of the eye used for the Zemax simulation.

Surface	Description	Position (mm)	Curvature	Conic	Refractive Index
1	Anterior Cornea	0	7.8	-0.5	1.377
2	Posterior Cornea	0.52	6.7	-0.3	1.377
3	Pupil	3.62	Inf	0	-
4	Anterior Lens	3.72	10	0	1.420
5	Posterior Lens	7.42	-6	-3.25	1.420
6	Retina	24	-11	0	-

get was at about 7° nasally, chosen such that no large retinal blood vessels appeared at or near the center of the disk, ensuring that the measured reflectance was that of the fundus and not affected by the presence of a high absorbing vessel, whose position may vary during the projection of the different size disks (see next chapter for examples). Dilation of the pupil was done using 1% tropicamide. Finally, the power of the source was measured at the corneal plane using a Newport 1815-C Power Meter (Newport Corporation, USA) and it was found to be between 0.4 and $0.6\mu\text{W}$, well below the acceptable limits put by ICNIRP (ICNIRP, 2013).

After each image was recorded, the center of each image was found and its intensity at the center of each projected disk was calculated by averaging

the central 3×3 pixel area, approximately 7 minutes of arc. The script used to determine the centroid of the disk can be found in appendix C. The total light available to the photoreceptors was calculated from the relation

$$I_p = I + rI. \quad (3.1)$$

where I is the intensity of the light passing from the photoreceptors before interaction with the deeper layers of the fundus and r is the measured relative reflectance for the specific wavelength and field size.

Previous studies with a similar optical setup (Ginis et al., 2012, 2013, 2014) have shown that under these illumination and imaging conditions fundus reflectance is not affected by photoreceptor bleaching. Furthermore, studies preliminary to the experiment had shown that the Stiles-Crawford effect, for the given geometry does not have an impact on the results.

Retinal reflectance depended on field size, wavelength and the subject's iris color. Figures 3.3(a) and 3.3(b) show reflected light as a function of field size for green and red light respectively for the two groups of subjects, where the scale is such that the intersubject differences are emphasized. The errors are the standard deviation from the mean. In fig. 3.4, both green and red data for the two different groups are plotted together.

As expected reflected light at 560nm is less than that at 650nm for both groups, with the red light showing a maximum reflectance of about 3 to 4 times more than the one of the green one. The dependence of the reflectance on the field size is, as expected, stronger for the long wavelength due to its weaker absorption and higher scattering in the RPE and the choroid (Hammer et al., 1995). Furthermore, although reflectance at red was higher for the subjects in the light colored iris group, this was not the case at green, since RPE melanin and choroid hemoglobin absorb most of the green light well before reaching the choroid, for choroidal melanin to play any significant role. It is important to mention once again, that iris color is only related to the amount of melanin in choroid, since the choroid and the iris comprise the same anatomical layer, the uvea, whereas RPE melanin seems to be independent of the iris color (Delori and Pflibsen, 1989; Weiter et al., 1985; Wakamatsu et al., 2008). There is a significant difference in spectral reflectivity in the longer wavelength between dark iris subjects and light iris ones, which shows the importance of choroidal melanin in the backscattered light.

The change in the available light to the photoreceptors for two different field sizes at two different wavelengths was calculated according to the

relation

$$R = \frac{\frac{I_{p,650}^{big}}{I_{p,560}^{big}}}{\frac{I_{p,650}^{small}}{I_{p,560}^{small}}}. \quad (3.2)$$

Substituting the intensities from (3.1) one gets

$$R = \frac{\frac{1+t_{650}^{big}}{1+t_{560}^{big}}}{\frac{1+r_{650}^{small}}{1+r_{560}^{small}}}. \quad (3.3)$$

The above ratio gives the increase of the red to green light available to the photoreceptors for a large field with respect to a smaller field. The above ratio for two field sizes that match the conditions investigated in the psychophysical setup (see below), namely 0.4 degrees and 6.5 degrees radius, was found to be 3.3% (SD=0.6) and 2.02% (SD=0.22) for light and dark eye subjects respectively. The standard deviation refers to the group's standard deviation. The individual's deviation between measurements was insignificant and was not taken into account.

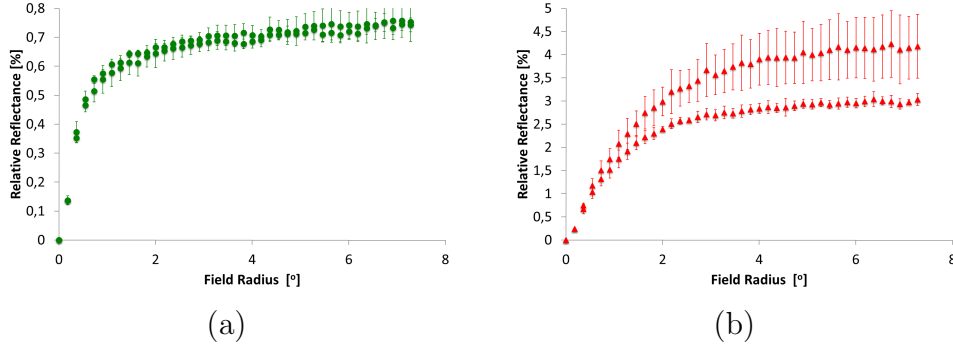


Figure 3.3: Fundus reflection at the center of the projected disk for the two different groups at 560nm (a) and at 650nm (b).

In the previous chapter (see chapter 2), where fundus diffusion was simulated and the back-scattered light was calculated for various disk sizes, the absorbance of the choroid was arbitrarily doubled in order to simulate the difference in melanin amongst the different subjects. Nevertheless, comparing fig. 2.8 to fig. 3.4 one can see that the behavior of the simulated data is very similar to the experimental ones, even for a relatively simple fundus model with only 4 layers. The simulations described in the previous chapter were carried out mainly to estimate the difference that one should anticipate for fundus diffusion at different wavelengths for subjects with different pigmentation. Surprisingly enough, the simulation results were quite accurate

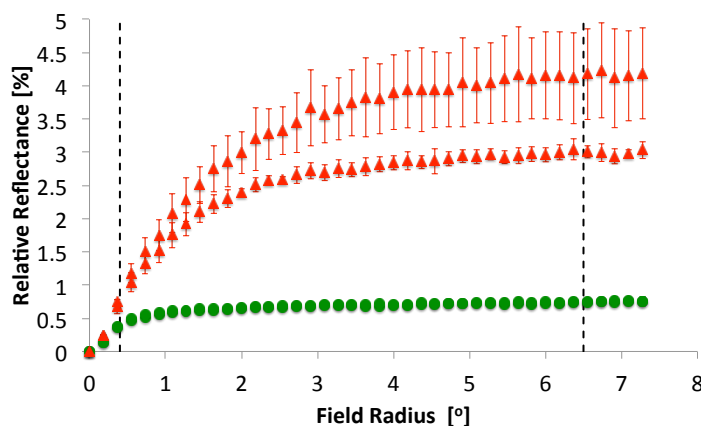


Figure 3.4: Fundus reflection for two different wavelengths and for two different subject groups with respect to field size. At 560nm (circles) the two groups are indistinguishable, whereas at 650nm (triangles) the light colored iris group exhibits a much higher relative reflection.

in predicting fundus diffusion, showing that it could be used in combination with experimental measurements to extract actual values for the pigmentation of an individual.

3.3 The effect of fundus diffusion in vision

The psychophysical method used for the study of fundus diffusion in vision was based on the Heterochromatic Flicker Photometry (HFP) which is proven to be consistent with the CIE standard observer (Wagner and Boynton, 1972). A schematic of the setup is shown in figure 3.5. The system consisted of a uniform source of 560nm and 650nm LEDs (S1) controlled by an Arduino micro-controller, a two-position adjustable aperture (D), a plano-convex lens (L), a pupil camera for subject alignment and a white flat-spectrum source which served as the adapting field, chosen such that it selectively isolates the M cone class, following previous studies (Sharpe et al., 2005; Stockman et al., 2008). The LED source operated in two channels in opposite phase at a frequency of 25Hz, changeable if needed at the start of the experiment. Red light intensity was kept fixed, whereas green light intensity was variable, controlled by the subject using a potentiometer connected to one of Arduino's analog input pins. The 16° adapting field was superimposed on the flickering field with an illuminance of 3 log photopic trolands. The total average illuminance of the test field and the adapting background was 3.2 log trolands. The test field consisted of a 0.4° radius disk surrounded by a dark

ring of less than 0.1° thickness, surrounded by a concentric annulus flickering in phase with the test field, as seen in figure 3.6. The aperture (D) could take two distinct values, thus blocking or allowing the view of the annulus. The radius of the entire disc, i.e. test field, dark ring and annulus was 6.5° .

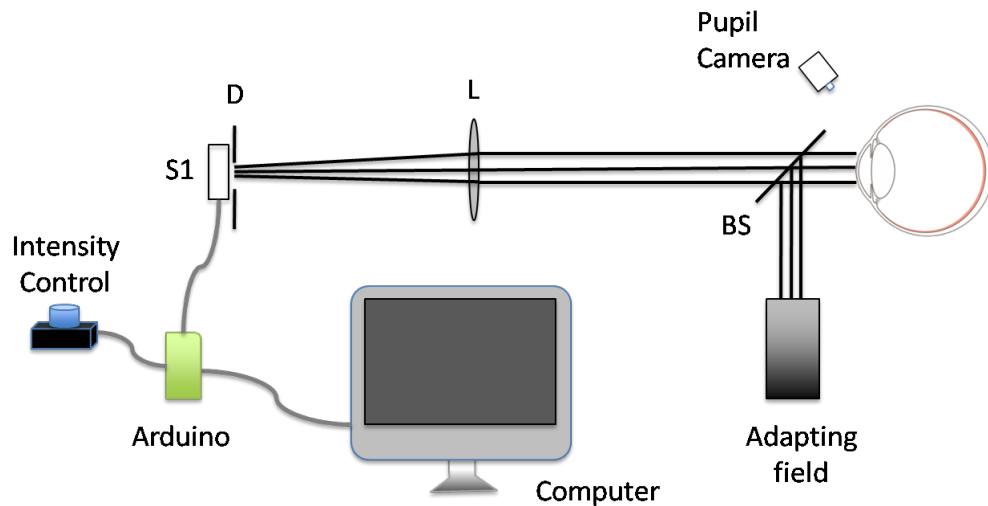


Figure 3.5: Schematic of the psychophysical setup used to measure relative color sensitivity.

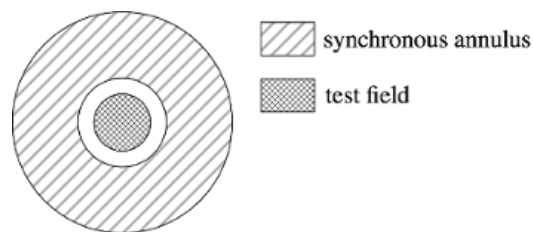


Figure 3.6: Schematic of the test field used in the psychophysical experiment.

The task of the subject in the psychophysical test was to determine the green light intensity where the flicker becomes minimal or, ideally, cancelled. The subject was asked to find the minimum flicker intensity which could be altered by a linear single turn potentiometer and the examiner registered the value. In order for the voltage and current at the LEDs to be fixed¹, the potentiometer was not used as a variable resistor in series with the LED, thus reducing the voltage to the LED, but it was connected to an Arduino's 8-bit analogue input. The input value was then used as output to dim the green

¹LEDs don't function linearly with voltage. There is a threshold voltage that turns the LED on, over which the current increases sharply with increasing voltage.

LED using Pulse Width Modulation (see appendix D). At the beginning of the session the subject was given a few minutes to get familiar with the objectives of the experiment and the control of the knob. This time also ensured the adaptation of the subject to the background field. The test was performed monocularly.

The procedure was repeated ten times for each condition, i.e. with the annulus present and without it. It is important to underline here that although the annular field was flickering in phase with the test field, the procedure is not equivalent to testing at a larger field size. The dark ring surrounding the test field provided a clear demarcation of the test field and the annulus. The subjects, all familiar with the procedure were instructed to judge flicker minimization or cancellation based on the modulation of the central test field solely, assuring this way that the area under investigation was always the same, i.e. only central foveal vision was used in both field sizes.

The respective relative green to red sensitivity increase for the two different experimental conditions, without and with the annulus, is given by the formula

$$R_s = \frac{S_{annulus}^{GR}}{S_{noannulus}^{GR}}. \quad (3.4)$$

and was calculated to be 7.2% (SD=2.6) and 3.4% (SD=1.24) for the light group and dark group respectively. All subjects demonstrated an increase of green to red relative sensitivity, ranging from 1.9 to 10.7%, with increasing field size as seen in table 3.2. Figure 3.7 shows green to red sensitivity without

Table 3.2: Mean green to red sensitivity and deviation for the two experimental conditions for all six subjects

Subject	G/R no annulus		G/R with annulus	
	Mean	Standard Deviation	Mean	Standard Deviation
G.P. (dark)	0.1045	0.0065	0.1065	0.0055
D.C.(dark)	0.111	0.0025	0.1165	0.0035
H.G.(dark)	0.1125	0.0015	0.1165	0.002
M.S.(light)	0.1165	0.0045	0.129	0.005
P.S.(light)	0.132	0.007	0.138	0.0035
P.A.(light)	0.1325	0.006	0.141	0.0045

the annulus with respect to green to red sensitivity with the annulus, for all subjects. Finally, figure 3.8 shows the relative sensitivities for the two groups and for the two different conditions.

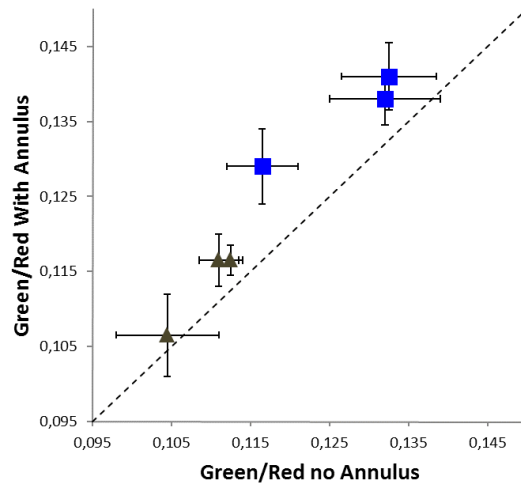


Figure 3.7: Relative green to red sensitivity without the annulus vs. relative green to red sensitivity with the annulus for all subjects. Subjects with dark iris are depicted with brown triangles and subjects with light iris with blue squares.

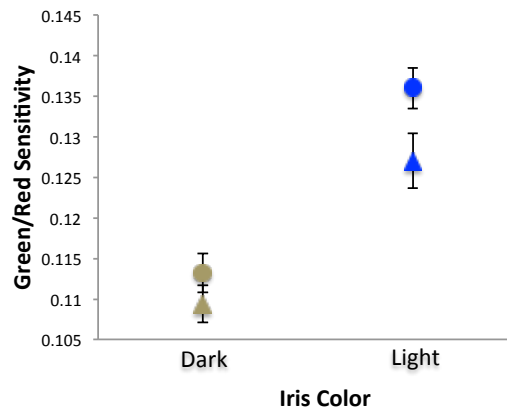


Figure 3.8: Relative green to red sensitivity for the two groups for the test field without the annulus (triangles) and with the annulus (circles).

3.4 Relation between fundus diffuse light and color sensitivity

The results of the two setups for the two different iris color groups are shown in table 3.3. The second column contains the relative sensitivity increase for the two different condition - with and without the annulus- and the third

one the relative increase in the ratio of the red to green reflectance for two different disk radii, matching those of the psychophysical test fields.

Table 3.3: Relative increase in the green to red sensitivity with and without the annulus (first column) and relative increase on the available light at the photoreceptors with field size for the two groups.

Group	Psychophysical (%)	Optical (%)
Dark	3.4(1.24)	2.02(0.22)
Light	7.2(2.6)	3.3(0.6)

Although it might seem counter-intuitive, in order to compare the corresponding quantities from the two experiments, in the ratio in the optical experiment as seen in eq. (3.3) the reflectance at red was divided by the reflectance at green, whereas in the psychophysical test the quantity under investigation is the green to red intensities ratio. This is due to the fact that more red light with respect to green light available optically leads to a lower green to red sensitivity i.e. higher value of the green to red intensities ratio. That in turn means that one must increase the intensity of the green light in the psychophysical experiment to compensate the optical increase of red light.

The qualitative comparison of the two different tests revealed two main points: there is an overall increase of the sensitivity due to diffuse light in the deeper fundus layers, which is consistent in all subjects, and this increase depends on the choroidal melanin of the subject, even for a simple classification by iris color. Therefore, there seems to be a contribution from the backscattered choroidal light to vision. Nevertheless, the effect can only be observed under appropriate laboratory conditions. Its small magnitude suggests that diffuse light from deeper fundus layers is unlikely to have practical relevance to vision.

The effect of the backscattering component on the photoreceptors was previously studied through the Stiles-Crawford effect by Berendschot et al. (2001). The study showed that the wavelength dependence of the SC effect is caused partially by the backscattered light and, therefore, the backscattered light is to some extent visible. The findings of our work are in line with this observation showing an increase of sensitivity with the amount of backscattered light.

Nevertheless, as shown in previous studies (van de Kraats et al., 1996; Prieto et al.), the impact of the backscattered light in vision is suppressed due to the directionality of the photoreceptors and the non-directionality of the backscattered light. This means that from the total light available at

the photoreceptors, only a fraction is guided from the outer segments of the photoreceptors and contribute to vision.

Regarding the psychophysical test, in principle it can be affected by three things:

- **The variability of L:M ratio between individuals.** The L:M cone ratio varies greatly between individuals, ranging from 0.4 to 13 according to Carroll et al. (2002) (or 1.1 to 16.5 for the sample studied by Hofer et al. (2005)) and has been shown to affect the individual sensitivity (Sharpe et al., 2005). Therefore, while deeper fundus layers absorb and scatter light depending on the choroid melanin, thus enabling us to naturally classify objects according to the melanin pigmentation, the visual effect could in principle depend also on the L:M ratio of the individual subject. In the experiment, the focus is on the change of the sensitivity between two distinct conditions (with an annulus surrounding the test field and without one), or the relative difference in the sensitivity ratios for the two conditions defined in (3.4). This effectively means that the results are normalized and thus, any difference in the L:M ratio between subjects, however great, would not affect the quantities under investigation. Furthermore, since the psychophysical test is done at the same site for both conditions, changes of the L:M ratio with eccentricity, if any, would not be an issue.
- **The change of the optical density of photopigments with eccentricity.** Previous studies have shown that the optical density of the outer segments of the photoreceptors changes with eccentricity, and more specifically it decreases for all types of cones when moving away from the fovea (Pokorny et al., 1976; Marcos et al., 1997; Yamada, 1969). This is believed to be a result of the change in length of the outer segments of the cones with eccentricity (Polyak, 1941). It has been shown that this change leads to a change in the width of the absorption spectrum throughout the retina that can effectively affect color vision (Stiles, 1937; Pokorny and Smith, 1976; Burns and Elsner, 1985; Alpern, 1979; Wyszecki and Stiles, 1980) and can also affect macular pigment density measurements using HFP (Sharpe et al., 1998). Nevertheless, this effect, also known as self-screening, did not affect the psychophysical test since for both conditions, with the annulus and without the annulus, since the same patch of foveal photoreceptors were used for the task.
- **The change of melanin density in the fovea.** As mentioned in chapter 1, melanin density is not uniform across the retina, showing a

peak at the fovea (Berendschot et al., 2010; Weiter et al., 1986). While the psychophysical task was performed foveally, the diffuse reflectance properties of the fundus were measured at about 7 degrees nasally. The reason for that was that optical measurements in the periphery have some important advantages; they are more stable as the subject can see better the fixation target and it is easier to avoid vessels. Moreover, specular reflections taking place at the ILM are significantly reduced at the periphery compared to the fovea.

Therefore the discordance between the psychophysical and the optical results can be attributed to the non-uniform distribution of melanin at the retina and/or the large errors in the psychophysical task associated mostly with the subjective nature of the test. Moreover, regarding the psychophysical test, it is worth noting that for the light colored iris subjects the variation between measurements was larger than the one for dark colored iris subjects, but the results were still consistently higher when the annulus was present.

On the other hand, the optical test has been proven to be very precise, showing a very high repeatability of the results. Therefore, direct comparison of the two experiments might be naive. However, and despite the quantitative discrepancies, a qualitative comparison of the results from the two experiments shows that the trend is the same, showing that the optically observed excess light can be detected up to a degree psychophysically and thus affect vision under certain conditions.

Chapter 4

Light Scattering Phenomena in Vision and Retinal Imaging

In this chapter a novel device to reconstruct the individual's wide-angle Point Spread Function (PSF) and a personalized technique to compensate for the effect of scattering in fundus imaging are described. The PSF reconstruction is based on the Optical Integration method in a double-pass system and the compensation was done through a custom contrast enhancement technique developed for that purpose.

As a proof of concept, before applying the method in-vivo, a single-pass test was performed. The complete algorithm for the PSF reconstruction and the contrast enhancement was tested for scattering caused by a photographic filter on a projected image. The advantage of the single-pass test is that since the original image is also available, it can be compared against the reconstructed. After the validation of the algorithm, it was applied in 7 healthy subjects.

Note that the term scattering, refers to scattering at the optics, whereas scattering in the fundus, as before, it is referred to as fundus diffusion.

4.1 Data Analysis and PSF approximation

4.1.1 The method of Optical Integration

The method of optical integration, is a technique developed by Ginis et al. (2012) for the reconstruction of the wide-angle PSF of the eye but it can also be applied for the evaluation of any optical system. The emphasis was given to the detailed reconstruction of the wide-angle part dominated by scattering rather than the central part of the PSF where aberrations and diffraction are

the main phenomena.

For the reconstruction of the PSF, the images of a series of uniform disks of increasing radius were recorded with a camera after going through the optics of the system, so that the recorded images are the convolution of the PSF with the original images. With this method, as will be shown rigorously below, the only experimental quantity needed for the reconstruction of the PSF is the intensity at the center of the projected disk.

The method can be applied for both single-pass and double-pass configurations with the latter being especially interesting since it is the case of the eye. In case of a single-pass system as in fig. 4.1(a), the PSF acting on the original image is the real PSF of the system, hereby called the single-pass PSF. In case of a double-pass system as in fig. 4.1(b), the PSF acting on the original image is the double-pass PSF, i.e. the autocorrelation of the real PSF of the system. For a symmetric PSFs autocorrelation is identical to selfconvolution (Easton, 2010) and therefore one can compute the PSF of the system using the double-pass PSF from the relation

$$PSF = \mathcal{F}^{-1} \left[\sqrt{|\mathcal{F}(PSF_{dp})|} \right] \quad (4.1)$$

where \mathcal{F} and \mathcal{F}^{-1} the forward and inverse Fourier transform respectively. It needs to be noted here that the above formula treats the Fourier transform of the PSF, or the Optical Transfer Function (OTF), as a real function. The proof of the flatness of phase of the OTF can be found in the introduction.

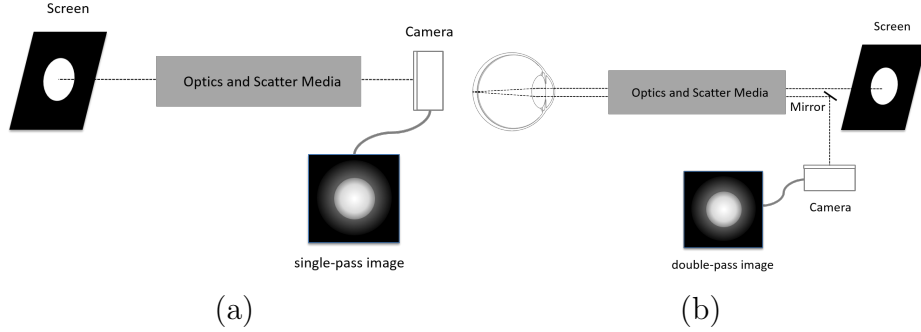


Figure 4.1: Single-pass (a) and double-pass configuration (b) for the projection of the uniform disks.

Assuming a rotationally symmetric PSF and that the image is a uniform disc of intensity I_o , then the intensity I at the center of the disc as recorded by the camera, thus after the effect of the system's PSF, will be given by the formula

$$I_c(\theta) = I_o \int_0^\theta 2\pi\phi PSF(\phi) d\phi \quad (4.2)$$

where θ the radius of the disc in degrees of visual angle, and PSF the total PSF of the system, which in case of a double-pass system is the correlation of the single-pass -the actual PSF of the system- with itself.

Eq.(4.2) essentially says that the intensity at the center is described by the surface integral of the PSF within a disc of radius θ . Here it is assumed that the PSF integrates to unity at $\pi/2$

$$\int_0^{\pi/2} 2\pi\theta PSF(\theta)d\theta = 1 \quad (4.3)$$

Assuming $I_o = I(\pi/2)$, eq. (4.2) can then be rewritten as

$$I_c(\theta) = I\left(\frac{\pi}{2}\right) \int_0^\theta 2\pi\phi PSF(\phi)d\phi \quad (4.4)$$

$$I'_c(\theta) = \int_0^\theta 2\pi\phi PSF(\phi)d\phi \quad (4.5)$$

where $I'_c(\theta)$ is the normalized intensity. In practice, it is fair to assume that $I(8) \approx I(90)$, or that almost all the energy of the PSF is within those first 8 degrees or less, meaning that the vast contribution to the PSF comes from angles between 0 to about 8 degrees. For our experiment, the intensities were normalized by dividing each intensity with the intensity at the center of the largest recorded disk. The PSF can be expressed with respect to the normalized intensity at the center as follows

$$PSF(\theta) = \frac{1}{2\pi\theta} \frac{dI_c(\theta)}{d\theta} \quad (4.6)$$

The above relation is the key relation for the computation of the PSF in the optical integration method and effectively states that the PSF can be extracted solely from the intensity at the center of the projected disks.

4.1.2 PSF reconstruction strategies

Difference Quotient

The most obvious and straightforward way to approximate the PSF would be by taking the difference quotient

$$PSF(\theta) = \frac{1}{2\pi\theta_n} \frac{I_c(\theta_{i+1}) - I_c(\theta_i)}{\theta_{i+1} - \theta_i} \quad (4.7)$$

where $\theta_n = (\theta_{i+1} - \theta_i)/2$. Nevertheless, for experimental data, this has been proven to be noise dependent and can give a bad estimation of the PSF. Such an example is shown in fig. 4.2. Common sources of noise can be thermal noise (dark current) at the camera and slight changes at fundus reflectance due to fixational eye movements.

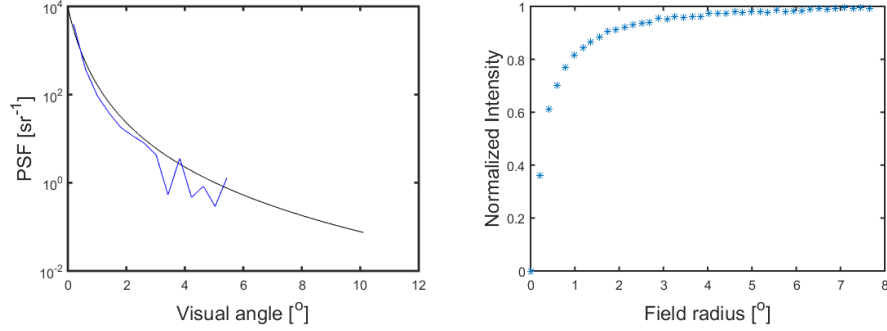


Figure 4.2: Example of a noisy PSF reconstruction (left) using the method of finite differences (blue line), where the real PSF is depicted in black and the normalized intensities used for the reconstruction (right).

PSF bi-parametric model fit

Another approach, would be to assume a function for the PSF based on existing models for PSF. A good candidate would be

$$PSF(\theta) = \frac{A}{(\theta + \theta_0)^n} \quad (4.8)$$

which is a generalized expression for the Stiles-Holladay formula (Holladay, 1926; Stiles, 1929) with n being approximately 2, θ_0 a very small parameter to avoid the pole when $\theta = 0$ and A a normalization factor. It needs to be taken into account however, that the model doesn't describe adequately the narrow angle part of the PSF Van den Berg et al. (2010), where the low order and high order aberrations are dominant.

As mentioned before (eq. (4.3)), the PSF normalizes to unity at $\theta = \pi/2$. Plugging eq. (4.8) into eq. (4.3) and solving for A we get

$$A = \begin{cases} \frac{1}{2\pi} \frac{1}{\left[\frac{\pi}{2} + \theta_0 \ln(\theta_0) - \theta_0 \ln\left(\frac{\pi}{2} + \theta_0\right)\right]} & \text{if } n = 1 \\ \frac{1}{-2\pi} \frac{1}{\left[\ln(\theta_0) + \ln\left(\frac{\pi}{2} + \theta_0\right) - \frac{2\theta_0}{\pi + 2\theta_0} + 1\right]} & \text{if } n = 2 \\ \frac{1}{2\pi} \frac{(n-1)(n-2)}{\theta_0^{2-n} + (\frac{\pi}{2} + \theta_0)^{(1-n)} \left(\theta_0 - \frac{\pi}{2} + \frac{n\pi}{2}\right)} & \text{if } n \neq 1 \wedge n \neq 2 \end{cases}, \theta > 0 \quad (4.9)$$

Finally, substituting equation eq. (4.8) into eq. (4.5) and solving the integral one gets an expression for the normalized intensity for the given PSF model

$$I_c(\theta) = \begin{cases} 2\pi A [\theta - \theta_0 \ln(\theta_0 + \theta)] & \text{if } n = 1 \\ 2\pi A \left[\ln(\theta_0 + \theta) + \frac{\theta_0}{\theta_0 + \theta} \right] & \text{if } n = 2 \\ -\frac{2\pi A (\theta_0 + \theta)^{1-n} (\theta_0 - \theta + n\theta)}{(n-1)(n-2)} & \text{if } n \neq 1 \wedge n \neq 2 \end{cases}, \theta > 0 \quad (4.10)$$

where the normalization factor, A , is given in eq. (4.9). The above formula has two free parameters: n and θ_0 . The dependence of the PSF on those two parameters is shown in fig. 4.3 below. As seen in fig. 4.3(b), a decrease in the parameter n , for a fixed θ_0 , leads to a different PSF curve, with higher values at higher angles. On the contrary, the PSF increases at higher angles when parameter θ_0 increases, as seen in fig. 4.3(d). Moreover, as expected from eq. (4.6), the slopes for the respective intensities curves behave similarly.

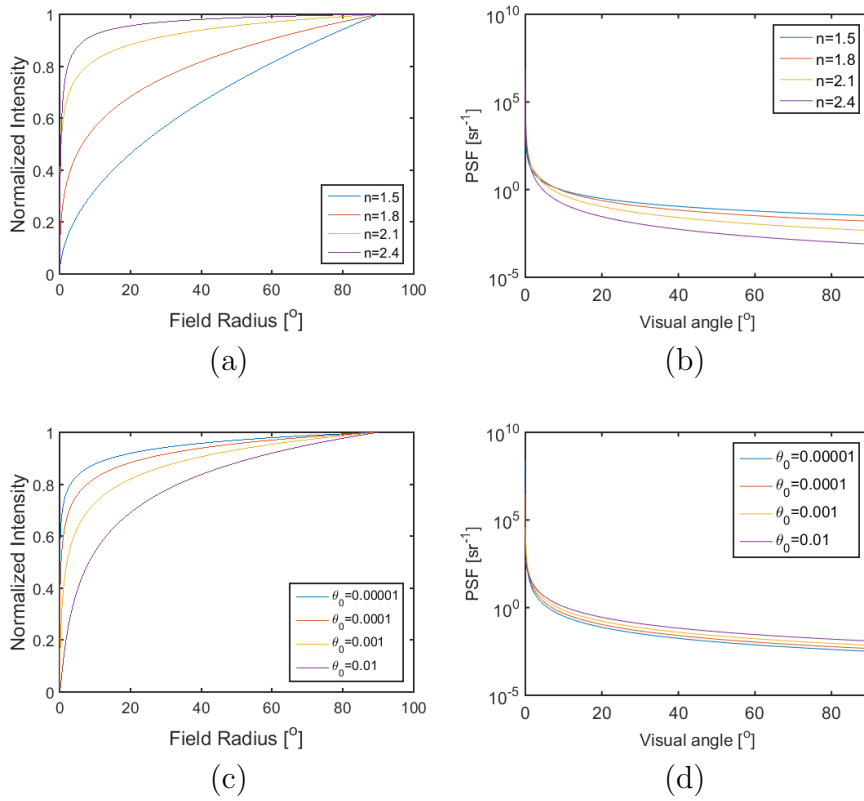


Figure 4.3: Dependence of the Intensity curve and the PSF by the parameters of the model, n (top) and θ_0 (bottom).

For the calculation of the parameters MATLAB's `fminsearch` function can be used, based on the unconstrained nonlinear optimization algorithm (Lagarias et al., 1998). The function finds the minimum of a multi-parametric function, starting at an initial estimate for the parameters. The disadvantage of this fitting is that it needs a relatively large number of points for an accurate estimation of the parameters.

Glare function fit

In the case of the human eye, a even more specific PSF model could be used, such as the one proposed by Van den Berg et al. (2010) (see chapter 1 for details). The general PSF model suggested reads

$$\begin{aligned}
 PSF_{CIE} = & [1 - (0.08 (A/70)^4)] \\
 & \left[\frac{9.2 \times 10^6}{[1 + (\theta/0.0046)^2]^{1.5}} + \frac{1.5 \times 10^5}{[1 + (\theta/0.045)^2]^{1.5}} \right] \\
 & [1 + 1.6(A/70)^4] \left\{ \left[\frac{400}{1 + (\theta/0.1)^2} + 3 \times 10^{-8} \times \theta^2 \right] \right. \\
 & \left. + p \left[\frac{1300}{[1 + (\theta/0.1)^2]^{1.5}} + \frac{0.8}{[1 + (\theta/0.1)^2]^{0.5}} \right] \right\} \\
 & + 2.5 \times 10^{-3} \times p [sr^{-1}]
 \end{aligned} \tag{4.11}$$

where θ the angle in degrees, A the age and p a pigmentation coefficient taking values 0, 0.5 and 1 for black, brown and light eyes respectively. The age was the free parameter to be determined by the fitting to the experimental data and the pigmentation p was set by simple observation of the subject's iris.

The strategy followed for the reconstruction of the single-pass PSF from double-pass measurements was the following: firstly, the glare PSF was calculated for a set of ages and for the three different pigmentation levels. Each PSF was associated with a scatter parameter S at 3 degrees. Then, the double-pass PSF was computed by taking the selfconvolution¹ of the single-pass PSF.

$$PSF_{dp} = \mathcal{F}^{-1} \{ \mathcal{F}\{PSF_{sp}\} \cdot \mathcal{F}\{PSF_{sp}\} \} \tag{4.12}$$

For the given set of double-pass PSFs, the intensities at the center of disks of radius θ were computed according eq. (4.2). The radii were chosen such that they were the same as the ones measured in the experiment. The simulation was done in MATLAB with a code snippet that simulates the intensities seen at appendix C.1. The simulated data produced by the code snippet can be seen in fig. 4.4.

Once the simulated intensities were produced, the fitting of the real data to the simulated ones is straightforward, simply by finding the minimum root-mean-square deviation (RMSD) from the simulated intensities sets. The

¹Remember: selfconvolution and autocorrelation are identical since the PSF for scattering is rotational symmetric.

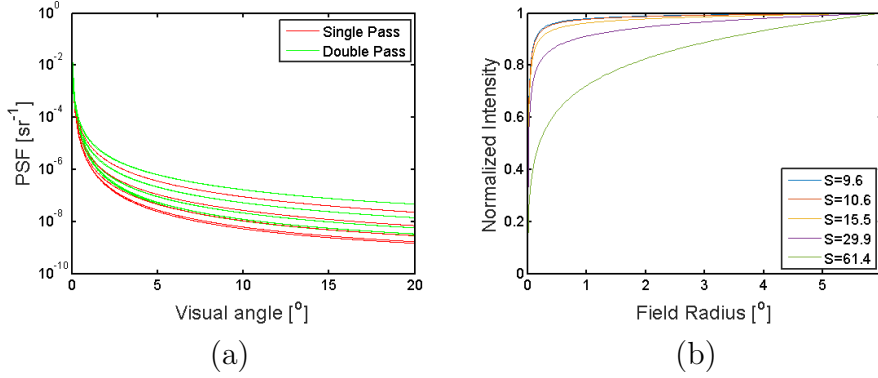


Figure 4.4: (a) Single-pass (red) and double-pass (blue) glare function for a set of ages for fixed pigmentation. (b). Double-pass normalized intensities with the corresponding single-pass scatter parameter for fixed pigmentation.

RMSD is defined as

$$R(A) = \sqrt{\frac{\sum_{\theta} (I_{exp}(\theta) - I_{sim}(\theta, A))^2}{n_{\theta}}} \quad (4.13)$$

where I_{exp} and I_{sim} the experimental and simulated intensity respectively and n_{θ} the total number of intensity data points (disk sizes). An example of such a fit is shown in figure 4.5, where three different glare PSF curves can be seen, with the blue one being the one with the lowest RMSD value, and therefore the best fit. In this particular example the RMSD values were 0.0263, 0.0132 and 0.0332 from top to bottom.

It needs to be noted here that for the fit using the glare function, only data points above 2.5 degrees were used. There were two reasons for that: firstly, the focus of the experiment was the wide-angle part of the PSF and less the part below 1 degrees where aberrations and diffraction are dominant. If the narrow angle part was the objective, one would need to project more disks below 2 degrees to have a higher sampling at lower angles where the shape of the PSF changes drastically. Secondly, as mentioned in chapter 2, scattering in the ocular media becomes dominant at larger angles. For angles below about 3 degrees fundus diffused light vastly affects the measured intensity at the center, with a very strong dependence on the wavelength. Nevertheless, as shown in chapter 3, the effect is not visually easily detectable but it is optically clearly present. The glare function was, however, based largely on psychophysical data and therefore light diffusion in the deeper fundus layers contributed only weakly to the measured PSF. Therefore, it was assumed that the glare function is a better fit for the data for angles where fundus diffusion is no longer present and scattering in the media is the dominant

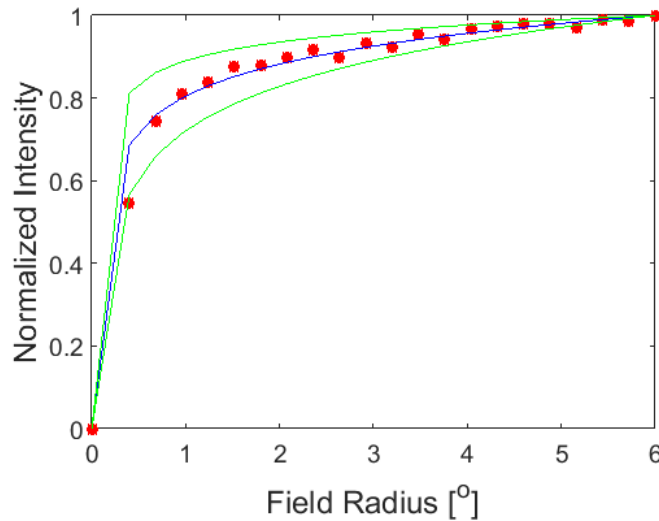


Figure 4.5: An example of a fit using the glare function.

effect.

Another important point is that the intensity data go from about 0.3 degrees radius and usually up to less than 8 degrees. For low amounts of scattering, the intensity at the center at that 8 degrees, has reached its maximum value. However, for higher amounts of scattering this is not the case, and therefore normalizing the data with the maximum value would not be correct. To take that into account, the glare function simulations were normalized at the same angle with the real data, in this case the maximum projected disk.

Linear Fit

A simpler and less noisy method, similar to the Difference Quotient method, to reconstruct the PSF at a specific angle would be to perform a linear fit on a small region of intensities around a specific angle and use the slope to approximate the derivative, thus the PSF at this specific angle. The PSF can then be approximated by the relation

$$PSF(\theta) = \frac{slope|_{\theta}}{2\pi\theta} \quad (4.14)$$

This technique, though simple, can provide a good estimate of scatter at a specific angle. A similar method is used for the extraction of the scatter parameter in the Sigma apparatus (Ginis et al., 2014). Nevertheless, the method is more appropriate for the approximation of a single PSF value at

a given angle (and from there the scattering parameter) and not the entire PSF.

4.1.3 Two-dimensional PSF reconstruction

As mentioned before, for scatter phenomena, it is safe to assume that the PSF possesses azimuthal symmetry. Under that assumption, the two-dimensional PSF is constructed by simply rotating the one-dimensional PSF in space. Naturally, since the general function describing the PSF is known, the 2D PSF can be reconstructed to the desired accuracy by choosing the appropriate number of points. There are two important aspects that one needs to take into account in order to correctly reconstruct the PSF: the point density and the parity of the number of points.

In order to have an accurate reconstruction of the PSF, one would ideally need a very high sampling. This, however, is not always practical and it is limited by the computational power. As an example, given that on an average workstation a 2048 by 2048 PSF takes about 5 seconds, the reconstruction of the two dimensional PSF of 10^6 by 10^6 points would take about 15 days. Therefore, a clever choice of sampling is needed, in order for the simulated PSF to be a good approximation of the continuous one but within a reasonable time.

Another important aspect of the simulation that one might underestimate, is the parity of the number of points in the sampling of the PSF. The parity becomes more important when the sampling is relatively low. This is due to the fact that the PSF, for angles around 0, changes dramatically, with its peak being two or more log units higher than the neighbor point, for a reasonable number of points, as seen in fig. 4.6(a), where the PSF was sampled from 0 to 12 degrees by 1023 and 1024 points. As expected, the profiles of the two PSFs are almost identical except for the very first points close to 0 degrees, where the odd sampled PSF is almost 2 log units higher. What, at a PSF level, might seem trivial, has an immense effect at the MTF, as seen in fig. 4.6(b).

In case where the number of points is sufficiently large, the parity of the sampling becomes less important, but still the MTF is better approximated using an odd number of points. In fig. 4.7 an odd (blue) and an even (red) sampled MTF is shown for a very high sampling number for the PSF² where the parity becomes irrelevant in the MTF approximation.

Finally, although MATLAB can perform the Fast Fourier Transform

²For practical reasons, the number of points stayed the same, but the PSF's range was reduce to 2 degrees.

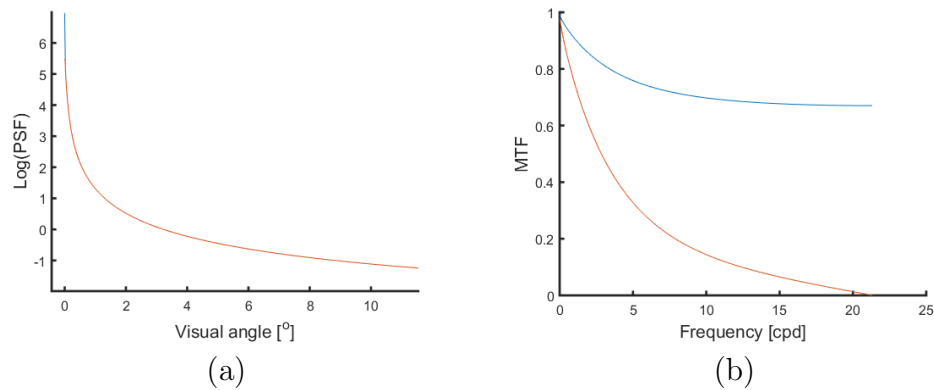


Figure 4.6: PSF (a) and MTF (b) reconstruction for 1023 (blue) and 1024 (red) points.

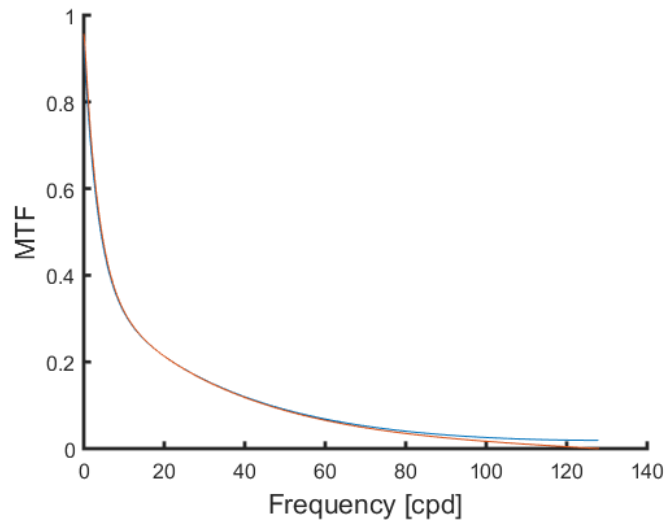


Figure 4.7: MTF reconstruction for odd (blue) and even (red) points, for high density sampling.

(FFT) for matrices or vectors of any size, it is more efficient if the sample number is a power of 2³.

4.1.4 Image Enhancement

The single-pass 2D wide-angle PSF describes fully the eye and it is the only quantity needed in order to compensate the effect of scattering in fundus imaging.

The captured fundus image (or in the vision scenario the seen image) is

³although for a modern computer the effect is barely noticeable

the convolution of the original image with the PSF of the system or else the product of the Fourier transform of the image with the Fourier transform of the PSF. Naturally, deconvolution is simply the division of the image with the PSF in the Fourier domain or simply

$$Image_{orig} = \mathcal{F}^{-1} \left\{ \frac{\mathcal{F}\{Image\}}{\mathcal{F}\{PSF\}} \right\} \quad (4.15)$$

The deconvolution technique for the extraction of the original image can be fast, but is limited by noise amplification, coming mainly from the division in the Fourier space, where small variations in the Fourier space can lead to high noise. Moreover, discontinuities in the Fourier transform can contribute to the ringing of the image. An example of ringing after deconvolution can be seen in fig. 4.8



Figure 4.8: Ringing in picture after performing a deconvolution.

Noise can be avoided by sampling down the image, or else lowering its resolution. This would be equivalent to the convolution of the image with a Gaussian filter

$$G(x, y) = \frac{1}{2\pi\sigma^2} e^{-\frac{x^2+y^2}{2\sigma^2}} \quad (4.16)$$

Ringing on the other hand is avoided by taking into account the diffraction taking place at the pupil. The diffraction MTF can act as a natural filter, filtering out very high frequencies where our PSF is not accurate⁴. In other

⁴The high spatial frequencies is affected solely by the very central part of the PSF.

words, we exclude the very high frequencies where diffraction is the dominant effect. The original image can now be extracted from the relation

$$Image_{orig} = \mathcal{F}^{-1} \left\{ \mathcal{F} \{Image\} \frac{\mathcal{F} \{PSF_{diff}\}}{\mathcal{F} \{PSF_{scat}\}} \right\} \quad (4.17)$$

The diffraction limited MTF is the autocorrelation of the pupil function. In the special case of a square pupil the MTF is given by the relation

$$MTF_{diff} = 1 - \frac{f}{f_{cut}} \quad (4.18)$$

where the cutoff frequency is defined as $f_{cut} = \frac{1}{\lambda(F|\#)}$ and $F|\#$ for the finite conjugate case is defined as

$$(F|\#)_{objectspace} = p/D \quad (4.19)$$

$$(F|\#)_{imagespace} = q/D \quad (4.20)$$

where p and q the object and image distance respectively. For more details see Boreman and Boremann (2001).

The scattering and the diffraction limited from a square aperture MTFs are shown in fig. 4.9

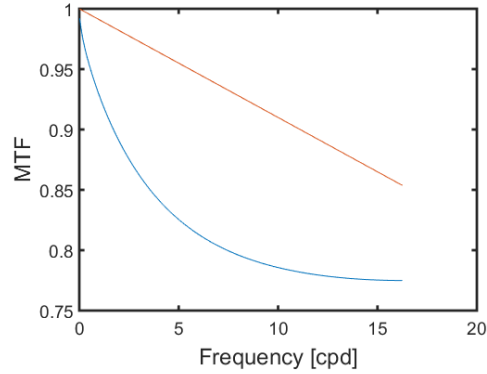


Figure 4.9: Diffraction limited MTF for a square aperture (red) and scattering MTF (green).

4.2 A single-pass test

The first step in order to validate the optical integration and the image enhancement method, was to setup a single-pass system where scattering

was introduced with a photographic filter. The PSF was then reconstructed with the method of optical integration and then images with and without the scattering filter were captured. The image enhancing method was applied to the latter and it was compared to the original image.

4.2.1 Experimental Setup

Figure 4.10 shows the setup used for the reconstruction of the PSF. The setup consists of an electron multiplying charge-coupled device camera (EMCCD, Luca; Andor, Belfast, UK) conjugate through a telescope to a projector screen, as seen in the schematic. The effect of scattering is induced by a filter (Pro Mist; The Tiffen Company, NY), representing the eye's lens, conjugate to an aperture (D1). The system, is essentially part of the double-pass system, which will be presented in detail in the next section. The projector

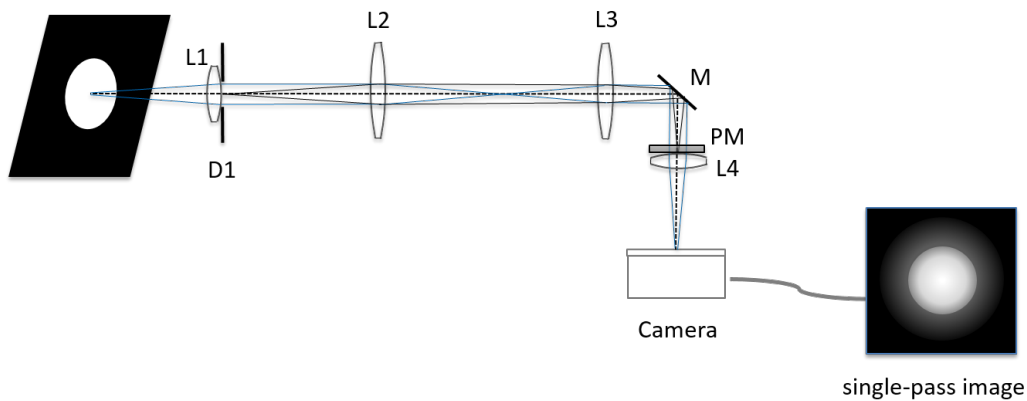


Figure 4.10: Experimental setup for the single-pass reconstruction of the PSF. L1, L2, L3 and L4 lenses, D1 aperture, M half mirror and PM (Pro Mist) a scattering media, simulating scattering in the eye.

used to project the image was an Optoma PK201 pico projector with a native resolution of 854×480 .

Graphical User Interface

A Graphical User Interface (GUI) was developed in MATLAB for the application of the optical integration method and the acquisition of images for the single-pass system. The GUI offered three different modes of operation, the single-pass mode, the capture image mode and the video mode.

- In single-pass mode, the user can show a number of uniform discs and record their image at the EMCCD camera, after passing through the

optics of the system. The software then calculated the intensity at the center of each of the shown discs and presented a plot showing the disc size in degrees of visual angle vs. the intensity at the center.

- In capture mode, the user could load any image, show it on the projector and record the image, after it went through the optics of the system.
- In video mode, the user could see a real time image of the projector as seen at the EMCCD camera. This was used as a control option, to fine tune the focus of the system and properly adjust exposure levels.

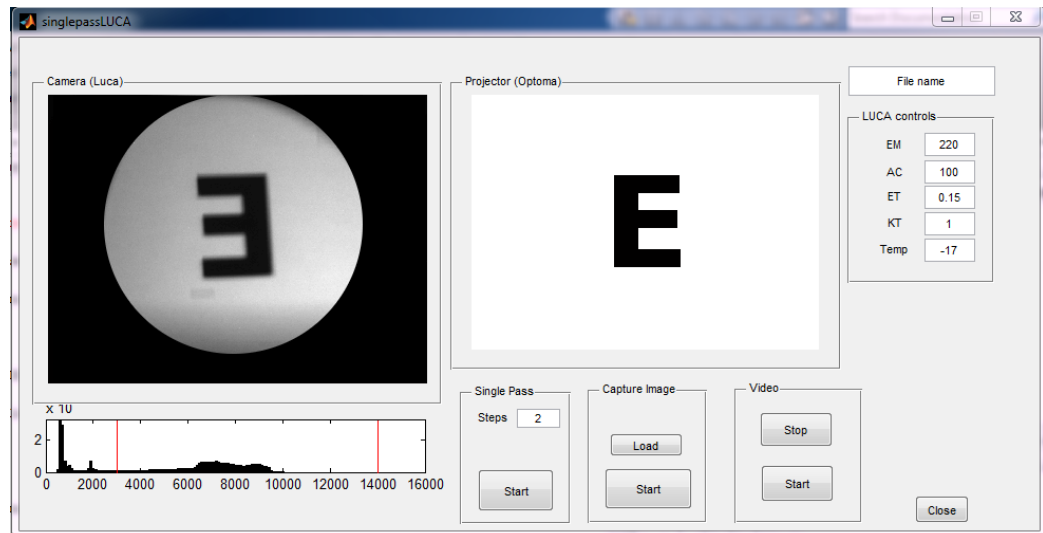


Figure 4.11: Graphical User Interface (GUI) developed in MATLAB for the control of the setup.

The software also gave the user full control of the camera's 4 main parameters: Gain (EM), Accumulated Cycles (AC), Exposure Time (ET) and Kinetic Series (KT).

- Gain referred to the electron-multiplying gain of the camera and could take values between 0 (off) and 220 depending on the light conditions.
- Exposure time was the time in seconds during which the CCD sensor was ON, collecting light.
- Accumulated Cycles was the number of single scans done.

- Kinetic Series mode captures a sequence of single scans, or a sequence of accumulated scans, into memory. This mode is equivalent to manually taking a series of single scans (or accumulated scans). However, by using the built-in Kinetic Series mode one gains the ability to specify the time delay between two consecutive scans and also the total number of scans to be acquired.

An example illustration of the parameters can be seen in fig. 4.12.

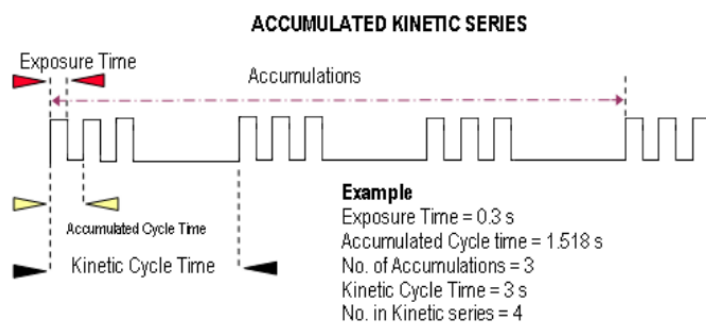


Figure 4.12: An schematic explaining the acquisition parameters of the camera. The horizontal axis represents time.

The EMCCD camera was calibrated in order to give a linear intensity response. The calibration process is described in detail in appendix B.

The temperature of the CCD is shown in the GUI window, labelled as Temp. In order to reduce the camera's dark current, it is important to correctly monitor and control its temperature, assuring that it stays low and constant throughout the measurement. A temperature between -20 and -30 degrees Celsius is considered adequate, as per the manufacturer's specifications.

Finally, a histogram of the recorded image was presented during image acquisition that allowed the user to monitor the pixel intensities. This way the user could ensure that, on the one hand, there were no saturated pixels and, on the other hand, the pixels of interested had the highest possible value.

4.2.2 PSF approximation of the scatter filter

The optical integration algorithm was applied for the reconstruction of the profile of the PSF of a scatter filter (Pro Mist 1; The Tiffen Company, NY), using the setup shown in fig. 4.10 on page 79, where the glare function from

eq. (4.11) was used to model the PSF, as described in chapter 4.1.2. Preliminary tests done with the other reconstruction techniques yielded similar results. The reconstructed profile of the filter's PSF is shown in fig. 4.13.

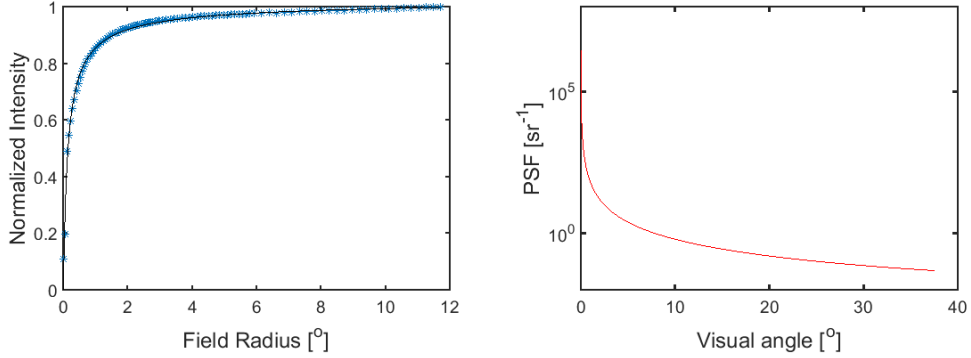


Figure 4.13: Intensities at the center for different disk radii (left) and PSF profile (right) of Pro Mist 1, reconstructed with the method of optical integration.

After reconstructing the 1-dimensional profile of the PSF, assuming rotational symmetry, one can easily reconstruct the 2-dimensional PSF with the method described in section 4.1.3. The image of the logarithm of the 2-dimensional PSF of the filter Pro Mist 1 is shown in fig. 4.14. The filter



Figure 4.14: Reconstructed 2d PSF for filter Pro Mist 1.

was found to have a straylight parameter $\log(S) = 1.68$.

4.2.3 Image enhancement

Three components are needed for the reconstruction of the scatter-free image: the wide-angle PSF, the diffraction limited PSF and the captured image. The

2D-MTF for the diffraction limited PSF was created according to eq. (4.18) with a simple MATLAB code snippet which can be found in appendix C.2. Having all parts, the original image can now be reconstructed according to the image enhancement algorithm. The method was applied for three different images, seen in fig. 4.15(a)-fig. 4.15(i). The first image was chosen because it contains various spatial frequencies and a relatively high dynamic range, similar to a fundus image. The other two images were selected such that it show the effect of scattering on a simple visual test. Since the effect of

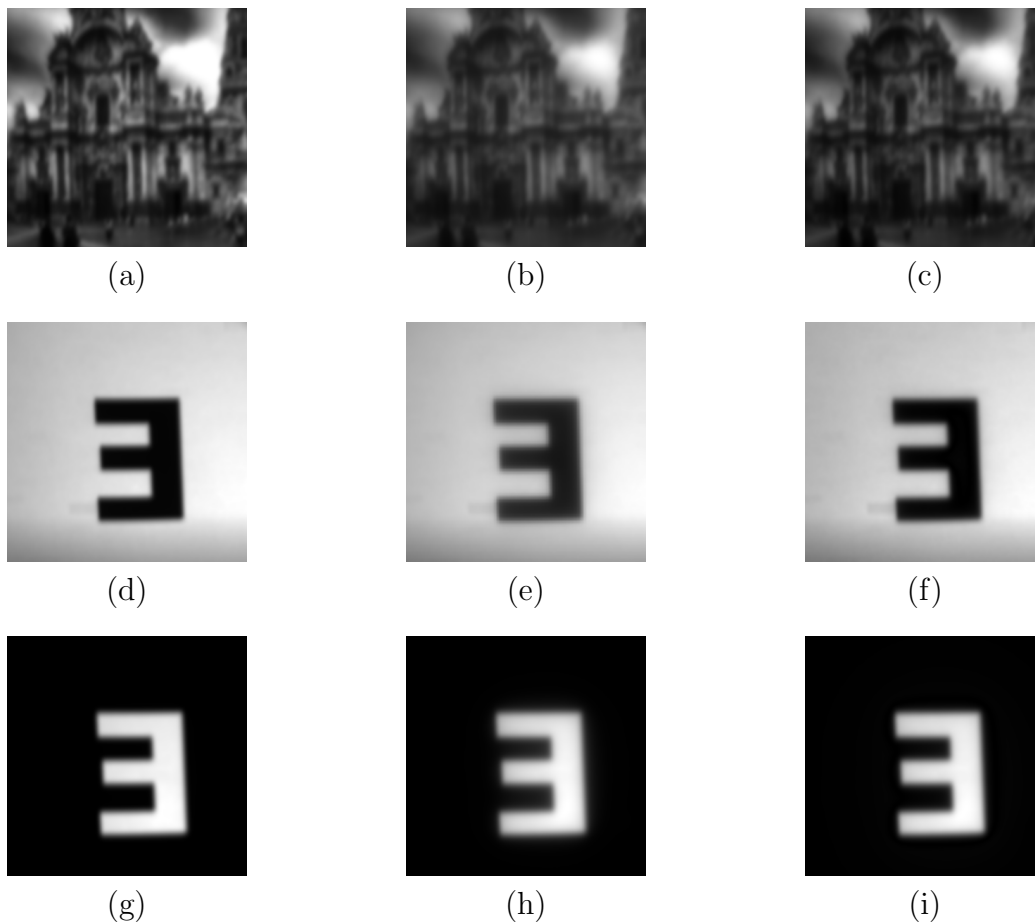


Figure 4.15: (a),(d),(g) Original images. (b),(e),(h) Captured images through Pro Mist 1. (c),(f),(i) Reconstructed images

contrast enhancement is not always visible in a printed image, a profile of each image both before and after the application of the algorithm is calculated and the two profiles are plotted together in fig. 4.16 for the image of the Cathedral and in fig. 4.17(a) and fig. 4.17(b) for the letter E for the two different backgrounds. In the image of the Cathedral, although the

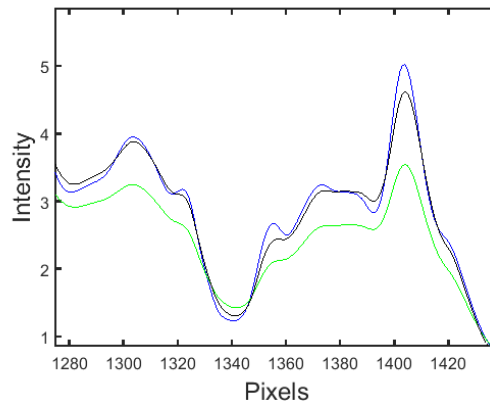


Figure 4.16: Profile of the original (blue), reconstructed (black) and “scattered” (green) image of the cathedral from fig. 4.15.

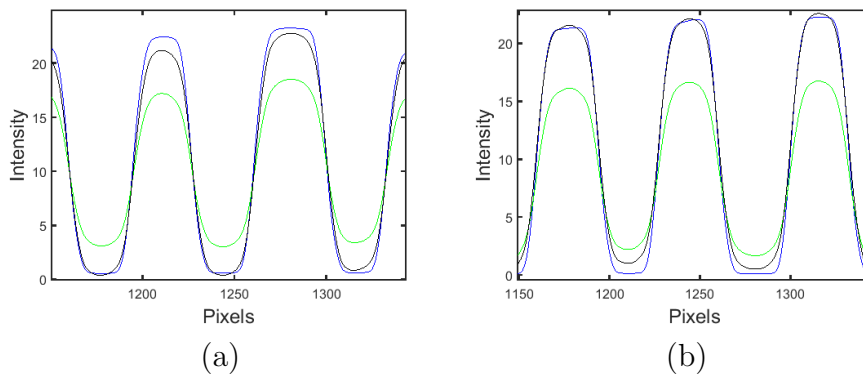


Figure 4.17: Profile of the original (blue), reconstructed (black) and “scattered” (green) image, for letter E, black on white background (a) and white on black background (b) from fig. 4.15.

contrast enhancement effect might not be visible in the actual image, in the image profile in fig. 4.16 the contrast retrieval is more clear. The blue and the black line depicting the original and the reconstructed image respectively differ only slightly, whereas the scattered image, depicted in green, shows a much lower contrast.

In the letter images where the contrast of the original image is high the effect is much clearer. It can be seen in fig. 4.15 that the filter lowers significantly the contrast of the image and smoothens the edges of the letter and the algorithm retrieves the original contrast. In the case of the black letter on the white background, the white background acts as a glare source, with light from the background reaching the black letter and reducing this way the image contrast. On the contrary, in the case of the white letter on the

black background, it is the light from the letter that is spread over the black background, thus lowering the intensity of the letter and increasing that of the background. Despite the fact that in the latter image the area of the letter was comparable to the area of the background, the effect of scattering on the letter was still higher for black letter on white background than the other way round. More specifically, the Michelson contrast for the black letter was as expected 1, whereas in the case of the white letter it was 0.96. In both cases the scattering compensation gives the correct contrast for the initial image, proving thus the validity of the optical integration and of the image enhancement technique.

One could reasonably argue however, on the importance of the a priori knowledge of the PSF and the effectiveness of the above method over a blind contrast enhancement algorithm. It needs to be emphasized here that the algorithm's objective is not to produce a better contrast image that might highlight structures and details of the fundus but to reconstruct the original contrast of the image. Although a blind enhancement might produce aesthetically better images, and might be a very useful tool for a qualitative analysis of the fundus, the resulting image would not represent correctly the intensity map of the original one. This means that a knowledge of the PSF is sine qua non for the contrast reconstruction of the original image.

4.3 Double-pass image acquisition and simultaneous PSF retrieval

Having proved the validity of the method of optical integration and the correct reconstruction of the contrast of the original image, the same concept was implemented to retrieve the eye's wide-angle PSF and then reconstruct fundus images by compensating for the effect of scattering in fundus imaging.

4.3.1 Experimental setup and procedure

The concept of the experimental setup used is based on the double-pass system described in chapter 3. Figure 4.18 shows a schematic representation of the instrument. It was designed to use the minimal amount of optical elements, minimizing this way the intrinsic scattering of the system (and the cost and size). Moreover, its geometry was such that it minimized the spurious light reflections from the instrument itself and the eye to be measured. A xenon lamp illuminates a wavelength filter, mounted on a filter wheel, followed by a diffusing fiber (Thorlabs Inc), a collimating lens (L5) and a motorized iris diaphragm (8MID10-40; Standa Ltd, Vilnius, Lithuania) which

is used to create uniform disks. The light is then guided through the optics of the system and focused on the subject's retina. The light reflected from the ocular fundus (depicted in fig. 4.18 in light blue) after passing through the optics of the system is reflected through a half mirror and collected by an electron multiplying charge-coupled device camera (EMCCD, Luca; Andor, Belfast, UK). The camera was mounted on a translating stage and was able to move axially, in order to compensate for the subject's defocus and the chromatic defocus. As before, the camera was calibrated and the full calibration is described in appendix B. A mechanical shutter (SH05 Optical Beam Shutter; Thorlabs Inc) controlled by a micro-controller (Arduino UNO, Arduino.cc, Italy) was synchronized with the EMCCD so that the duration of the illumination would be roughly the same with the duration of the image capture⁵. The actual system is depicted in fig. 4.19.

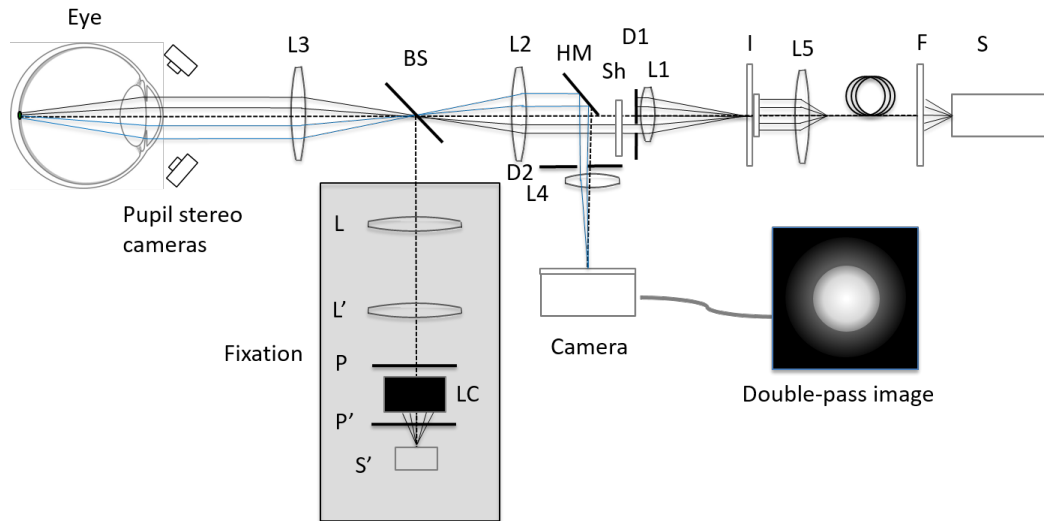


Figure 4.18: Experimental setup for the double-pass measurements. S, xenon lamp, F, wavelength filter, I, motorized iris with diffuser, D1 and D2 rectangular diaphragms conjugate to the pupil, Sh, mechanical shutter, HM, half mirror and BS, beam splitter. In light gray, the fixation subsystem with LC the LCoS and P, P' linear polarizers.

In order to be able to measure without the need of pupil dilation, we had to limit the illumination duration below 0.3 seconds. Two rectangular apertures, D1 and D2, 2 by 5 millimetres each, conjugates to the pupil plane were used.

The illumination aperture was conjugate to the upper part of the pupil whereas the imaging aperture was conjugate to the lower part of the pupil,

⁵In reality, the duration of illumination was set to be slightly longer, so that the camera captured a full image, with no dark tails.

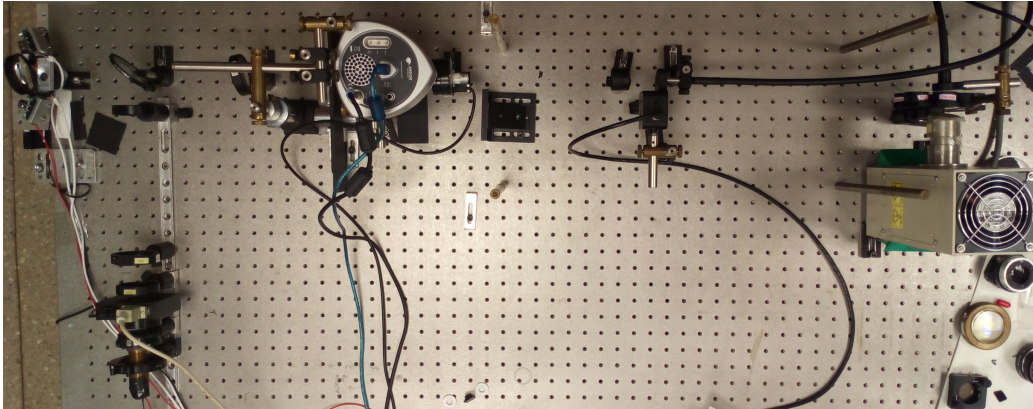


Figure 4.19: A photo of the system. The subject's position is at the top left.

eliminating thus any backscattered light from the lens or the cornea. The separation between the two apertures was such that no light was lost from an average dark adapted pupil, either in the illumination path or the imaging path. As in chapter 3, the size and the formation of the pupils was calculated according to a Zemax simulation of the system with a model eye. The properties of the model eye were based on the Navarro model eye and can be seen in table 3.1 in 56. The aperture configuration at the pupil plane, as computed by ray tracing in Zemax can be seen in fig. 4.20. As in the case of the system of the previous chapter, the ideal configuration was determined depending on the size of the maximum field and the physical and optical parameters of the simulated eye. Moreover, the rectangular shape of the apertures permitted higher amount of light to reach the fundus, with the same lateral aperture separation.

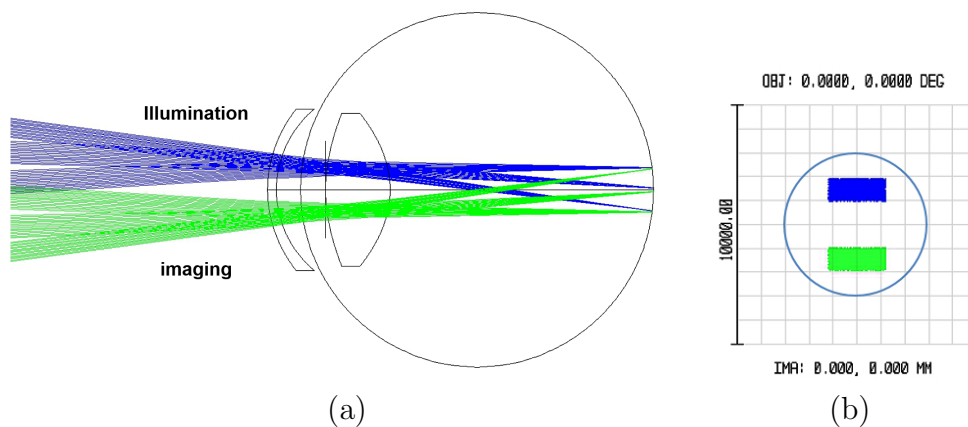


Figure 4.20: Aperture configuration at the pupil plane. The light enters from the top and is captured through the bottom.

For the fixation of the subject a Liquid Crystal Spatial Light Modulator was used (LC2002, Holoeye) in intensity mode. The LC was back-illuminated by a white LED (S') connected to the Arduino and it was located at a plane conjugate to the retina plane through the relay telescope formed by L and L3. Two polarisers, P and P', were also used along with the LC2000. In order not to contaminate the measurements with the fixation light coming from the white LED, Arduino was instructed to shut down the fixation LED temporarily, for as long as the measurement took place. The subsystem used for the fixation is shown in fig. 4.21(a).

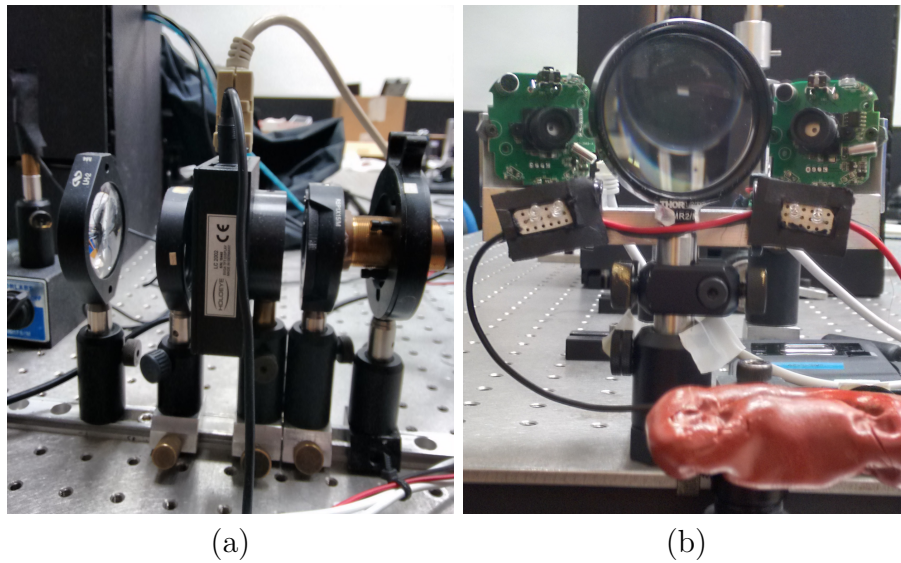


Figure 4.21: Photo of the fixation subsystem, where the led source, the two polarizers, a lens and the LC2000 can be seen (a) and photo of the 2-camera stereoscopic subsystem for high precision pupil alignment (b)

In order to find the ideal position of the pupil, the configuration of the apertures on the pupil plane was printed on a plain white paper, with the appropriate de-magnification caused by the relay telescope. The position of the pupil was then found at the best focus of the rectangular aperture D1 on the pupil plane. In reality, due to chromatic aberrations in the system, the conjugate plane to D1 was closer for shorter wavelengths. For this purpose the best focus for 4 wavelengths, namely 450nm, 550nm, 632 nm and 800nm⁶ was determined. Similarly, for the fine tuning of the imaging arm of the system, the same paper was back illuminated and the camera aperture (D1), conjugate to the pupil plane, was put at the point of best focus.

⁶At 632nm and 800nm the focus was practically the same

This illumination/recording approach requires a precise alignment of the eye, down to less than a millimeter. The importance of the precise alignment, especially in the longitudinal axis can be seen at fig. 4.20(a), where a slight longitudinal shift can cause a contamination to the image from lens back-reflections. Precise alignment was accomplished using a stereo sub-system which consisted of two cameras and NIR LEDs for illumination. The principle of operation of the aligning system was similar to that of the coincidence rangefinder, often find in photography or for military purposes for the precise determination of a distance. The geometry and an image of the stereo-sub system can be seen in fig. 4.18 and fig. 4.21(b) respectively.

The idea behind the stereoscopic alignment of the pupil is to focus two different cameras at the desired point, i.e. the pupil. The two cameras, seeing the pupil from an angle, would see it as an ellipse instead of a disk. The images from the two cameras are stretched accordingly in order to restore the pupil's circular shape as if the cameras were viewing the pupil from a hypothetical zero-degree angle. The alignment is correct when the images from both cameras are identical.

In order to compare the frames taken from the two different cameras a composite video of the pupil is shown in real-time where the upper half of the shown video is that of the left camera and the bottom part that of the right camera. When the pupil is shown at the center of the image without any discontinuities between the top part and the bottom part, then the pupil is properly aligned. An example of the pupil alignment process is shown in fig. 4.22.

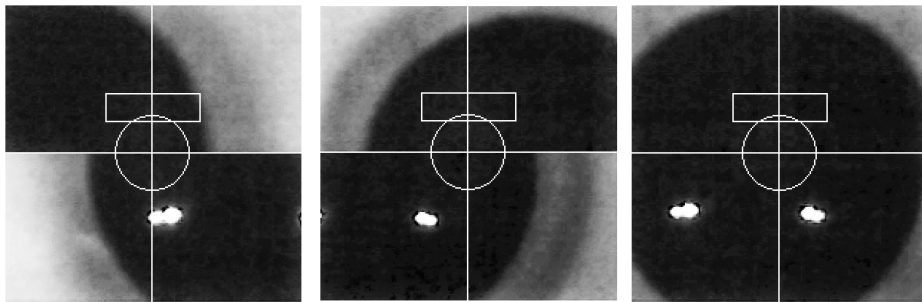


Figure 4.22: Pupil alignment using 2-camera the stereoscopic subsystem.

It needs to be noted here that despite the fact that both cameras were aligned so that they view the exact same area, in practice this is not trivial. In order to make sure that the viewing area was the same, the cameras were calibrated in a way such that a specific region of interest –the pupil– was chosen. For the calibration process an image of an 8mm circular pupil was located to the position of best focus for each wavelength and it was selected

as the region of interest for both cameras. The process is seen in fig. 4.23, where the left camera is being calibrated. The angle of the camera, as seen in the pictures, is not important, as long as the entire pupil is within the view of the camera.

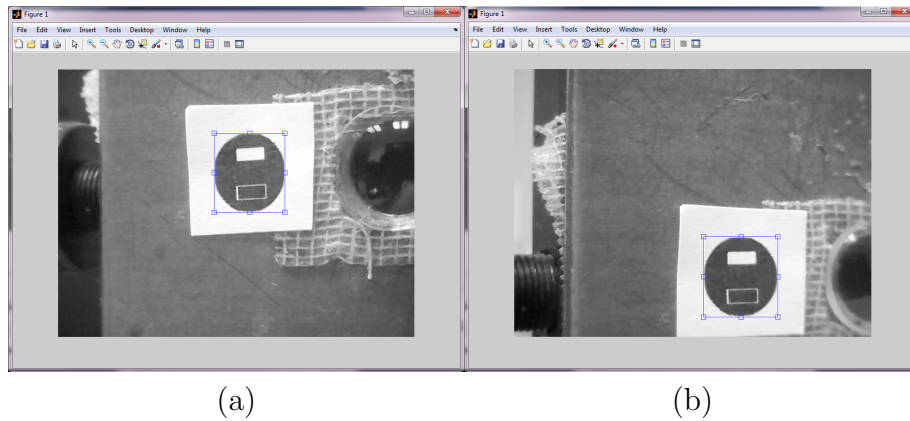


Figure 4.23: Calibration process for the 2-camera stereoscopic system, where the Region of Interest (ROI) is selected for each camera.

The Arduino micro-controller was used for the control of the mechanical shutter. The shutter controller (TSC001, Thorlabs INC) was externally triggered by Arduino with a 3.3 volts digital pulse. Additionally, the micro-controller was used to turn off the IR illumination used by the two cameras stereoscopic system during the fundus measurement in order to avoid unwanted light collected by the EMCCD camera.

All measurements were normalized with the reflectance values of a 99% flat spectrum reflecting surface used as a fundus in an artificial eye with similar geometry to a typical eye.

Graphical User Interface

The complete control of the setup was done through a Graphical User Interface (GUI) developed in MATLAB. A layout of the interface is shown in fig. 4.24 The interface could function in three different modes: Sequential, Single and Repeat mode.

- In sequential mode the user could take a series of fundus images with the option of whether to realign the pupil between measurements. For natural pupil measurements the monitoring of the pupil between images was absolutely essential in order to ensure that the pupil returned to its natural dark-adapted diameter.

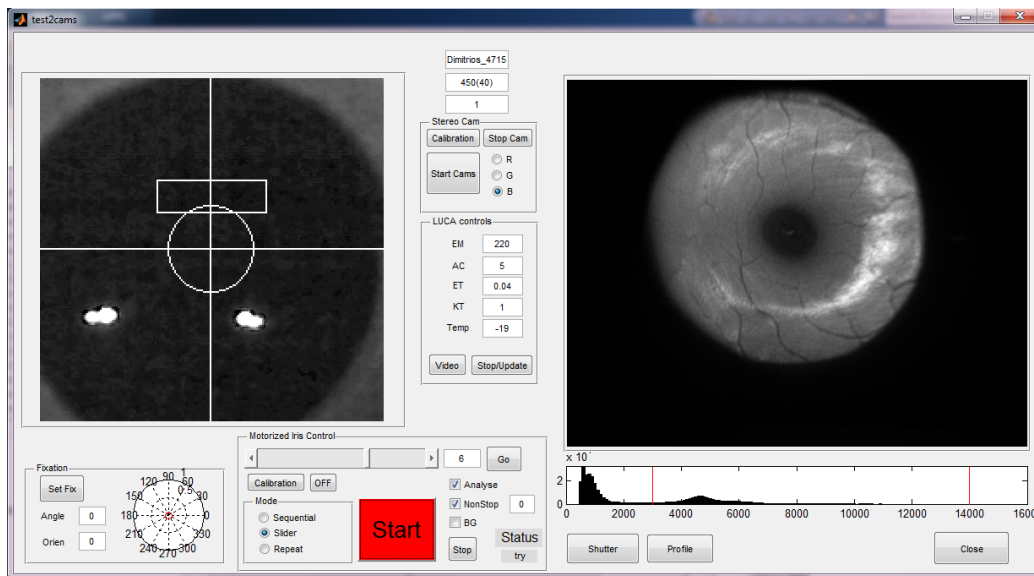


Figure 4.24: Graphical User Interface (GUI) developed in Matlab for the control of the setup.

- In single mode the user could take a single image. If the KT was greater than 1 then each image in the series was spatially transformed to the coordinate system of the first so that they were all identical.
- In repeat mode the user could select the settings for a series of single image captures. This was used in order to study the bleaching effect throughout the experiment.

For all modes the user could choose the parameters of the acquisition, namely the exposure time, the gain, the accumulated cycles and the Kinect time series. For a more detailed description of the parameters and their meaning see section 4.2.1.

4.3.2 Image registration

In general, there are two main techniques for the registration of the images in medical physics, both extensively used: the feature-based image registration and the intensity-based image registration (Aladl et al., 2011).

In feature-based techniques the user needs to find a landmark in the images which will be segmented from the images in order to perform the image registration. Therefore, feature-based image registration, though effective and fast, usually requires manual segmentation, making the procedure very difficult to automate (Aladl et al., 2011).

Intensity-based techniques on the other hand are based on the maximization of a similarity metric of the intensity values of the two images (Wells et al., 1996). Since there is no need of manually selecting a feature, the procedure can be fully automated and any possible errors coming from the segmentation process are eliminated, making the procedure more robust. Nevertheless, it requires much more actual computation power for the registration to be done and in some cases depending on the image parameters can be extremely slow. Here, due to the low resolution of the fundus images and their very characteristic vessel map ⁷, the intensity-based image registration was by far the fastest and easiest technique. Additionally, due to the large number of images taken, an automated method was essential in order to minimize the processing time.

The image registration was done according to MATLAB's intrinsic function for intensity based registration. There were two important parameters that need to be set and that could greatly affect registration's both speed and effectiveness; the similarity metric and the optimizer. The heart of the registration, the similarity metric, as its name suggests, is simply a scalar denoting how accurate the registration was, whereas the optimizer is the method used for the maximization or the minimization of the similarity metric. Each of the above quantities depends on a set of parameters such as the growth factor, the initial radius, the number of maximum iterations for the optimizer and the number of spatial samples. Finally, one needs to guess the possible distortion and provide a possible transformation between the two images. MATLAB's `imregister` can take a number of possible transformations as arguments combining the four main transformations: translation, rotation, scaling and shear. The most general transform used here was the affine transform, which despite being slower, covered all of the basic distortions such as rotation, scaling, translation and shear, caused by fixational eye movements and/or head movements while the subject was on the bite bar.

A registration example is shown in fig. 4.25 where two images taken at the same wavelength for the same subject with a few seconds difference were displaced with respect to one another due to fixational eye movements. In the first row the initial images are shown and in the second row the superposition of the two images is displayed before (c) and after (d) image registration. Discoloration demarks the differences between the two images. The improvement due to the registration process is obvious, especially at the central part of the image, which is the main area of interest.

⁷The vessel map has similar contrast at short and medium wavelengths. This will be proven useful for image registration in the following chapter.

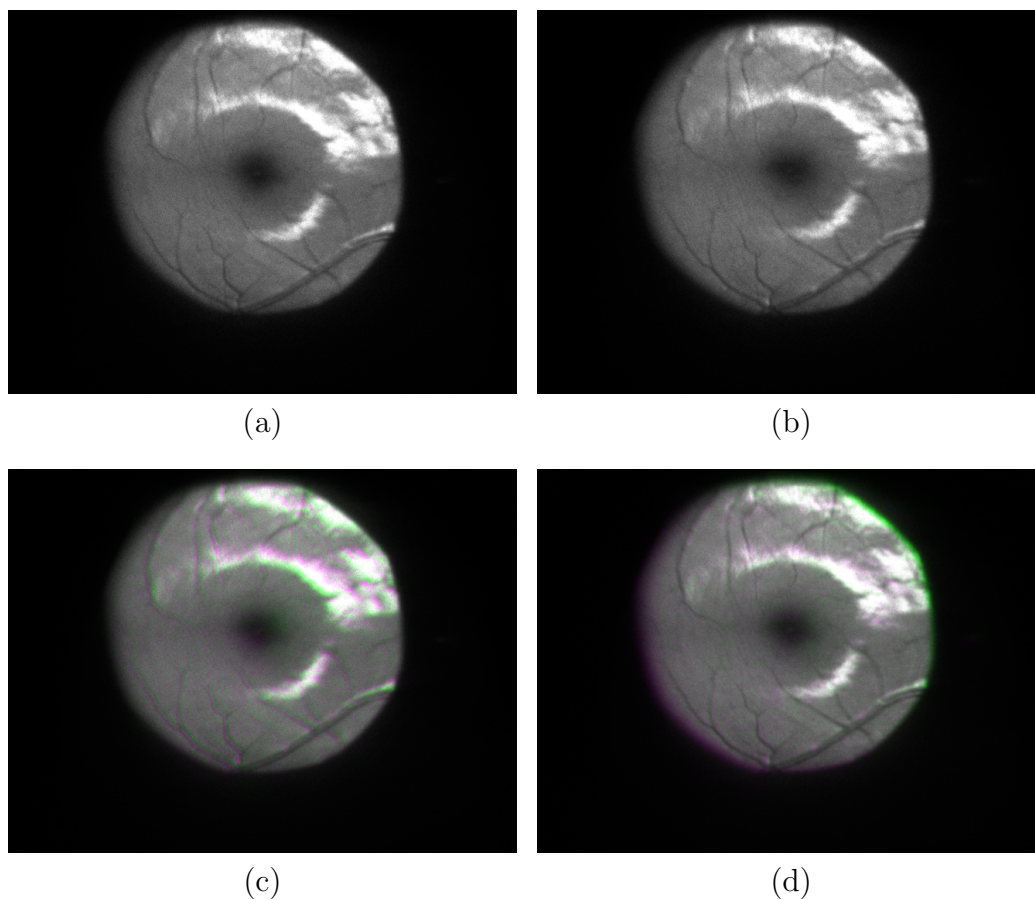


Figure 4.25: Two misaligned images of the fovea at 450nm due to fixational eye movements(a),(b), the superimposed image of the two original images (c) , and the superimposed image of the two images after image registration (d). In blue and green the relative image displacement.

4.3.3 Subjects

Seven subjects, all Caucasians, with normal trichromatic vision, between 24 and 35 years old participated in the study. Their mean age was 29.14 with a standard deviation 4.22. The experiment followed the tenets of the Declaration of Helsinki. Informed consent was obtained from the subjects after they were fully informed about the nature of the measurements.

4.3.4 Reconstruction of the wide-angle PSF

The first step was to properly align the subject, making sure that no light is blocked by the pupil neither in the way in nor in the way out. The appropriate wavelength was selected through a filter wheel, with 5 different wavelengths,

shown in table 4.1. Then the subject fixated at about 8 degrees nasally, where the fundus is more uniform, with fewer veins and no macular pigment. The subject was then instructed to fixate at various positions around that angle, a 7 degrees radius disk was projected on the retina and its image was then recorded. This was done in order to find a position where a central patch of about 2 degrees diameter is vein-free. The exposure time for the capture was adjusted in order to avoid pixel saturation and to assure that the recorded pixel values lie within the linear region of the camera response but high enough for a higher signal to noise ratio.

Table 4.1: Optical characteristics of the bandpass filters.

Filter	Central Wavelength (nm)	FWHM (nm)
FB450-40	450±8	40±8
FB550-40	550±8	40±8
FB632.8-10	632.8±2	10±2
FB800-10	800±2	10±2

Once a uniform area of the retina is located, the axial position of the camera is changed and more 7 degrees disks fundus images are taken in order to get the best focus of the retina on the camera, compensating this way any defocus caused by the subject's refractive errors and chromatic defocus. Since the motorized iris I (see fig. 4.18) does not move in the same manner with the camera, this could cause a defocus in the illumination path, making the limits of the disk being out of focus, however, this does not affect the measurement. In fig. 4.26 four image examples are shown, depicting a good image (a), an image very close to a vein (b) a partially saturated image (c) and an out of focus image (d). In our example, the conditions and parameters that will be used throughout the experiment for the given wavelength, are set to those used in (a).

After the ideal position of the retina and the camera is found, a sequence of 21 disks is projected on the retina, varying equally from 0.4 to 6 degrees radius, and their image is captured by the camera. An example of such a series is shown in fig. 4.27, with 9 projected disks.

During the previous two steps, a minimum number of 10 fundus images had to been taken. The procedure also assured the adaptation of the photoreceptors before starting the measurements. This was also tested in some preliminary tests where a number of disks of the same radius was projected on the retina⁸ over a period of 10 minutes and the intensity of a small patch

⁸The repeat mode in the GUI was used to test bleaching.

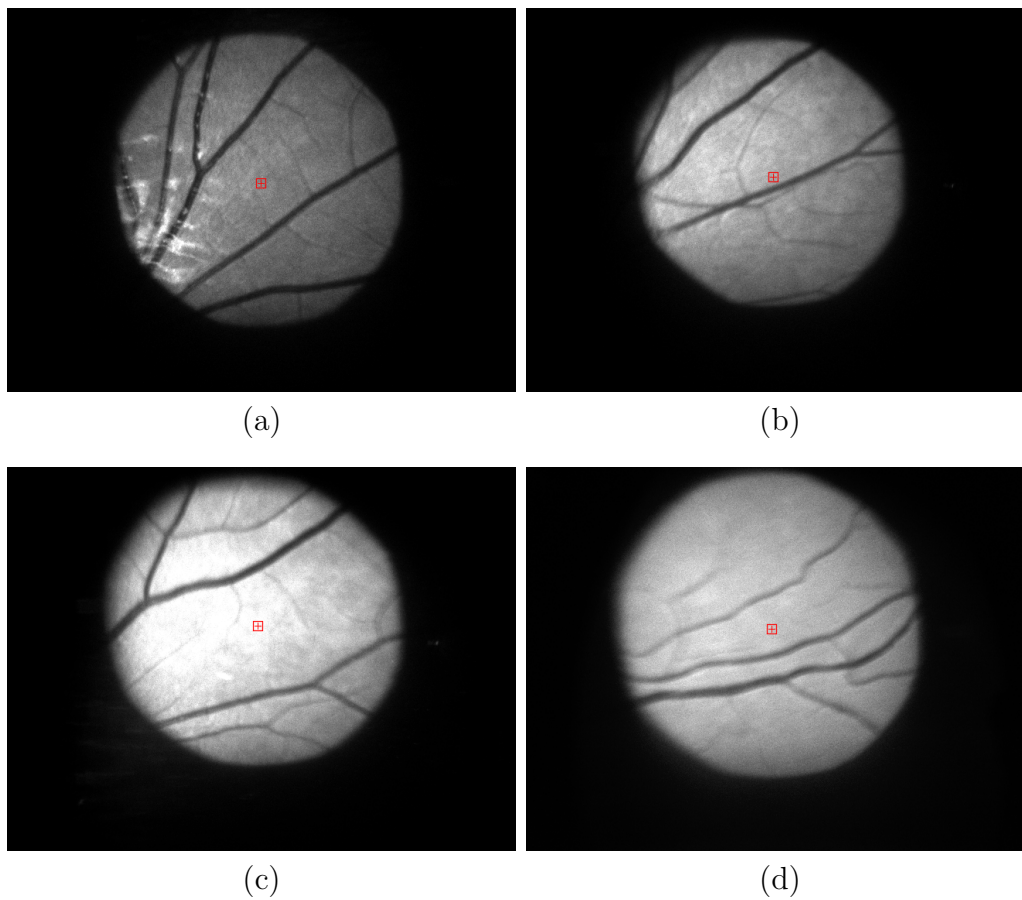


Figure 4.26: Four images taken during the search for the proper conditions: An acceptable image (a), an image with its center very close to a vein (b), a partially saturated image (c) and a blurred image (d).

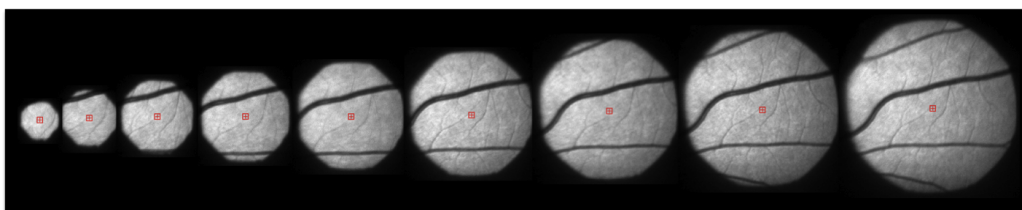


Figure 4.27: A sequence of 9 disks projected on the retina. The central patch used for the reconstruction of the PSF is depicted in red.

of the recorded image was calculated. The test showed that after the first 5 images the photoreceptors are indeed adapted.

For the determination of the center of the disk a MATLAB function was written, which can be found in appendix C.3. In order to reduce errors due

to thermal noise, instead of taking a single point as the intensity at the center of each projected disk, the intensity was set to be the mean value of a central square patch of an area of 9×9 pixels, or roughly 16×16 minutes of arc for the particular setup.

One subject (D.C) performed the experiment for four different wavelengths, two subjects (A.P. and J.M.) for three different wavelengths and the rest for two wavelengths.

Despite the fact that for the scattering measurements only the relative fundus reflectance between different disks was important, and thus it was important to make sure that no light is apodized at the pupil throughout the measurement, extra attention was paid to keep the same conditions for all subjects so that the reflected light could be directly compared. Moreover, using a 99% flat-spectrum reflector for the artificial eye the reflected light was properly normalized to correspond to the real value. In average the reflectance values were in accordance with the values found by (Delori and Pflibsen, 1989).

The data collected from the measurement of a single subject (D.C.) for 4 different wavelengths is shown in fig. 4.28, along with the fitted functions.

For the reconstruction of the eye's wide-angle PSF the glare function fit was used, as described in detail in section 4.1.2. As mentioned earlier, only data over 2.5 degrees were used in the fit where fundus diffusion becomes less relevant. The reason for that can be seen in the fits in fig. 4.28. The fit curves, although based only on points over 2.5 degrees, seem to describe very well all experimental points at shorter wavelengths. This is not, however, the case at longer wavelengths where it fails to correctly describe the lower angle points. This deviation is due to the fact that the PSF for the standard observer, since it is based also on psychophysical data, does not fully account for fundus diffusion which is significant at longer wavelengths.

Moreover, as seen in chapter 2, for longer wavelengths diffusion at the fundus is much higher and becomes comparable to scattering in the optics even at greater angles. This essentially means that it is more complicated to separate the contribution of the fundus and the contribution of the optics in the PSF. Nevertheless, as seen in fig. 2.12 on page 50, one can safely assume that over 4 degrees fundus diffusion for wavelengths around 650nm is not contributing. Therefore, in order to make a safe estimation of scattering in the optics one needs to exclusively use data over 3.5-4 degrees for longer wavelengths.

It is important to note here that mainly due to dust particles and uniformities of the optical elements the system also introduces scattering that needs to be taken into account in the measurements. Therefore, in order to have a correct estimate for intraocular scattering, one needs to subtract

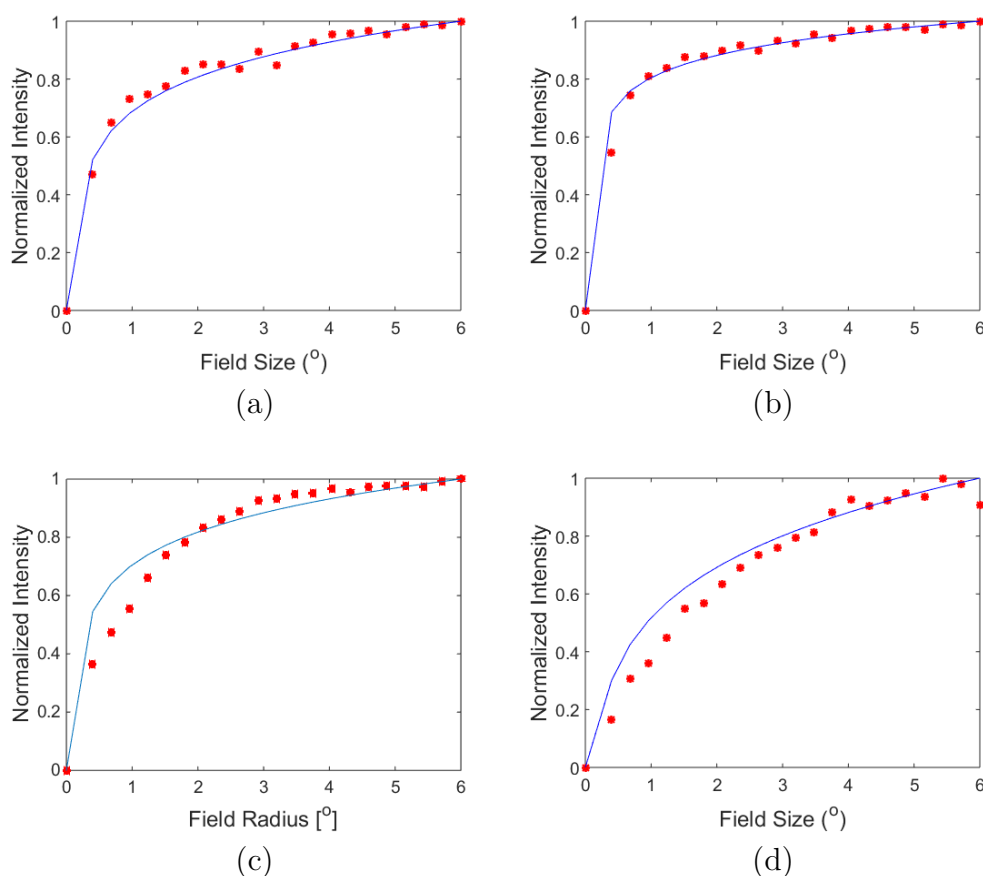


Figure 4.28: Normalized intensity at the center of the projected disc with respect to disk radius in degrees at 450nm (a), 550nm (b), 632nm (c) and 800nm (d).

system's scattering from each measurement. For the measurement of intraocular scattering an artificial eye consisting of a 20mm plano-convex lens and a 99% reflective flat spectrum background was used, and the scattering was calculated using the glare function fit, as in real subjects.

As seen in fig. 4.29 scattering is significantly higher at both shorter and longer wavelengths than at green. For example at 5 degrees the PSF for infrared can be almost 15 times higher than that of green. Similarly the PSFs at 5 degrees at red and blue are about 0.6 and 3.6 times higher respectively than that of green. The intensities and the respective reconstructed PSFs for 2 more subjects (J.M. and L.H.) at two wavelengths are shown in fig. 4.30 and fig. 4.31 respectively.

In table 4.2 the logarithm of the scatter parameter S (see eq. (1.23)) at 3 degrees is shown for all 7 subjects for the available wavelengths.

From table 4.2, one can easily see how scattering depends on wavelength.

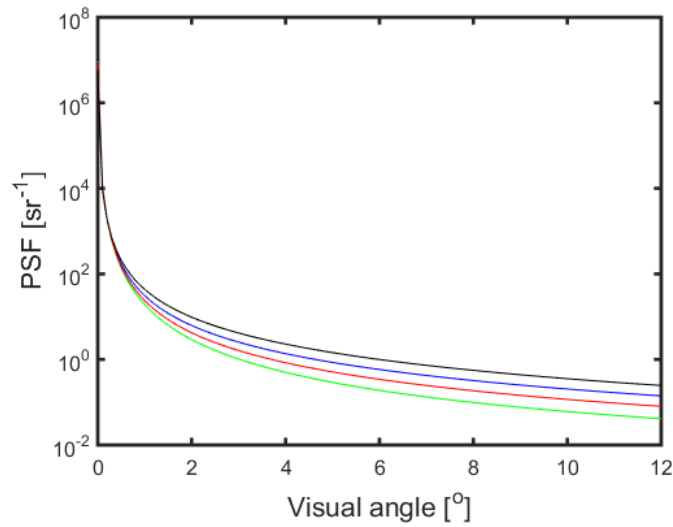


Figure 4.29: Reconstructed PSFs for subject D.C. at 450nm (blue), 550nm (green), 632nm (red) and 800nm (black).

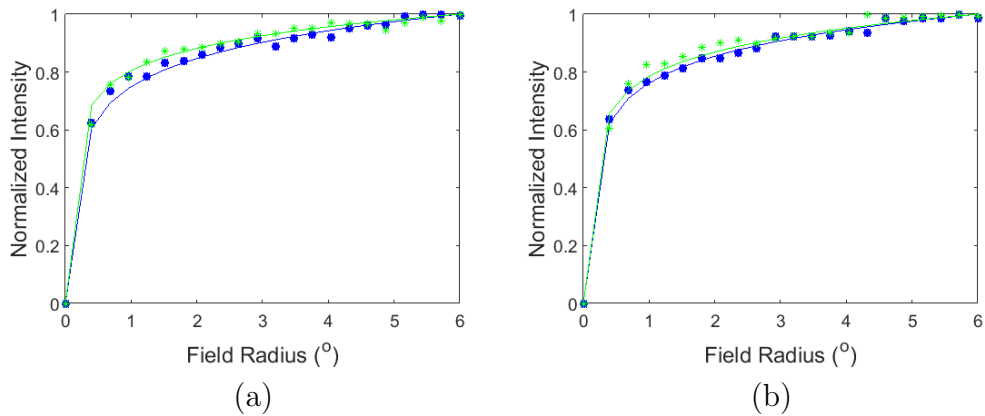


Figure 4.30: Normalized intensities at the center of the projected disk with respect to disk radius at 550nm (green) and 450nm (blue) for subject J.M. (a) and L.H. (b). The squares represent actual experimental data and the lines the fitted intensity curves using the glare function.

Scattering exhibits a minimum at 550nm, with values increasing for both shorter (450nm) and longer (632nm, 800nm) wavelengths. The average relative to 550nm increase at 450nm for all 7 subjects is 1.64 with a standard deviation of 0.47, whereas for 632nm the respective increase for 3 subjects is 1.34 with a standard deviation of 0.18.

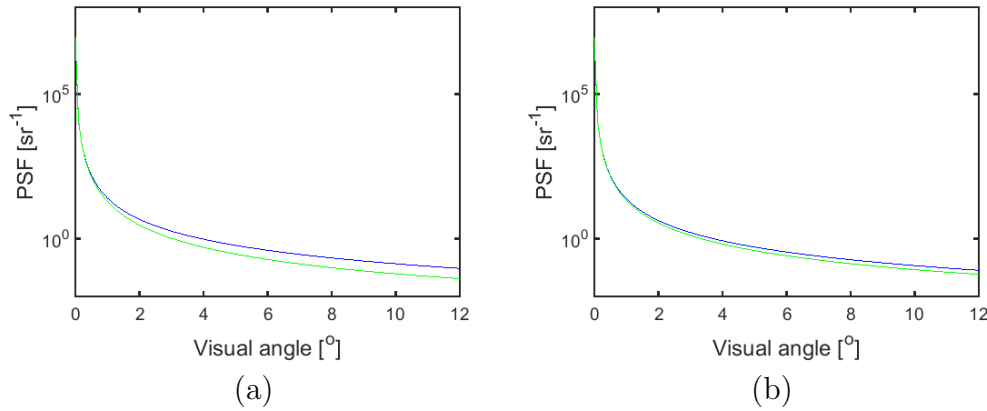


Figure 4.31: Reconstructed PSFs at 550nm (green) and 450nm (blue) for subject J.M. (a) and L.H. (b).

Table 4.2: Logarithm of the scatter parameter S at 3 degree for 7 subjects for the available wavelengths

Subject	Log(S)			
	450nm	550nm	632nm	800nm
B.L.	1.29	1.01	-	-
M.S.	1.21	0.98	-	-
S.H.	1.32	1.32	-	-
A.P.	1.31	1.15	1.24	-
D.C.	1.35	0.96	1.15	1.56
J.M.	1.20	0.96	1.05	-
L.H.	1.15	1.05	-	-

4.3.5 Fundus Image Acquisition and Scattering compensation

The setup of fig. 4.18, as explained in section 4.3.1 can also function in single mode, where it can take single images of the fundus, at the desired wavelength, eccentricity and field size. The preparation is identical as in the PSF reconstruction case: first find the ideal pupil position using the 2-camera subsystem, then set the desired wavelength and take a few trial images to find the best focus by moving the camera. Finally, set the EMCCD camera's parameters accordingly in order to acquire a non-saturated, high contrast image. Ideally, as with the PSF reconstruction procedure, the exposure time must be set such that is high enough to have a relatively high signal but

low enough so that any saccades do not affect the measurement. Usually the two tests -scattering and single image- are done consequently. In order to acquire an image with a higher signal-to-noise ratio we take a number of pictures, we perform an intensity based image registration (see fig. 4.25 on page 93) to compensate for any involuntary eye movements between pictures and create a new image by taking the sum of all images. An example is shown in fig. 4.32 where the two relatively noisy images (a),(b) are registered and added to produce a better quality image (c).

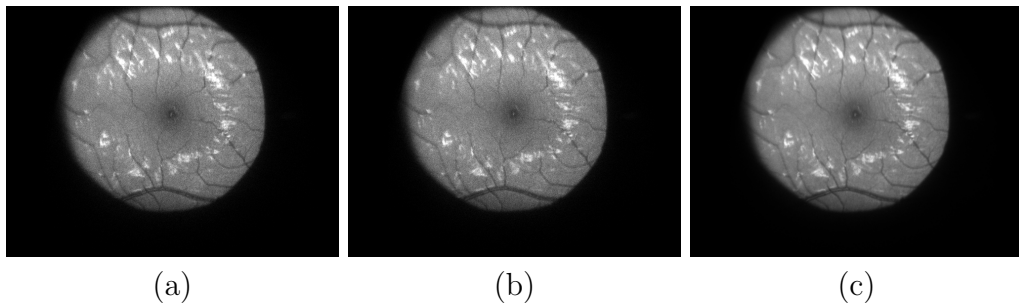


Figure 4.32: Partial images (a),(b) and final image (c) after registration and summation of the partial images.

Once the image is taken the procedure of section 4.1.4 is applied in order to reconstruct the contrast of the original image. The reconstruction is done according to section 4.3.5. It reads

$$Image_{orig} = \mathcal{F}^{-1} \left\{ \mathcal{F} \{Image\} \frac{\mathcal{F} \{PSF_{diff}\}}{\mathcal{F} \{PSF_{scat}\}} \right\}$$

where the Fourier transform of the diffraction limited PSF, is approximated by that of a square aperture. As an example, fig. 4.33 shows the scattering MTF and the diffraction limited MTF of the system for subject D.C. at 450 nm, as well as the filter function in the frequency domain. Additionally, in order to highlight the difference between a typical aberrated MTF and a scattering MTF reconstructed using the above method, a scattering MTF and two defocus MTFs are plotted in fig. 4.34. It is clear that the effect of scattering is limited in the low frequencies and has almost no effect in the higher frequencies, contrary to a system with defocus.

Applying the algorithm to a fundus image will effectively increase its contrast. The amount of the increase depends on two of things: the amount of scattering the eye has at the particular wavelength but also the dynamical range of the image. The latter means that the effect of scattering will be greater, or better more noticeable, when the image has both high reflective and high absorbing areas, in the same way that visually, scattering is much

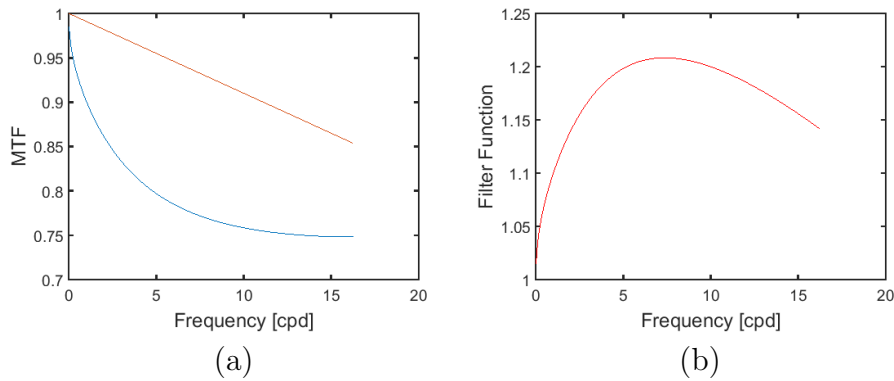


Figure 4.33: Scattering (blue) and diffraction limited MTF (red) of the system for subject D.C. at 450 nm (a) and the filter function in the frequency domain (b).

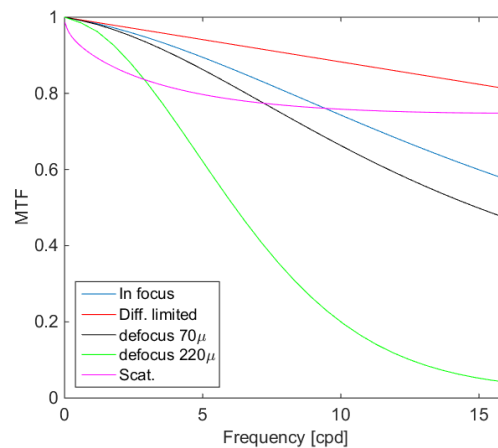


Figure 4.34: MTFs showing the effect of diffraction, high and low order aberrations and scattering.

more noticeable when driving at night, where the dynamic range is large due to the headlights, than at day. Examples of a 6 degrees radius foveal image before and after the compensation of scattering at 450nm and 632nm are shown in fig. 4.35 and fig. 4.36 respectively. In both cases, scattering consistently reduces the contrast by causing light from the bright areas to be spread over the image, thus increasing light intensity at darker sites. In all cases, the background of the system was first subtracted and solely the effect of the intraocular scattering is shown.

In order to give a more realistic idea of the effect of scattering in the measurement of fundus reflectance, for the first example the intensity at two sites, one at the fovea and one at the perifovea depicted in red and blue

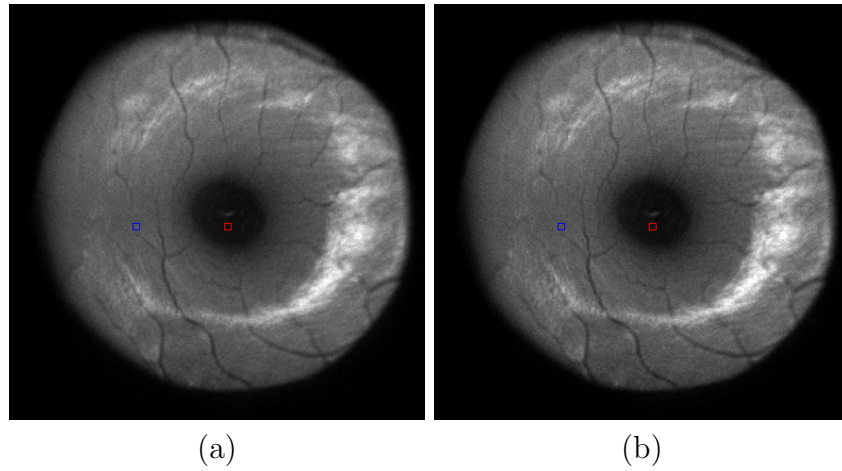


Figure 4.35: A 6 degrees radius foveal image before (left) and after (right) scattering compensation at 450nm.

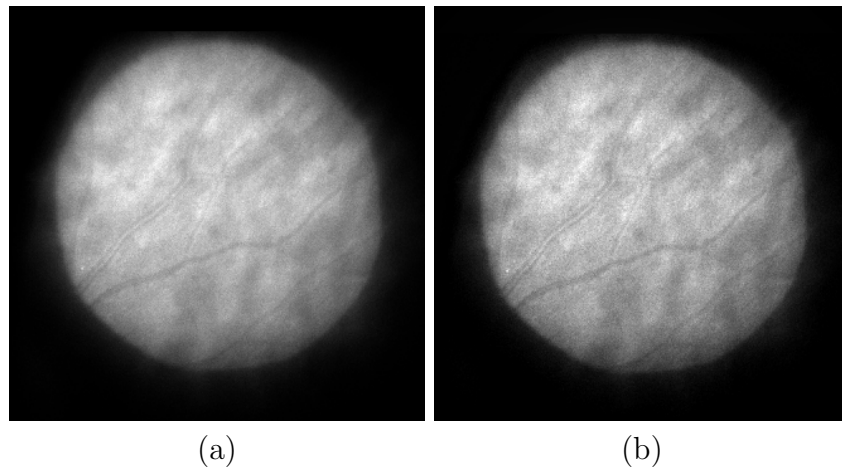


Figure 4.36: A 6 degrees radius image at about 8 degrees nasally before (left) and after (right) scattering compensation at 632nm.

squares in fig. 4.35 respectively, was measured. The red site is an area of very low reflectance-high absorption, whereas the blue site of average reflectance-absorption. The ratio of the intensities at the two sites before and after scattering was then calculated and finally, the increase in the ratio between the two images was compared by taking the ratio of the ratios

$$\frac{\left. \frac{I_P}{I_F} \right|_{scatt}}{\left. \frac{I_P}{I_F} \right|_{noscott}} = 1.0911 \quad (4.21)$$

The above result means that there an about 10% increase in the ratio peri-fovea to fovea of a blue fundus image. This can be understood as if scattering is "stealing" light from the maxima and "giving" it to the minima of the image. In the following chapter an example will be presented showing how this affects an actual clinical measurement, the measurement of macular pigment.

Scattering in Macular Pigment Optical Density measurements

There is a number of methods to measure the optical density of the Macular Pigment, some of them optical and other psychophysical. From the optical methods the most commonly used is the reflectometry method, which as the name suggest uses the reflected from the fundus light, and as such, as shown in the previous chapter, is affected by scattering.

In this chapter the effect of scattering in Macular Pigment Optical Density (MPOD) measurements using the reflectometry method is studied and a method for its compensation is presented. Additionally, in order to validate the results from this novel method of compensation, they were compared against a psychophysical method using a custom-made apparatus based on Heterochromatic Flicker Photometry (HFP).

5.1 MPOD measurement using fundus reflectometry

The method consists of the intensity analysis of two fundus images taken at green where the MP absorption is minimal and at blue where the absorption is maximal, as shown in fig. 5.1. The images need to extend enough so that they contain both the fovea, where the highest concentration of MP is found, and the perifovea where concentration falls approximately to zero (Snodderly et al., 1984a). Ideally, the largest the field, the better, however, the field is limited by the resolution of the camera and therefore the magnification is set appropriately in order to have a good trade off between image resolution and field size.

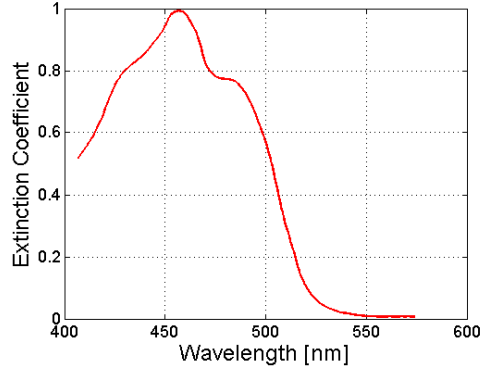


Figure 5.1: Macular pigment absorption spectrum normalized at 455nm by Brown and Wald (1963).

For the analysis a simplified fundus model was assumed containing 4 different absorbers. A schematic of the model used for the calculations is shown in fig. 5.2.

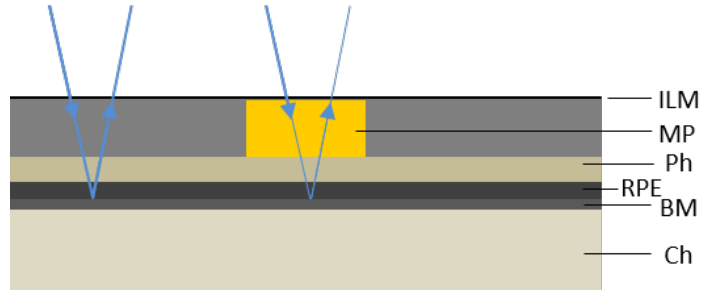


Figure 5.2: Simplified fundus model used for the calculation of MP. The layers from top to bottom: Inner Limiting Membrane (ILM), Macular Pigment (MP), Photoreceptor Layer (Ph), Retinal Pigment Epithelium (RPE), Bruch's Membrane (BM) and Chorioid (Ch).

Assuming that no light is attenuated before the MP, then the reflectance measured at the camera is related with the MPOD through the relation

$$R(x, y, \lambda) = 10^{-D(\lambda)} R^*(x, y, \lambda) 10^{-D(x, y, \lambda)}$$

$$R(x, y, \lambda) = R^*(x, y, \lambda) 10^{-2D(x, y, \lambda)} \quad (5.1)$$

where R^* is the reflectance of all layers posterior to the MP and D its optical density. The factor 2 at the above relation is due to the fact that light travels twice through the MP before being recorded by the camera. For two different sites x, y and x', y' , taking the log-ratio one obtains

$$\log \frac{R(x, y, \lambda)}{R(x', y', \lambda)} = \log \frac{R^*(x, y, \lambda)}{R^*(x', y', \lambda)} + 2(D(x', y', \lambda) - D(x, y, \lambda)) \quad (5.2)$$

Replacing the optical density difference between the two sites $D_{MP}(\lambda) = D(x', y', \lambda) - D(x, y, \lambda)$ and expressing then that density difference as a function of the extinction coefficient $K_{MP}(\lambda)$ from fig. 5.1, eq. (5.2) becomes

$$\log \frac{R_P(\lambda)}{R_F(\lambda)} = \log \frac{R_P^*(\lambda)}{R_F^*(\lambda)} + 2D_{MP}(460)K_{MP}(\lambda) \quad (5.3)$$

where we let site x, y be at the perifovea (P) and site x', y' at the fovea (F). Applying eq. (5.3) for two different wavelengths λ_1 and λ_2 and subtracting one equation from the other one gets

$$\begin{aligned} \log \frac{R_P(\lambda_1)}{R_F(\lambda_1)} - \log \frac{R_P(\lambda_2)}{R_F(\lambda_2)} &= \log \frac{R_P^*(\lambda_1)}{R_F^*(\lambda_1)} - \\ &\log \frac{R_P^*(\lambda_2)}{R_F^*(\lambda_2)} + 2D_{MP}(460)(K_{MP}(\lambda_1) - K_{MP}(\lambda_2)) \end{aligned} \quad (5.4)$$

Assuming now that the reflection spectrum at the perifovea is proportional to the reflection spectrum at the fovea, then that the ratio $\frac{R_P^*(\lambda)}{R_F^*(\lambda)}$ is constant for all wavelengths, and therefore eq. (5.4) simplifies to

$$\log \frac{R_P(\lambda_1)}{R_F(\lambda_1)} - \log \frac{R_P(\lambda_2)}{R_F(\lambda_2)} = 2D_{MP}(460)(K_{MP}(\lambda_1) - K_{MP}(\lambda_2)) \quad (5.5)$$

Finally, solving for D_{MP} and rearranging we get

$$D_{MP}(460) = \frac{0.5}{(K_{MP}(\lambda_1) - K_{MP}(\lambda_2))} \left(\log \frac{R_P(\lambda_1)}{R_P(\lambda_2)} + \log \frac{R_F(\lambda_2)}{R_F(\lambda_1)} \right) \quad (5.6)$$

From eq. (5.6), it can be understood that the periphery reflectance, given that the macular pigment exists solely at the fovea, essentially calibrates the calculation.

A number of assumptions were made in order to come down to the above formula, with most important one that of treating the fundus posterior to the MP as a uniform reflecting surface. For short and middle wavelengths below 580nm, reflections occur mostly at the RPE and at Bruch's membrane (Delori and Pfibsen, 1989; Gorrand et al., 1984) and therefore melanin density at the RPE affects heavily the amount of reflected light. This is also supported by the findings at chapter 3, where at 550nm there was no difference in the reflectance amongst subjects with different choroidal melanin pigmentation amounts, which was not the case at 650nm. Since RPE melanin is not constant throughout the fundus but exhibits a higher density at the fovea,

it contributes in MPOD reflectometry measurements. In order to take into account that melanin density difference one could rewrite eq. (5.3) as follows

$$\log \frac{R_P(\lambda)}{R_F(\lambda)} = \log \frac{R_P^*(\lambda)}{R_F^*(\lambda)} + 2D_{MP}(460)K_{MP}(\lambda) + nd_{ME}K_{ME}(\lambda) \quad (5.7)$$

where d_{ME} is the single pass melanin density difference between the fovea and the perifovea, K_{ME} an extinction coefficient for melanin, n a factor that takes value up to 2 and describes the depth where the reflection takes place (2 being a full double pass of the light) and R^* the fundus reflectance in the absence of MP and RPE melanin. Following the same analysis as before and substituting equation 5.6 a more generalized formula for the MP holds

$$D_{MP,G}(460) = D_{MP}(460) - \frac{n}{2}d_{ME} \left(\frac{K_{ME}(\lambda_1) - K_{ME}(\lambda_2)}{K_{MP}(\lambda_1) - K_{MP}(\lambda_2)} \right) \quad (5.8)$$

Delori et al. (2001) calculated for $\lambda_1 = 470nm$ and $\lambda_2 = 550nm$ the contribution of the last term to the calculation of the MPOD. They found that for a value of the nd_{ME} of 0.13 *D.U.* the contribution to the MPOD was about 0.03 *D.U.*, concluding thus that the melanin difference across the fundus has a limited effect on the estimation of the MPOD.

Another factor which was overlooked was the directionality of the photoreceptors. The reason for this convenient negligence was that since in the setup, the illuminating and imaging angles are relatively large (about 5 degrees), because of the pupil configuration used (see fig. 4.20) waveguiding is relatively low at those angles (Delint et al., 1997). Tests prior to the experiment supported this fact.

The methodology that was followed for the extraction of the macular pigment was simply the application of equation 5.6 using the intensities as recorded by two images of the fundus, of 6 degrees radius, one at 450nm (FWHM=40nm) and one at 550nm (FWHM=40nm). The respective transmission spectra of the filters used for the illumination are shown in fig. 5.3.

The fundus images were acquired with the double pass system shown in fig. 4.18 on page 86 and following the process for single image acquisition described in section 4.3.5. The image registration was done using MATLAB's `imreg` function (see section 4.3.2 on page 91 for more details) so that each pixel depicted the exact same retinal region. A filter function was then applied to all images, in order to exclude irrelevant structures, such as axons of ganglion cells at the nerve fiber layer, mostly visible in blue (Knighton et al., 1989; Knighton and Huang, 1999), and blood vessels which exhibit a higher contrast in green, due to the absorption spectrum of hemoglobin (van

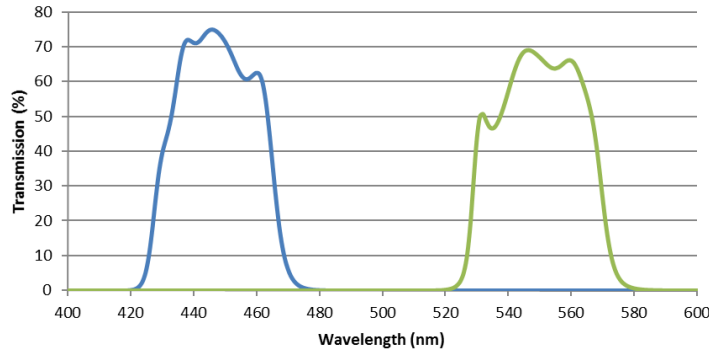


Figure 5.3: Transmission spectrum of bandpass filters peaking at 450nm (blue) and at 550nm (green) used for the measurement of the MPOD.

Kampen and Zijstra, 1983). In this particular setup, a blood vessel appears about 8 pixels, depending on the site, or about 13 minutes of arc, so the low-pass filter was chosen such that frequencies higher than about 2 cycles per degree fall to zero, thus affecting solely the high frequency patterns and not the macular pigment. This was done by multiplying the final PSF by an appropriate function in the Fourier domain. The function used was

$$f(r) = e^{-ar^6} \quad (5.9)$$

where a is a parameter that related to the frequency cut-off limit and $r = \sqrt{x^2 + y^2}$. An example of the MTF before and after the filtering is shown in fig. 5.4. The effect of the above filter function on a fundus image is shown in fig. 5.5.

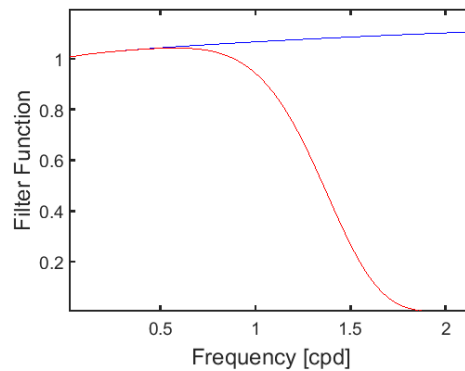


Figure 5.4: Low pass filter function in the Fourier domain for the elimination of higher frequencies.

The values for the extinction coefficients was extracted from Brown's data presented in fig. 5.1 on 106 and were found to be $K_{MP}(450) = 0.9566$ and

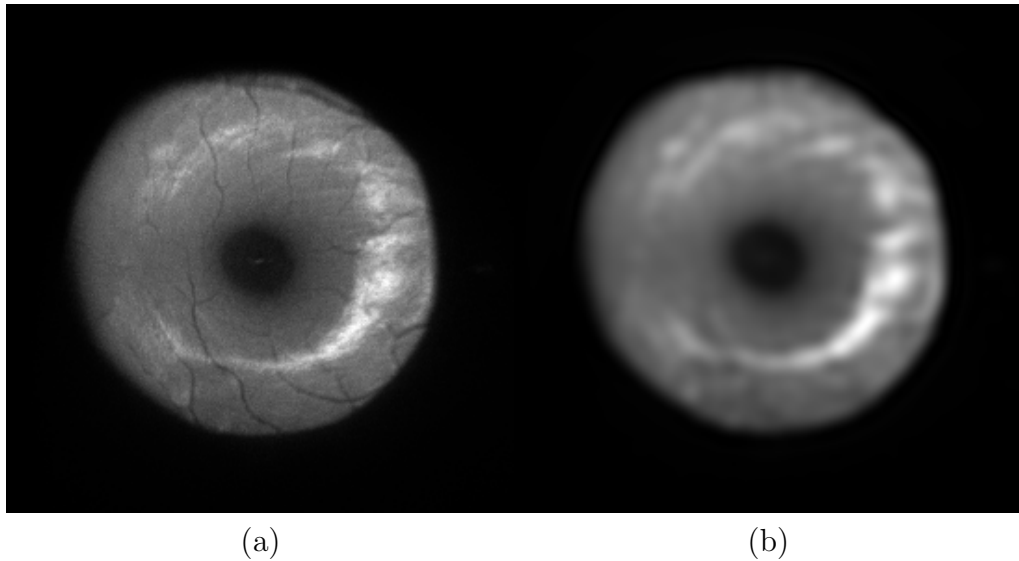


Figure 5.5: Example of a fundus image before (a) and after (b) applying the filter function of fig. 5.4.

$K_{MP}(550) = 0.0087$. There is a number of different metrics that can be used for the calculation of the MPOD, like the median, the peak value, the weighted average etc. For the present study, the average value for an area of 1 degrees around the center of the fovea was chosen as a final value for the MPOD.

In order to see the effect of scattering in the MPOD measurement, the above technique was applied for both the original images without any enhancement and the images after the scattering compensation, as described in section 4.3.5.

In short, the complete algorithm followed for each of the seven subjects was the following

1. Reconstruct the wide angle PSF at 450nm and 550nm.
2. Take two foveal images of 12 degrees diameter at 450nm and 550nm.
3. Register the two images and apply the low-pass filter.
4. Using the respective PSFs calculated at step 1, compensate scattering at the fundus images.
5. Apply eq. (5.6) to both the original set of images and the enhanced ones and extract the MPOD distributions.

6. Take the mean for a 1 degree region around the fovea for each distribution and compare the the results.

It needs to be noted here that not all MPOD measurement techniques suffer at the same degree from scattering. In this particular study, only the effect of scattering in the reflectometry method is examined. For more details about how scattering affects different methods see table 2 from Leung (2008), though the paper gives only a very rough estimate.

The complete process was done for seven subjects (see section 4.3.3 for details on the subjects). As an example, the measured MPOD distributions after applying the enhancement technique for four subjects are shown in fig. 5.6. The MPOD profile distributions for all 7 subjects are presented

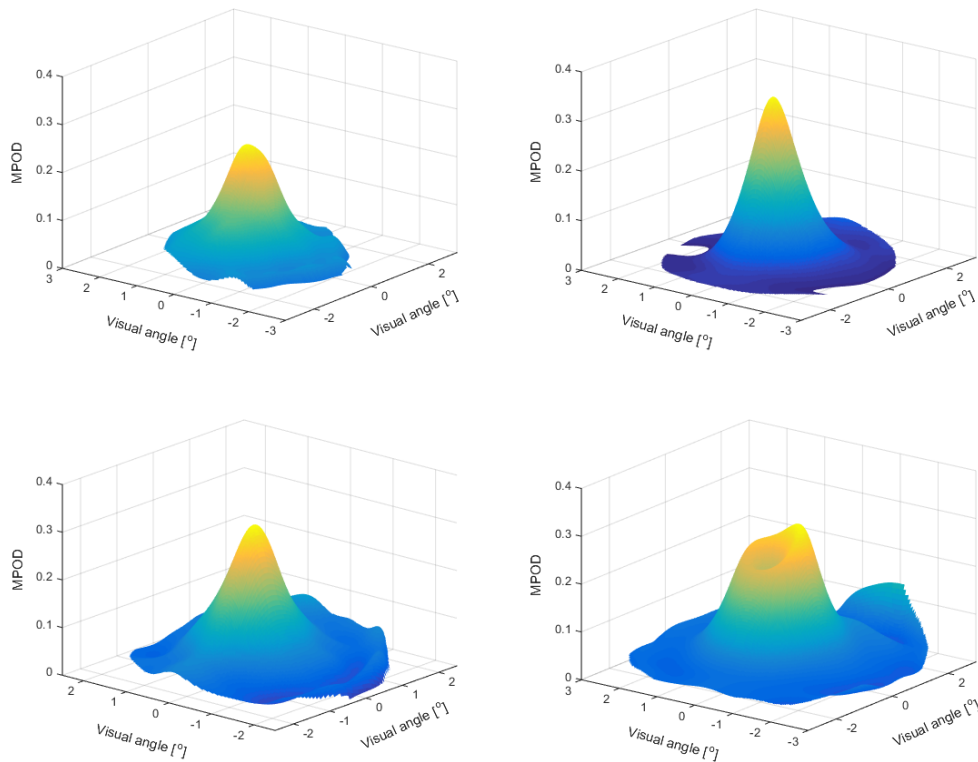


Figure 5.6: MPOD spatial distributions after scattering compensation for 4 subjects.

graphically in fig. 5.7 for both cases, i.e. with scattering compensation (red) and without (blue). The final values for the MPOD as well as the relative increase with and without the scattering compensation is shown in table 5.1.

There is an important factor that could lead to a wrong estimation of the macular pigment optical density with this method: the specular reflec-

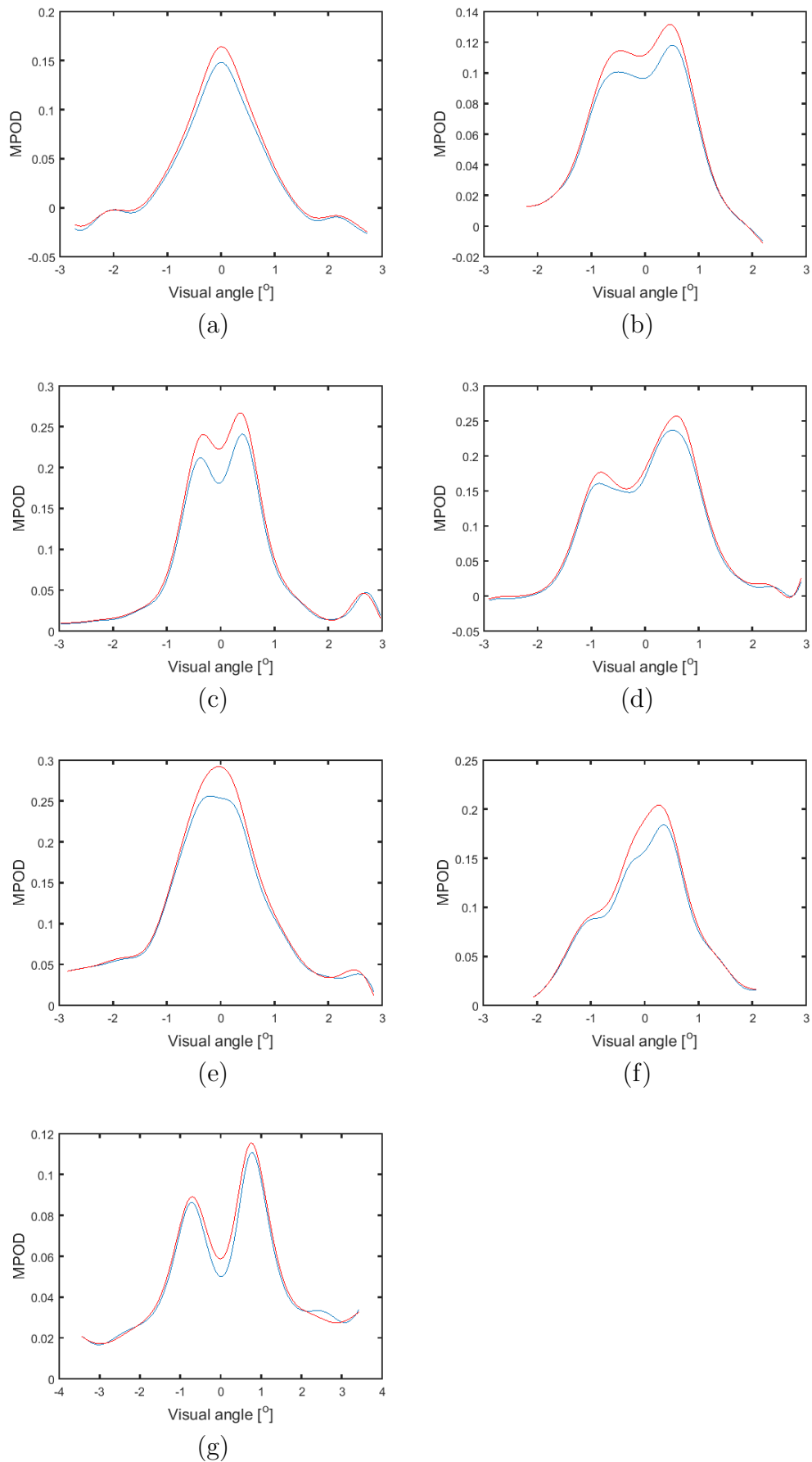


Figure 5.7: MPOD profile before (blue) and after (red) scattering compensation for the seven subjects.

tions, mainly taking place at the interface between the aqueous humor and the inner limiting membrane (ILM) (Delori and Pflibsen, 1989). Those specular reflections arrive at the camera sensor under very specific conditions, depending on the parameters of the system such as the incident angle of the rays and the curvature of the fundus. The specular reflections were higher in younger subjects in both our study and previous studies (Gorrand and Delori, 1999; Delori et al., 2001). Such specular reflections can be seen in almost all fundus images (e.g. fig. 4.25 on 93), especially at middle and short wavelengths at about 3 degrees at the perifovea. Those reflections at the perifovea may affect the measurement to some extent, since they could act as glare sources¹. In order to make sure that any scattered light introduced by that effect is properly compensated, it was assured that the pixels at the sites where the specular reflections occur, were not saturated, though were close to saturation, so that the intensity values for the rest of the image were kept the highest possible.

Another phenomenon, also related to specular reflections, occurs at the center of the foveola, where the retinal surface forms a spherical-shaped pit of curvature of about 1mm radius, that depends strongly on the age (Gorrand and Delori, 1999; Delori et al., 2001). An OCT scan showing that curvature, can be seen in fig. 5.8. Since these reflections at the foveal pit happen before

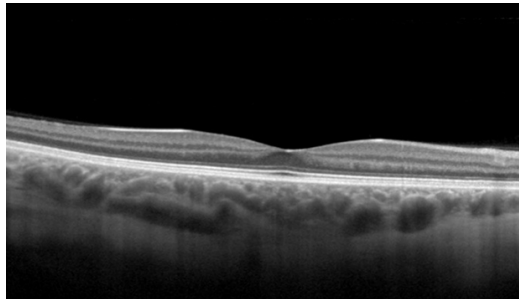


Figure 5.8: OCT scan of the fovea. The foveal pit can be seen at the very center of the foveola.

reaching the RPE layer, they are not screened by the MP, and therefore the above algorithm would give a wrong estimate for the MPOD at those sites. Nevertheless the specular reflectance is not the same for the two wavelengths, mainly due to the different intensity between wavelengths and possible ro-

¹This effect can lead to a more severe underestimation of the MPOD in younger subjects than in older ones where the specular reflections are lower. Nevertheless, older individuals exhibit higher intraocular scattering which as we have seen earlier is also causes an underestimation. Further studies are needed for a more quantitative investigation of the two antagonistic effects.

tations of the retina when capturing the two images. The way this affects the measured MPOD distribution can be seen in fig. 5.7(b),(c),(d),(g) where the effect is stronger in the last image, leading to an underestimation of the MPOD. There is a number of techniques that could reduce those specular reflections, such as changing the geometry of the system, using of polarizers or applying appropriate algorithms at the fundus images. Nevertheless, in most cases the effect was minor and the analysis was done normally.

Table 5.1 shows the values for the MPOD before (second column) and after (third column) scattering compensation for the seven subjects tested, as well as the relative change (fourth column). As seen in the table, the underestimation of the macular pigment when scattering is not taken into account ranges between 7.8 and 13%, with an average of 10.23%. The average MPOD before the compensation was found to be 0.1431 ± 0.0623 and 0.1639 ± 0.0573 after compensation. The importance of the effect, depends on the amount of intraocular scattering at blue and green, their difference, specular reflections in the image, as well as the distribution characteristics of the macular pigment itself.

Table 5.1: MPOD values before and after scattering compensation as well as the relative change between the two measurements for seven subjects.

Subject	MPOD (no compens.) [D.U.]	MPOD (compens.) [D.U.]	Relative Increase [%]
M.S.	0.1129	0.1249	10.6
D.C.	0.2109	0.2383	13.0
B.L.	0.1092	0.1224	12.1
S.H.	0.1552	0.1696	9.3
L.H.	0.1780	0.1918	7.8
J.M.	0.2012	0.2197	9.2
A.P.	0.0734	0.0804	9.6

5.2 MPOD measurement using the Heterochromatic Flicker Photometry method

A psychophysical setup based on the Heterochromatic Flicker Photometry (HFP) method (Wooten et al., 1999) was developed for the qualitative validation of the optical method described in the previous section. The purpose was by no means to build a perfect psychophysical system for the calculation

of the MPOD, but to build a control system that could be used as a qualitative reference for the optical method described in the previous chapter.

The principle of the method of HFP is the same as the one described in section 1.6.2. As with that system, the concept is the following: equate the luminance for two lights of different wavelengths flickering in counter-phase and at a constant frequency. Since the luminance is equal, the ratio of the intensities that cancels -or minimizes- the flicker is essentially the ratio of the sensitivities for the respected wavelengths. The presence of the MP can affect the measurement in a very specific way: since the MP absorbs only short wavelengths and is confined within the fovea, it would affect a test which uses a short-middle wavelength light combination and only at the fovea. In other words if one performs the test using blue-green sources at the fovea and at the perifovea, the difference in the test between the two sites will be affected by the presence of the macular pigment. Assuming a blue-green test at two sites, at the fovea and the perifovea then the luminance match at each site can be expressed mathematically as

$$I_F^B 10^{-D_F^B} S_F^B = I_F^G 10^{-D_F^G} S_F^G \quad (5.10)$$

$$I_P^B 10^{-D_P^B} S_P^B = I_P^G 10^{-D_P^G} S_P^G \quad (5.11)$$

where I the intensities of minimal flicker, D the optical densities of the MP and S the photoreceptor sensitivities at the fovea and at the perifovea and for the two colors. Dividing eq. (5.10) by eq. (5.11) we get

$$\frac{I_F^B}{I_P^B} 10^{D_P^B - D_F^B} \frac{S_F^B}{S_P^B} = \frac{I_F^G}{I_P^G} 10^{D_P^G - D_F^G} \frac{S_F^G}{S_P^G} \quad (5.12)$$

$$\Rightarrow \frac{I_F^B}{I_P^B} 10^{-D_{MP}^B} \frac{S_F^B}{S_P^B} = \frac{I_F^G}{I_P^G} 10^{-D_{MP}^G} \frac{S_P^B}{S_P^G} \quad (5.13)$$

where in the last one we let $D_{MP} = D_F - D_P$. Before moving further on with the algebra, there are three very important assumptions that need to be made;

- Short wavelength cones and rods are not involved in the detection.
- The optical density of the photopigments is the same in the fovea and the perifovea.
- The long to middle cone ratio is the same in the fovea and the perifovea.

The first assumption can be fulfilled by selecting the background in a way that chiefly stimulates the cone classes that are not desired to participate

in the detection. A background with a peak at 470nm for example, at the peak of the S cone sensitivity, that stimulates selectively the S cones and it is intense enough to saturate the rods would be suitable for that purpose. The importance of the background in HFP tasks is explained in detail in Sharpe et al. (2005); Brindley et al. (1966). The second assumption is somehow more complicated. There have been a number of studies investigating the effect of the change of the optical density of the photoreceptors with eccentricity on sensitivity and in macular pigment measurements (Sharpe et al., 1998; Werner et al., 2000), a phenomenon also known as self-screening. Nevertheless, Delori et al. (2001) using the extinction spectra for the L and M cones from previous studies (Stockman and Sharpe, 2000) concluded that the MPOD values determined by the HFP method are underestimated only by 0.01-0.07 D.U. for all MPOD values. For the final assumption, there have been studies investigating the change of the L:M ratio arguing that it is relatively constant throughout the central retina (Deeb et al., 2000; Knau et al., 2001).

With the above assumptions one can now conclude that the spectral sensitivities at the two sites are proportional

$$\frac{S_F^B}{S_F^G} = \frac{S_P^B}{S_P^G} \quad (5.14)$$

Plugging eq. (5.14) into eq. (5.13) and with a little bit of algebra one gets

$$D_{MP}^B - D_{MP}^G = \log \left(\frac{I_F^B I_P^G}{I_P^B I_F^G} \right) \quad (5.15)$$

Depending on the experiment either the intensity of the blue source can vary and the green one be kept constant or the intensity of the green source can vary and the blue one be kept constant. In case of the latter, then $I_F^B = I_P^B$ and eq. (5.15) becomes

$$D_{MP}^B - D_{MP}^G = \log \left(\frac{I_P^G}{I_F^G} \right) \quad (5.16)$$

$$(5.17)$$

or by introducing the extinction coefficients relative to that at 460nm like before we get

$$D_{MP}(460) = \frac{1}{K_{MP}^B - K_{MP}^G} \log \left(\frac{I_P^G}{I_F^G} \right) \quad (5.18)$$

From this final relation, for the extraction of the MPOD using the HFP technique, only the intensities of the varying source that minimize the flicker at each of the retinal sites are needed.

The HFP technique, has been extensively used for the measurement of the MPOD, yet it needs to be understood that it is by no means a golden standard (Howells et al., 2011). Its accuracy is still under investigation though studies have shown to have a good repeatability even for untrained subjects (Van Der Veen et al., 2009; Howells et al., 2013; Loughman et al., 2012; de Kinkelder et al., 2011; Leung et al., 2003).

5.2.1 Experimental Setup

The experimental setup for the psychophysical measurement of the MPOD consisted of a 10W RGB LED source (LEDengin, Inc; CA) where only the green (525nm) and the blue (457nm) channels were used, controlled by the Arduino UNO microcontroller through a MATLAB program developed for that purpose. The LED back-illuminated a thin aluminum plate with a circular hole close to its center. The front side of the plate was covered with a white, highly reflective, flat spectrum paper and was front-illuminated by a white LED which served as a background. The high diffusing properties of the paper ensured a uniform field. On the paper there was also a small black dot which served as a fixation point for the perifovea measurement. The amount of light entering the eye was controlled by an aperture (D1) conjugate to the pupil plane. A schematic and a photo of the setup is shown in fig. 5.9 and fig. 5.10 respectively. Any myopic or hyperopic effects were compensating by translating axially the source ².

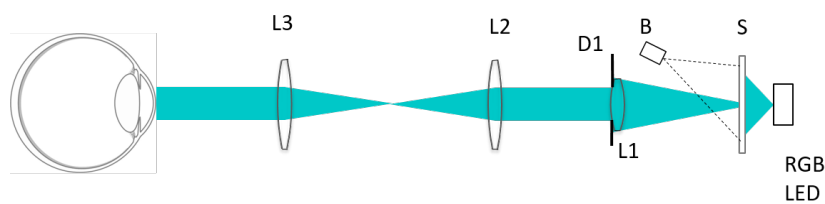


Figure 5.9: Schematic of the experimental setup for the psychophysical calculation of MPOD.

The background was set to a retinal illuminance of about 3.0 logTd and the total illuminance with the test field of 3.3 logTd. The characteristics of the optics of the system were such that the field pertained an angle of 1 degree

²Additionally, the retinal plane was set to be slightly off-focus, in order for the granules of the paper not to be visible.

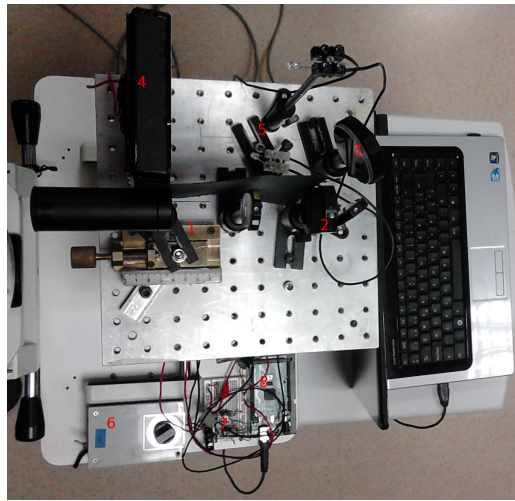


Figure 5.10: A photo of the psychophysical setup where (4) is the main component - the screen with the test field and the background and (2) an aperture conjugate to the pupil controlling retinal illumination.

and the white background an angle of 10 degrees. A MATLAB program was developed, which communicating with the Arduino micro-controller through a virtual COM port and gave full control of the intensity of the green LED and the frequency of the test field. A snapshot of the MATLAB GUI developed for the control of the experiment is shown in fig. 5.11. The Arduino and script

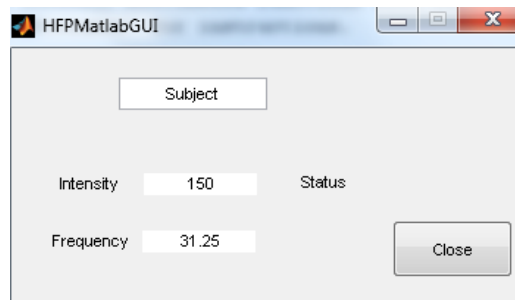


Figure 5.11: Graphical User Interface for the control of the HFP system.

developed for the control of the system can be found in appendix C. For the control of the high power LED a circuit was built that could take as input an low current analog pulse and amplify it in order to feed the high power LED. The circuit is shown in fig. 5.12. The way to produce pseudo-analog pulses with the Arduino is described in appendix D.

The subject's task was to find the intensity of the green LED that minimizes the flicker at two sites, at the fovea and at about 5.5 degrees. The

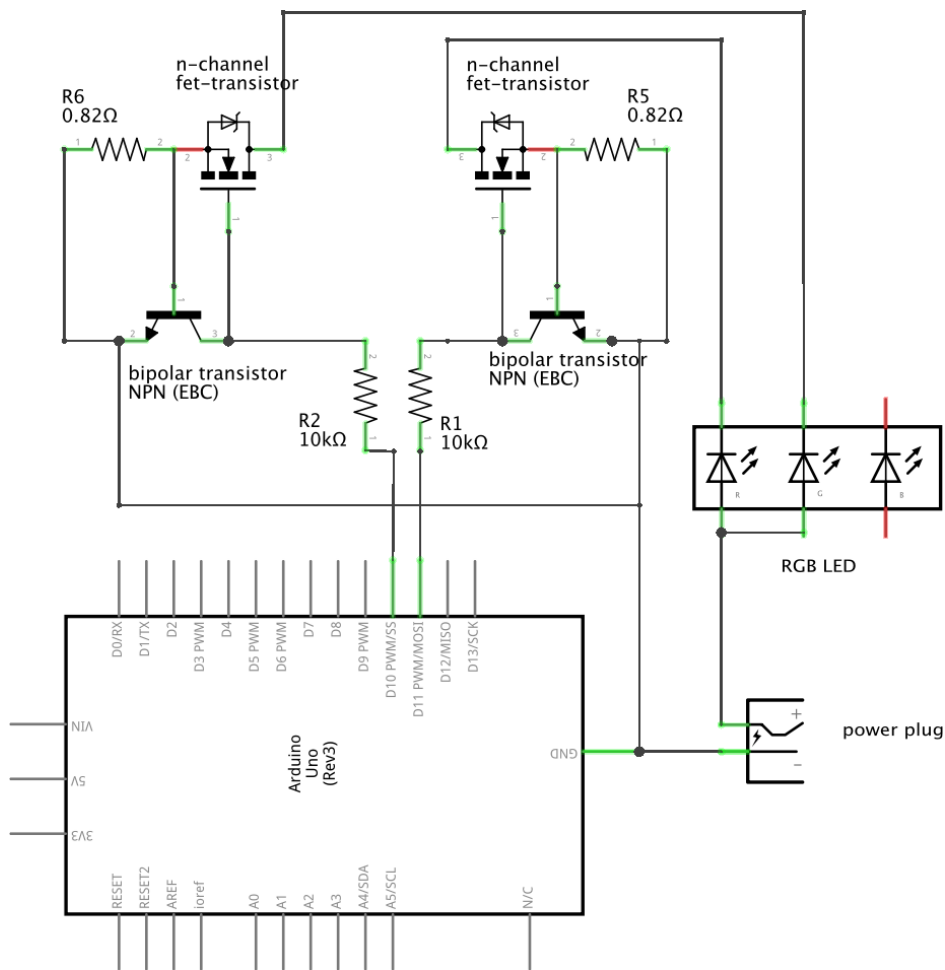


Figure 5.12: Schematic of the circuit used to drive the high power LEDs.

Table 5.2: MPOD values for six subject using the HFP method.

Subject	MPOD [D.U.]
M.S.	0.1729
D.C.	0.3429
B.L.	0.1628
L.H.	0.2614
J.M.	0.2228
A.P.	0.1572

control of the intensity and the frequency was done by the subject using the horizontal and the vertical keyboard arrows respectively. The frequency was set at an initial value for all subjects of 15 Hz at the fovea and 12 Hz at the perifovea and the subject was instructed initially to find the point of minimal flicker. The subject was instructed to change the flicker frequency only when there was more than one single intensity value for which the flicker was cancelled or when the flicker was never cancelled and the subject wasn't able to find the minimum flicker point. Before the start of the actual test, the subject was given a few minutes to get used to the control of the device and to adapt to the light conditions.

The test was done by 6 subjects and the results are shown in table 5.2. The average MPOD for the six subjects was found to be $0.2284 \pm 0.0757 D.U.$

5.3 Validation of the Reflectometry with the HFP method

Despite the fact that there is no golden standard for the measurement of the MPOD, for trained subjects, the HFP method is considered relatively reliable and with high repeatability. Therefore, as an informal validation of the RE method developed, the results from the two different devices were compared, where it was also assumed that psychophysical measurements are affected less by intraocular scattering.

In general, discrepancies in the measurement of the MPOD using different methods are expected and have been shown and discussed in a number of studies (Delori et al., 2001; de Kinkelder et al., 2011; van der Veen et al., 2009; O'Brien et al., 2013). Usually the psychophysical methods tend to underestimate low densities and overestimate higher ones compared to the RE method. This is mainly due to the fact that, as seen earlier, a number of approximations had to be made based on studies done for specific subjects.

A precise measurement would require an exact knowledge of the L:R ratio at the two sites, the melanin density change between the two sites and the self-screening done at the photoreceptors as well as a experienced subject.

On the other hand, with reflectometry, specular reflections and scattering can affect the algorithm and underestimate the MPOD. Furthermore, while in the reflectometry method the area measured is well defined, this isn't the case with the psychophysical method and therefore comparing the results from the two different methods is not trivial. Even when the conditions in both methods are identical, in the psychophysical method the MPOD seems to be determined at the edge of the test stimulus rather than the average MPOD for that test stimulus size. This effect, though already known in visual science (Ratliff, 1978), was first suggested to affect MPOD measurements by Werner et al. (1987) and it was then supported by data from Hammond et al. (1997b).

For the comparison of the agreement of the two methods the Bland-Altman analysis was performed on the data (Bland and Altman, 1986). The results of the analysis are shown in fig. 5.13, where the plot on the left shows the MPOD measurements using the HFP method against the RE method and the plot of the left is the Bland-Altman plot, i.e. the difference of the two measurements against the mean of the two measurements. As expected, since the same quantity is measure, correlation between the two methods was very strong, as seen in the correlation plot. The dashed line in the left plot represents the line where the points would lie if the two methods yielded identical results.

Despite the fact that the correlation plot is by no means an agreement test, it is a quick starting point, since low correlation between the two data sets would imply a lack of relationship between the two variables, and no further testing would be necessary. As seen in the figure, the actual regression line lies slightly lower than the ideal line, showing indeed a difference in the results, despite the very high correlation. For a more in depth comparison of the two methods one needs to study the Bland-Altman plot on the right. The heavy line shows the mean difference between the data and the two dashed lines the 95% limits of agreements. The mean difference was found to be 0.057 D.U. for the RE method with the differences of the two measurements scattered uniformly around the mean difference. The low limits of agreement show a relatively good agreement between the two methods with no biases.

Similarly, for the reflectance data without the scattering compensation, the agreement with the HFP method is good, as seen in fig. 5.14. This was expected, since the effect of scattering for the specific study group was similar and caused a systematic underestimation of the MPOD, which can also be seen in the figure.

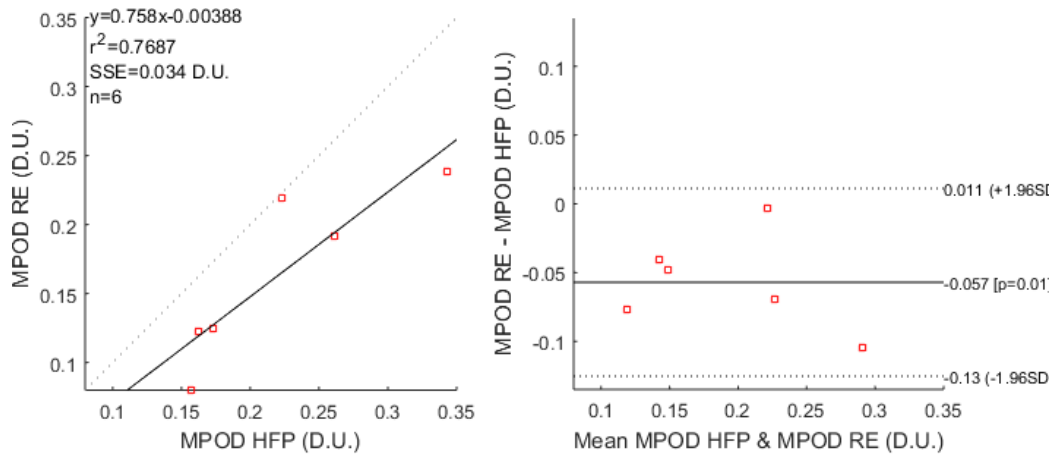


Figure 5.13: Comparison of the MPOD using the Reflectance method after scattering compensation and the HFP method.

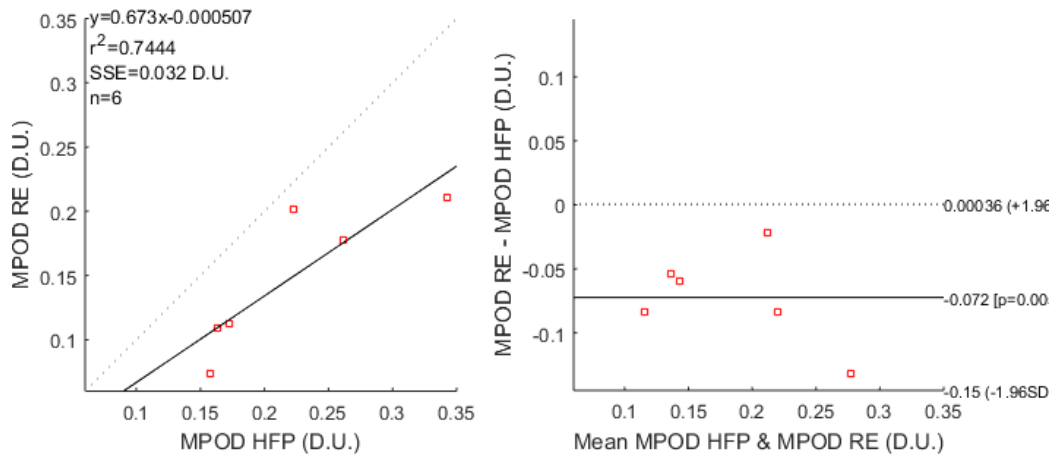


Figure 5.14: Comparison of the MPOD using the Reflectance method before scattering compensation and the HFP method.

The very small number of subjects tested does not allow for a more meticulous comparison of the two methods. However, the purpose of the HFP test was to validate the results and mainly test the correlation of the two methods rather than to extensively study the agreement between the two methods. From that respect, the RE method used for the measurement of the MPOD was indeed an accurate and consistent method. Moreover, it compensating the effect of scattering in the RE method improved its agreement with the psychophysical method.

Conclusions

The focus of this thesis was to investigate primarily how scattering in the ocular media in the fundus affect fundus reflectance measurements and visual psychophysical estimates. A number of experiments, both psychophysical and optical, were performed, and a theoretical fundus model was built for the study of straylight.

1. A theoretical model of the fundus was built - and light propagation under different conditions was simulated - using a Monte Carlo algorithm. The simulation revealed two things:
 - Based on physiological data on the amounts of choroidal melanin in the population, the simulation showed that, depending on the field size, fundus diffusion can lead to up to two times higher fundus reflectance at 650nm, whereas there was no significant effect at 550nm.
 - Light scattered at the ocular optics becomes dominant in the PSF for angles larger than about 2 degrees and 4 degrees at 550nm and at 650nm, respectively.
2. An optical setup was used for the study of fundus diffusion in reflectance measurements. Additionally, a LED-based psychophysical setup was built for the study of the effect of fundus diffusion in vision. The two devices were used to compare optical data for fundus diffusion and psychophysical data for color sensitivity in 6 subjects which formed two melanin pigmentation groups. Fundus diffusion is higher in subjects with less melanin pigmentation. However, its effect in vision is only observed under specific laboratory conditions and it is unlikely to have any practical relevance in vision.

3. An optical setup capable of acquiring fundus images at different eccentricities and wavelengths was built. Additional attention was given to avoid corneal and lens back-reflections. The system was based on the double pass principle and was capable of acquiring fundus images at various eccentricities and field sizes, and at 4 different wavelengths.
4. An algorithm for the reconstruction of the wide angle PSF at different wavelengths was developed, based on the integration technique.
5. Scattering in the optics of the eye exhibits a wavelength dependence for all eyes tested. It shows a minimum for medium wavelengths and a rise of similar magnitude for short and long wavelengths. For wavelengths in the NIR region, fundus diffusion is dominant even at very large angles, masking any effect from scattering in the ocular media.
6. It was verified quantitatively that the effect of scattering is increased for black letters on white backgrounds compared to white letters on black backgrounds. This result, though it might not have a practical consequence on a healthy subject, may affect vision tests for subjects with increased scattering in the optics, such as subjects with cataracts.
7. A complete algorithm for scattering compensation in fundus imaging was developed. For validation of the algorithm, the wide-angle PSF of a scattering filter in a single pass setup was successfully reconstructed, and consequently used to retrieve the original image. The same algorithm was applied on real fundus images. Two fundus images at 450nm and 550nm were acquired and the complete scattering compensation algorithm was applied to them. The original contrast of the fundus images that was reduced due to scattering was retrieved.
8. Based on the reflectometry technique using the optical system, the MPOD was measured and the effect of scattering in the measurement was quantified. The full procedure was applied for 7 subjects and an underestimation of about 10.2% on average was seen when scattering was not compensated.
9. The MPOD was also measured using the HFP method. When comparing the corrected MPOD from the reflectance method to the MPOD from the HFP method, the agreement is higher, which suggests that, while in the HFP method scattering has limited effect, it needs to be taken into account when measuring the MPOD using a reflectance method.

Bibliography

- U. E. Aladl, T. Peters, A. S. El-Baz, R. Acharya U, A. F. Laine, and J. S. Suri. Medical Image Registration. In *Multi Modality State-of-the-Art Medical Image Segmentation and Registration Methodologies*, pages 227–245. 2011.
- T. S. Aleman, J. L. Duncan, M. L. Bieber, E. De Castro, D. A. Marks, L. M. Gardner, J. D. Steinberg, A. V. Cideciyan, M. G. Maguire, and S. G. Jacobson. Macular pigment and lutein supplementation in retinitis pigmentosa and usher syndrome. *Investigative Ophthalmology & Visual Science*, 42(8):1873–1881, 2001.
- P. V. Algvere, J. Marshall, and S. Seregard. Age-related maculopathy and the impact of blue light hazard. *Acta Ophthalmologica Scandinavica*, 84(1):4–15, 2006.
- M. Alpern. Lack of uniformity in colour matching. *Journal of Physiology*, (288):85–105, 1979.
- P. Artal and J. Tabernerero. The eye’s aplanatic answer. *Nature photonics*, 2: 586–589, 2008.
- P. Artal, J. Santamaria, and J. Bescos. Retrieval of wave aberration of human eyes from actual point-spread-function data. *Journal of Optical Society of America A*, 5(8):1201–1206, 1988.
- P. Artal, I. Iglesias, N. López-Gil, and D. G. Green. Double-pass measurements of the retinal-image quality with unequal entrance and exit pupil sizes and the reversibility of the eye’s optical system. *Journal of the Optical Society of America A*, 12(10):2358–66, 1995a.
- P. Artal, S. Marcos, R. Navarro, and D. R. Williams. Odd aberrations and double-pass measurements of retinal image quality. *Journal of the Optical Society of America A*, 12(2):195–201, 1995b.

- P. Artal, A. Benito, G. M. Pérez, E. Alcón, A. De Casas, J. Pujol, and J. M. Marín. An objective scatter index based on double-pass retinal images of a point source to classify cataracts. *PloS one*, 6(2):e16823, 2011.
- P. Asbell and D. Brocks. Cornea Overview. In *Encyclopedia of the Eye*, pages 522–531. 2010.
- D. A. Atchison. Accommodation and presbyopia. *Ophthalmic and Physiological Optics*, 15(4):255–272, 1995.
- D. A. Atchison and G. Smith. *Optics of the Human Eye*. Butterworth-Heinemann, 2000.
- G. Aurell and H. Holmgren. On the metachromatic staining of the corneal tissue and some observations on its transparency. *Acta Ophthalmologica*, 31(1):1–27, 1953.
- S. Beatty, M. Boulton, D. Henson, H.-H. Koh, and I. J. Murray. Macular pigment and age related macular degeneration. *British Journal of Ophthalmology*, 83(83):867–877, 1999.
- S. Beatty, I. J. Murray, D. B. Henson, D. Carden, H. Koh, and M. E. Boulton. Macular pigment and risk for age-related macular degeneration in subjects from a Northern European population. *Investigative Ophthalmology & Visual Science*, 42:439–446, 2001.
- G. B. Benedek. Theory of transparency of the eye. *Applied Optics*, 10(3):459–73, 1971.
- G. B. Benedek. The molecular basis of cataract formation. *Ciba Found Symp*, 106:237–247, 1984.
- T. J. Berendschot, J. van de Kraats, and D. van Norren. Wavelength dependence of the Stiles-Crawford effect explained by perception of backscattered light from the choroid. *Journal of the Optical Society of America A*, 18(7):1445–51, 2001.
- T. T. J. M. Berendschot and D. van Norren. On the age dependency of the macular pigment optical density. *Experimental eye research*, 81(5):602–9, 2005.
- T. T. J. M. Berendschot, R. A. Goldbohm, W. A. A. Klopping, J. Van de Kraats, J. Van Norel, and D. Van Norren. Influence of lutein supplementation on macular pigment, assessed with two objective techniques. *Investigative Ophthalmology & Visual Science*, 41(11):3322–3326, 2000.

- T. T. J. M. Berendschot, P. J. DeLint, and D. van Norren. Fundus reflectance—historical and present ideas. *Progress in Retinal and Eye Research*, 22(2):171–200, 2003.
- T. T. J. M. Berendschot, J. van de Kraats, M. J. Kanis, and D. van Norren. Directional model analysis of the spectral reflection from the fovea and para-fovea. *Journal of Biomedical Optics*, 15(6):065005, 2010.
- F. A. Bettelheim. An interpretation of small-angle light-scattering patterns of human cornea. *Investigative Ophthalmology & Visual Science*, 16(3):233–236, 1977.
- J. M. Bland and D. G. Altman. Statistical methods for assessing agreement between two methods of clinical measurement. *Lancet*, 1(8476):307–310, 1986.
- D. Bok. The retinal pigment epithelium: a versatile partner in vision. *Journal of Cell Science. Supplement*, 17:189–195, 1993.
- R. A. Bone and J. T. Landrum. Heterochromatic flicker photometry. *Archives of Biochemistry and Biophysics*, 430:137–142, 2004.
- R. A. Bone and J. M. Sparrock. Comparison of macular pigment densities in human eyes. *Vision Research*, 11(10):1057–1064, 1971.
- R. A. Bone, J. T. Landrum, and S. L. Tarsis. Preliminary identification of the human macular pigment. *Vision Research*, 25(11):1531–1535, 1985.
- R. A. Bone, J. T. Landrum, L. Fernandez, and S. L. Tarsis. Analysis of the macular pigment by HPLC: Retinal distribution and age study. *Investigative Ophthalmology & Visual Science*, 29(6):843–849, 1988.
- R. A. Bone, J. T. Landrum, G. W. Hime, A. Cains, and J. Zamor. Stereochemistry of the human macular carotenoids. *Investigative Ophthalmology & Visual Science*, 34(6):2033–2040, 1993.
- C. Boote, S. Dennis, Y. Huang, A. J. Quantock, and K. M. Meek. Lamellar orientation in human cornea in relation to mechanical properties. *Journal of Structural Biology*, 149(1):1–6, 2005.
- G. D. Boreman and G. D. Boremann. *Modulation Transfer Function in Optical and Electro-Optical Systems*. SPIE Press, 2001.

- L. J. Bour, L. Koo, F. C. Delori, P. Apkarian, and A. B. Fulton. Fundus photography for measurement of macular pigment density distribution in children. *Investigative Ophthalmology & Visual Science*, 43(5):1450–1455, 2002.
- G. S. Brindley, J. J. DuCroz, and W. A. H. Rushton. The flicker fusion frequency of the blue-sensitive mechanism of colour vision. *Journal of Physiology*, (183):497–500, 1966.
- A. Bron, R. Tripathi, and B. Tripathi. *Wolff’s Anatomy of the Eye and Orbit*. Taylor & Francis, 8th edition, 1998.
- P. K. Brown and G. Wald. Visual Pigments in Human and Monkey Retinas. *Nature*, 200(4901):37–43, 1963.
- J. M. Bueno and P. Artal. Double-pass imaging polarimetry in the human eye. *Optics letters*, 24(1):64–66, 1999.
- S. a. Burns and a. E. Elsner. Color matching at high illuminances: the color-match-area effect and photopigment bleaching. *Journal of the Optical Society of America. A, Optics and image science*, 2(5):698–704, 1985.
- F. W. Campbell and R. W. Gubisch. Optical quality of the human eye. *The Journal of physiology*, 186(3):558–578, 1966.
- J. Carroll, J. Neitz, and M. Neitz. Estimates of L:M cone ratio from ERG flicker photometry and genetics. *Journal of Vision*, 2(8):531–542, 2002.
- W. N. Charman. The eye in focus: Accommodation and presbyopia. *Clinical and Experimental Optometry*, 91(3):207–225, 2008.
- S. S. Choi, N. Doble, J. L. Hardy, S. M. Jones, J. L. Keltner, S. S. Olivier, and J. S. Werner. In Vivo Imaging of the Photoreceptor Mosaic in Retinal Dystrophies and Correlations with Visual Function. *Investigative Ophthalmology & Visual Science*, 47(5):2080–2092, 2006.
- D. Christaras, H. Ginis, and P. Artal. Spatial properties of fundus reflectance and red – green relative spectral sensitivity. *Journal of the Optical Society of America A*, 32(9):1723–1728, 2015.
- N. J. Coletta, S. Marcos, C. Wildsoet, and D. Troilo. Double-Pass Measurement of Retinal Image Quality in the Chicken Eye. *Optometry and Vision Science*, 80(1):50–57, 2003.

- M. J. Costello, S. Johnsen, K. O. Gilliland, C. D. Freel, and W. C. Fowler. Predicted light scattering from particles observed in human age-related nuclear cataracts using mie scattering theory. *Investigative Ophthalmology & Visual Science*, 48(1):303–312, 2007.
- C. Darwin. *On the Origin of the Species*. John Murray, 1859.
- A. Daxer, K. Misof, B. Grabner, A. Ettl, and P. Fratzl. Collagen fibrils in the human corneal stroma: Structure and aging. *Investigative Ophthalmology & Visual Science*, 39(3):644–648, 1998.
- R. de Kinkelder, R. L. P. van der Veen, F. D. Verbaak, D. J. Faber, T. G. van Leeuwen, and T. T. J. M. Berendschot. Macular pigment optical density measurements: evaluation of a device using heterochromatic flicker photometry. *Eye (London, England)*, 25(1):105–112, 2011.
- S. S. Deeb, L. C. Diller, D. R. Williams, and D. M. Dacey. Interindividual and topographical variation of L:M cone ratios in monkey retinas. *Journal of the Optical Society of America A*, 17(3):538–544, 2000.
- P. J. Delint, T. T. Berendschot, and D. van Norren. Local photoreceptor alignment measured with a scanning laser ophthalmoscope. *Vision Research*, 37(2):243–248, 1997.
- F. C. Delori and K. P. Pflibsen. Spectral reflectance of the human ocular fundus. *Applied Optics*, 28(6):1061–1077, 1989.
- F. C. Delori, D. G. Goger, B. R. Hammond, D. M. Snodderly, and S. A. Burns. Macular pigment density measured by autofluorescence spectrometry : comparison with reflectometry and heterochromatic flicker photometry. *Journal of the Optical Society of America A*, 18(6):1212–1230, 2001.
- A. Dubra, Y. Sulai, J. L. Norris, R. F. Cooper, A. M. Dubis, D. R. Williams, and J. Carroll. Noninvasive imaging of the human rod photoreceptor mosaic using a confocal adaptive optics scanning ophthalmoscope. *Biomedical Optics Express*, 2(7):1864–1876, 2011.
- R. L. Easton. *Fourier Methods in Imaging*. Wiley, 1st edition, 2010. ISBN 9780470689837.
- A. Eisner and D. I. Macleod. Flicker photometric study of chromatic adaptation: selective suppression of cone inputs by colored backgrounds. *Journal of the Optical Society of America*, 71(6):705–717, 1981.

- R. A. Farrell, R. L. McCally, and P. E. Tatham. Wave-length dependencies of light scattering in normal and cold swollen rabbit corneas and their structural implications. *The Journal of Physiology*, 233:589–612, 1973.
- J. Feeney, C. Finucane, G. Savva, H. Cronin, S. Beatty, J. Nolan, and R. Kenny. Low macular pigment optical density is associated with lower cognitive performance in a large, population-based sample of older adults. *Neurobiol. Aging*, (34):2449–2456, 2013.
- E. J. Fernández, I. Iglesias, and P. Artal. Closed-loop adaptive optics in the human eye. *Optics Letters*, 26(10):746–748, 2001.
- E. J. Fernández, B. Hermann, A. Unterhuber, B. Považay, and W. Drexler. Adaptive optics with a magnetic deformable mirror : applications in the human eye. *Optics Express*, 14(20):631–643, 2006.
- M. Fippel and M. Soukup. A Monte Carlo dose calculation algorithm for proton therapy. *Medical physics*, 31(8):2263–2273, 2004.
- F. Flamant. Etude de la repartition de lumiere dans l’image retinienne d’une fente. *Revue d’Optique*, 34:433–459, 1955.
- V.-P. Gabel, R. Birngruber, and F. Hillenkamp. Visible and near infrared light absorption in pigment epithelium and choroid. *XXIII Concilium Ophthalmologicum*, (450):658–662, 1978.
- W. J. Geeraets, R. C. Williams, G. Chan, W. T. Ham, D. Guerry, and F. H. Schmidt. The Relative Absorption of Thermal Energy in Retina and Choroid. *Investigative Ophthalmology & Visual Science*, 1(3):340–347, 1962.
- K. O. Gilliland, C. D. Freil, C. W. Lane, W. C. Fowler, and M. J. Costello. Multilamellar bodies as potential scattering particles in human age-related nuclear cataracts. *Molecular vision*, 7:120–130, 2001.
- K. O. Gilliland, C. D. Freil, S. Johnsen, W. Craig Fowler, and M. J. Costello. Distribution, spherical structure and predicted Mie scattering of multilamellar bodies in human age-related nuclear cataracts. *Experimental Eye Research*, 79(4):563–576, 2004.
- H. Ginis, G. M. Pérez, J. M. Bueno, and P. Artal. The wide-angle point spread function of the human eye reconstructed by a new optical method. *Journal of Vision*, 12(3):1–10, 2012.

- H. Ginis, G. M. Perez, J. M. Bueno, A. Pennos, and P. Artal. Wavelength dependence of the ocular straylight. *Investigative Ophthalmology & Visual Science*, 54(5):3702–8, 2013.
- H. Ginis, O. Sahin, A. Pennos, and P. Artal. Compact optical integration instrument to measure intraocular straylight. *Biomedical Optics Express*, 5(9):3036, 2014.
- J. N. Goldman and G. B. Benedek. The relationship between morphology and transparency in the non-swelling corneal stroma of the shark. *Investigative Ophthalmology & Visual Science*, 6(6):574–600, 1967.
- M. A. Golshan, M. G. Tarei, M. A. Ansari, and A. Amjadi. The Propagation of Laser Light in Skin by Monte Carlo- Diffusion Method : A Fast and Accurate Method to Simulate Photon Migration in Biological Tissues Laser Propagation in Skin by Monte Carlo Diffusion Method. *Journal of lasers in medical sciences*, 2(3):109–114, 2011.
- J. M. Gorrard and F. C. Delori. Reflectance and curvature of the inner limiting membrane at the foveola. *Journal of the Optical Society of America A*, 16(6):1229–37, 1999.
- J. M. Gorrard, R. Alfieri, and J. Y. Boire. Diffusion of the retinal layers of the living human eye. *Vision Research*, 24(9):1097–1106, 1984.
- Y. Guo and J. Tan. Monte Carlo simulation of retinal light absorption by infants. *Journal of the Optical Society of America A*, 32(2):271–276, 2015.
- D. X. Hammer, R. D. Ferguson, J. C. Magill, M. a. White, A. E. Elsner, and R. H. Webb. Compact scanning laser ophthalmoscope with high-speed retinal tracker. *Applied Optics*, 42(22)Hammer, D.X. et al., 2003. Compact scanning laser ophthalmoscope with high-speed retinal tracker. *Applied Optics*, 42(22), pp.4621–4632. Available at: <http://www.ncbi.nlm.nih.gov/pubmed/15003161> [Accessed May 27, 2014].):4621–4632, 2003.
- M. Hammer, A. Roggan, D. Schweitzer, and G. Müller. Optical properties of ocular fundus tissues—an in vitro study using the double-integrating-sphere technique and inverse Monte Carlo simulation. *Physics in medicine and biology*, 40(6):963–978, 1995.
- B. R. Hammond, E. J. Johnson, R. M. Russell, N. I. Krinsky, K. J. Yeum, R. B. Edwards, and D. M. Snodderly. Dietary modification of human

- macular pigment density. *Investigative Ophthalmology & Visual Science*, 38(9):1795–1801, 1997a.
- B. R. Hammond, B. R. Wooten, and D. M. Snodderly. Individual variations in the spatial profile of human macular pigment. *Journal of the Optical Society of America A*, 14(6):1187–1196, 1997b.
- M. R. Hee, J. A. Izatt, E. A. Swanson, D. Huang, J. S. Schuman, C. P. Lin, C. A. Puliafito, and J. G. Fujimoto. Optical coherence tomography of the human retina. *Archives of ophthalmology*, 113(3):325–332, 1995.
- R. P. Hemenger. Small-angle intraocular light scatter: a hypothesis concerning its source. *J. Opt. Soc. Am. A*, 5(4):577–582, 1988.
- H. Hofer, L. Chen, G. Y. Yoon, B. Singer, Y. Yamauchi, and D. R. Williams. Improvement in retinal image quality with dynamic correction of the eye's aberrations. *Optics Express*, 8(11):631–643, 2001.
- H. Hofer, J. Carroll, J. Neitz, M. Neitz, and D. R. Williams. Organization of the human trichromatic cone mosaic. *The Journal of Neuroscience*, 25(42):9669–9679, 2005.
- L. L. Holladay. The fundamentals of glare and visibility. *Journal of the Optical Society of America*, 12:271, 1926.
- O. Howells, F. Eperjesi, and H. Bartlett. Measuring macular pigment optical density in vivo: A review of techniques. *Graefe's Archive for Clinical and Experimental Ophthalmology*, 249:315–347, 2011.
- O. Howells, F. Eperjesi, and H. Bartlett. Improving the repeatability of heterochromatic flicker photometry for measurement of macular pigment optical density. *Graefe's Archive for Clinical and Experimental Ophthalmology*, 251(3):871–80, 2013.
- ICNIRP. ICNIRP guidelines on limits of exposure to incoherent visible and infrared radiation. Technical Report 5, 2013.
- I. Iglesias, E. Berrio, and P. Artal. Estimates of the ocular wave aberration from pairs of double-pass retinal images. *Journal of the Optical Society of America A*, 15(9):2466–76, 1998.
- J. K. IJspeert, P. W. T. de Waard, T. J. T. P. van den Berg, and P. T. V. M. de Jong. The intraocular straylight function in 129 healthy volunteers; Dependence on angle, age and pigmentation. *Vision Research*, 30(5):699–707, 1990.

- J. K. Ijspeert, H. Spekreijse, P. W. T. de Waard, T. J. T. P. Van Den Berg, and H. Spekreijse. An improved mathematical description of the foveal visual point spread function with parameters for age, pupil size and pigmentation. *Vision Research*, 33(1):15–20, 1993.
- P. K. Kaiser and J. P. Comerford. Flicker photometry of equally bright lights. *Vision Research*, 15(12):1399–1402, 1975.
- A. Kienle and M. S. Patterson. Improved solutions of the steady-state and the time-resolved diffusion equations for reflectance from a semi-infinite turbid medium. *Journal of Optical Society of America A*, 14(1):246–254, 1997.
- M. Kirillin, I. Meglinski, V. Kuzmin, E. Sergeeva, and R. Myllylä. Simulation of optical coherence tomography images by Monte Carlo modeling based on polarization vector approach. *Optics Express*, 18(21):21714–24, 2010.
- K. Kirschfeld. Carotenoid pigments: their possible role in protecting against photooxidation in eyes and photoreceptor cells. *Proceedings of the Royal Society of London.*, 216(1202):71–85, 1982.
- C. C. W. Klaver, J. J. M. Assink, R. V. Leeuwen, R. C. W. Wolfs, J. R. Vingerling, T. Stijnen, A. Hofman, and P. T. V. M. D. Jong. Incidence and Progression Rates of Age-Related Maculopathy : The Rotterdam Study. *Investigative Ophthalmology & Visual Science*, 42(10):2237–2241, 2001.
- R. Klein, Q. Wang, B. E. K. Klein, S. E. Moss, and S. M. Meuer. The relationship of age-related maculopathy, cataract, and glaucoma to visual acuity. *Investigative Ophthalmology & Visual Science*, 36(1):182–191, 1995.
- R. Klein, B. E. K. Klein, and K. J. Cruickshanks. The prevalence of age-related maculopathy by geographic region and ethnicity. *Progress in Retinal and Eye Research*, 18(3):371–389, 1999.
- H. Knau, H. Jagle, and L. T. Sharpe. L/M cone ratios as a function of retinal eccentricity. *Color Research and Application*, 26:S128–S132, 2001.
- R. W. Knighton and X. R. Huang. Directional and spectral reflectance of the rat retinal nerve fiber layer. *Investigative Ophthalmology & Visual Science*, 40(3):639–47, 1999.
- R. W. Knighton, S. G. Jacobson, and C. M. Kemp. The spectral reflectance of the nerve fiber layer of the macaque retina. *Investigative Ophthalmology & Visual Science*, 30(11):2393–2402, 1989.

- E. V. Koblova, A. N. Bashkatov, E. a. Genina, V. V. Tuchin, and V. V. Bakutkin. Estimation of melanin content in iris of human eye. *Proceedings of SPIE*, 5688:302–311, 2005.
- J. F. Koretz, P. L. Kaufman, M. W. Neider, and P. A. Goeckner. Accommodation and presbyopia in the human eye—aging of the anterior segment. *Vision Research*, 29(12):1685–1692, 1989.
- A. M. Labin, S. K. Safuri, E. N. Ribak, and I. Perlman. Müller cells separate between wavelengths to improve day vision with minimal effect upon night vision. *Nature communications*, 5:4319, 2014.
- J. C. Lagarias, J. a. Reeds, M. H. Wright, and P. E. Wright. Convergence Properties of the Nelder–Mead Simplex Method in Low Dimensions. *SIAM Journal on Optimization*, 9(1):112–147, 1998.
- J. T. Landrum and R. A. Bone. Lutein, zeaxanthin, and the macular pigment. *Archives of biochemistry and biophysics*, 385(1):28–40, 2001.
- J. T. Landrum, R. A. Bone, H. Joa, M. D. Kilburn, L. L. Moore, and K. E. Sprague. A one year study of the macular pigment: the effect of 140 days of a lutein supplement. *Experimental eye research*, 65(1):57–62, 1997.
- P. Lennie, J. Pokorny, and V. C. Smith. Luminance. *Journal of Optical Society of America A*, 10(6):1283–1293, 1993.
- I. F. Leung. Macular pigment: new clinical methods of detection and the role of carotenoids in age-related macular degeneration. *Optometry*, 79:266–272, 2008.
- I. F. Leung, S. Caldarella, and D. M. Snodderly. The Repeatability of Macular Pigment Measurement Using Flicker Photometry. *Investigative Ophthalmology & Visual Science*, 44(13):406, 2003.
- E. Loane, C. Kelliher, S. Beatty, and J. M. Nolan. The rationale and evidence base for a protective role of macular pigment in age-related maculopathy. *The British journal of ophthalmology*, 92:1163–1168, 2008.
- N. López-Gil and P. Artal. Comparison of double-pass estimates of the retinal-image quality obtained with green and near-infrared light. *Journal of the Optical Society of America. A, Optics, image science, and vision*, 14(5):961–971, 1997.

- M. A. Losada and R. Navarro. Point spread function of the human eye obtained by a dual double-pass method. *Pure and Applied Optics*, 7(1): L7–L13, 1998.
- J. Loughman, M. C. Akkali, S. Beatty, G. Scanlon, P. A. Davison, V. O’Dwyer, T. Cantwell, P. Major, J. Stack, and J. M. Nolan. The relationship between macular pigment and visual performance. *Vision Research*, 50(13):1249–56, 2010a.
- J. Loughman, P. a. Davison, J. M. Nolan, M. C. Akkali, and S. Beatty. Macular pigment and its contribution to visual performance and experience. *Journal of Optometry*, 3(2):74–90, 2010b.
- J. Loughman, G. Scanlon, J. M. Nolan, V. O’Dwyer, and S. Beatty. An evaluation of a novel instrument for measuring macular pigment optical density: the MPS 9000. *Acta ophthalmologica*, 90(2):e90–7, 2012.
- S. Marcos, R. P. Tornow, A. E. Elsner, and R. Navarro. Foveal cone spacing and cone photopigment density difference: Objective measurements in the same subjects. *Vision Research*, 37(14):1909–1915, 1997.
- D. M. Maurice. The Structure and Transparency of the Cornea. *J. Physiol.*, 136:263–286, 1957.
- R. L. McCally, D. E. Freund, A. Zorn, J. Bonney-Ray, R. Grebe, Z. De La Cruz, and W. R. Green. Light-scattering and ultrastructure of healed penetrating corneal wounds. *Investigative Ophthalmology & Visual Science*, 48(1):157–165, 2007.
- K. M. Meek, D. W. Leonard, C. J. Connon, S. Dennis, and S. Khan. Transparency, swelling and scarring in the corneal stroma. *Eye (London, England)*, 17(8):927–936, 2003.
- N. Metropolis. The beginning of the Monte Carlo method. *Los Alamos Science*, 15:125–130, 1987.
- N. Metropolis and S. Ulam. The Monte Carlo method. *Journal of the American Statistical Association*, 44(2013):335–341, 1949.
- D. L. Nickla and J. Wallman. The multifunctional choroid. *Progress in Retinal and Eye Research*, 29(2):144–168, 2010.
- R. J. Noll. Zernike polynomials and atmospheric turbulence. *Journal of the Optical Society of America*, 66(3):207, 1976.

- A. O'Brien, C. Leahy, and C. Dainty. Imaging system to assess objectively the optical density of the macular pigment in vivo. *Applied Optics*, 52(25): 6201–6212, 2013.
- F. Orihuela-Espina, E. Claridge, and S. J. Preece. Histological parametric maps of the human ocular fundus : preliminary results. In *Medical Image Understanding and Analysis (MIUA)*, pages 133–136, 2003.
- N. Otsu. A threshold selection method from gray level histogram. *IEEE Transactions on Systems, Man, and Cybernetics*, 9:62–66, 1979.
- S. V. Patwardhan, A. P. Dhawan, and P. a. Relue. Monte Carlo simulation of light-tissue interaction: three-dimensional simulation for transillumination-based imaging of skin lesions. *IEEE transactions on biomedical engineering*, 52(7):1227–1236, 2005.
- J. Pokorny and V. C. Smith. Effect of field size on red–green color mixture equations. *Journal of the Optical Society of America*, 66(7):705–708, 1976.
- J. Pokorny, V. C. Smith, and S. J. Starr. Variability of color mixture data. II. The effect of viewing field size on the unit coordinates. *Vision Research*, 16(10):1095–1098, 1976.
- S. L. Polyak. *The Retina*. The University of Chicago Press, Chicago, Ill., 1941.
- S. J. Preece and E. Claridge. Monte Carlo modelling of the spectral reflectance of the human eye. *Physics in medicine and biology*, 47(16):2863–77, aug 2002.
- P. M. Prieto, J. S. McLellan, and S. A. Burns. Investigating the light absorption in a single pass through the photoreceptor layer by means of the lipofuscin fluorescence. *Vision Research*, 45(15):1957–1965.
- C. A. Puliafito, M. R. Hee, C. P. Lin, E. Reichel, J. S. Schuman, J. S. Duker, J. A. Izatt, E. A. Swanson, and J. G. Fujimoto. Imaging of Macular Diseases with Optical Coherence Tomography. *Ophthalmology*, 102(2): 217–229, 1995.
- S. Ramachandran, N. K. Taylor, A. I. McNaught, and A. R. Harvey. Modelling of light propagation in retinal tissue. *Progress in Biomedical Optics and Imaging - Proceedings of SPIE*, 5(30):48–60, 2004.
- F. Ratliff. *Visual Psychophysics and Physiology*. Elsevier, 1978.

- V. M. Reading and R. a. Weale. Macular pigment and chromatic aberration. *Journal of the Optical Society of America*, 64(2):231, 1974.
- A. Saad, M. Saab, and D. Gatinel. Repeatability of measurements with a double-pass system. *Journal of cataract and refractive surgery*, 36(1): 28–33, 2010.
- J. Santamaría, P. Artal, and J. Bescós. Determination of the point-spread function of human eyes using a hybrid optical-digital method. *Journal of the Optical Society of America. A, Optics and image science*, 4:1109–1114, 1987.
- I. Sechopoulos, S. Suryanarayanan, S. Vedantham, C. J. D’Orsi, and A. Karellas. Radiation Dose to Organs and Tissues from Mammography: Monte Carlo and Phantom Study. *Radiology*, 246(2):434–443, 2008.
- L. T. Sharpe, A. Stockman, H. Knau, and H. Jägle. Macular pigment densities derived from central and peripheral spectral sensitivity differences. *Vision Research*, 38(21):3233–3239, 1998.
- L. T. Sharpe, A. Stockman, W. Jagla, and H. Jägle. A luminous efficiency function, $V^*(\lambda)$, for daylight adaptation. *Journal of Vision*, 5(11): 948–968, 2005.
- C. R. Simpson, M. Kohl, M. Essenpreis, and M. Cope. Near-infrared optical properties of ex vivo human skin and subcutaneous tissues measured using the Monte Carlo inversion technique. *Physics in medicine and biology*, 43(9):2465–2478, 1998.
- G. Smith and D. A. Atchison. *The Eye and Visual Optical Instruments*. Cambridge University Press, 1997.
- D. M. Snodderly. Evidence for protection against age related macular degeneration by carotenoids and antioxidant vitamins. *American Journal of Clinical Nutrition*, 62:1448S–1261S, 1995.
- D. M. Snodderly. Macular Pigment Measurement by Heterochromatic Flicker Photometry in Older Subjects: The Carotenoids and Age-Related Eye Disease Study. *Investigative Ophthalmology & Visual Science*, 45(2):531–538, 2004.
- D. M. Snodderly, J. D. Auran, and F. C. Delori. The Macular Pigment II. Spatial Distribution in Primate Retinas. *Investigative Ophthalmology & Visual Science*, 25:674–685, 1984a.

- D. M. Snodderly, P. K. Brown, F. C. Delori, and J. D. Auran. The Macular Pigment. I. Absorbance spectra, localization, and discrimination from other yellow pigments in primate retinas. *Investigative Ophthalmology & Visual Science*, 25(6):660–673, 1984b.
- R. H. Steinberg. Interactions between the retinal pigment epithelium and the neural retina. *Documenta ophthalmologica. Advances in ophthalmology*, 60(4):327–346, 1985.
- W. S. Stiles. The Scattering Theory of the Effect of Glare on the Brightness Difference Threshold. *Proceedings of the Royal Society of London. Series B, Containing Papers of a Biological Character*, 105(735):131–146, 1929.
- W. S. Stiles. The Luminous Efficiency of Monochromatic Rays Entering the Eye Pupil at Different Points and a New Colour Effect. *Proceedings of the Royal Society B: Biological Sciences*, 123(830):90–118, 1937.
- A. Stockman and L. T. Sharpe. The spectral sensitivities of the middle- and long-wavelength-sensitive cones derived from measurements in observers of known genotype. *Vision Research*, 40(13):1711–1737, 2000.
- A. Stockman and L. T. Sharpe. Into the twilight zone: The complexities of mesopic vision and luminous efficiency. *Ophthalmic and Physiological Optics*, 26(3):225–239, 2006.
- A. Stockman, D. I. A. MacLeod, and J. A. Vivien. Isolation of the middle- and long-wavelength sensitive cones in normal trichromats. *Journal of the Optical Society of America A*, 10(12):2471–2490, 1993.
- A. Stockman, H. Jägle, M. Pirzer, and L. T. Sharpe. The dependence of luminous efficiency on chromatic adaptation. *Journal of Vision*, 8(16):1,1–26, 2008.
- H. Sun, J. Pokorny, and V. C. Smith. Control of the modulation of human photoreceptors. *Color Research & Application*, 26:S69–S75, 2001.
- J. S. L. Tan, J. J. Wang, V. Flood, E. Rochtchina, W. Smith, and P. Mitchell. Dietary Antioxidants and the Long-term Incidence of Age-Related Macular Degeneration. The Blue Mountains Eye Study. *Ophthalmology*, 115(2):334–341, 2008.
- K. Trier. The Sclera. *Advances in Organ Biology*, 10(05):353–373, 2006.

- C. Tsika, M. K. Tsilimbaris, M. Makridaki, G. Kontadakis, S. Plainis, and J. Moschandreas. Assessment of macular pigment optical density (MPOD) in patients with unilateral wet age-related macular degeneration (AMD). *Acta Ophthalmologica*, 89:1–6, 2011.
- S. Vaezy and J. I. Clark. A quantitative analysis of transparency in the human sclera and cornea using Fourier methods. *Journal of microscopy*, 163(Pt 1):85–94, 1991.
- H. C. Van De Hulst. *Light scattering by small particles*. Dover Publications Inc., 2003.
- J. van de Kraats, T. T. Berendschot, and D. van Norren. The pathways of light measured in fundus reflectometry. *Vision Research*, 36(15):2229–47, aug 1996.
- T. J. T. P. Van den Berg. On the relation between glare and straylight. *Documenta ophthalmologica. Advances in ophthalmology*, 78(3-4):177–181, 1991.
- T. J. T. P. Van Den Berg and J. K. Ijspeert. Light scattering in donor lenses. *Vision Research*, 35(1):169–177, 1995.
- T. J. T. P. Van den Berg, L. Franssen, and J. E. Coppens. Ocular Media Clarity and Straylight. *Encyclopedia of Eye*, 3:173–183, 2010.
- R. L. P. Van Der Veen, T. T. J. M. Berendschot, F. Hendrikse, D. Carden, M. Makridaki, and I. J. Murray. A new desktop instrument for measuring macular pigment optical density based on a novel technique for setting flicker thresholds. *Ophthalmic and Physiological Optics*, 29:127–137, 2009.
- R. L. P. van der Veen, T. T. J. M. Berendschot, M. Makridaki, F. Hendrikse, D. Carden, and I. J. Murray. Correspondence between retinal reflectometry and a flicker-based technique in the measurement of macular pigment spatial profiles. *Journal of Biomedical Optics*, 14(6):064046, 2009.
- E. J. van Kampen and W. Zijstra. Spectrophotometry of hemoglobin and hemoglobin derivatives. *Advances in clinical chemistry*, 23:199–257, 1983.
- R. Vishwanathan, A. Iannaccone, T. Scott, S. Kritchevsky, B. Jennings, G. Carboni, G. Forma, S. Satterfield, T. Harris, and K. Johnson. Macular pigment optical density is related to cognitive function in older people. *Age Aging*, (43):271–275, 2014.

- J. Vos and J. Boogaard. Contribution of the cornea to entoptic scatter. *Journal of the Optical Society of America*, 53(7):869–873, 1963.
- J. J. Vos. Disability glare - a state of the art report. *CIE*, 3(2):39–53, 1984.
- J. J. Vos and T. J. T. P. Van den Berg. On the course of the disability glare function and its attribution to components of ocular scatter. *CIE Collection on Colour and Vision*, 124, 1997.
- J. J. Vos and T. J. T. P. Van den Berg. Report on disability glare. *CIE Collection on Colour and Vision*, 135, 1999.
- G. Wagner and R. M. Boynton. Comparison of Four Methods of Heterochromatic Photometry. *Journal of the Optical Society of America*, 62(12):1508–1515, 1972.
- K. Wakamatsu, D. N. Hu, S. A. McCormick, and S. Ito. Characterization of melanin in human iridal and choroidal melanocytes from eyes with various colored irides. *Pigment Cell and Melanoma Research*, 21(1):97–105, 2008.
- L. Wang and S. L. Jacques. *Monte Carlo Modeling of Light Transport in Multi-layered Tissues in Standard C*. University of Texas M. D. Anderson Cancer Center, 1992.
- J. J. Weiter, F. C. Delori, G. L. Wing, and K. A. Fitch. Relationship of senile macular degeneration to ocular pigmentation. *American Journal of Ophthalmology*, 99(2):185–187, 1985.
- J. J. Weiter, F. C. Delori, G. L. Wing, and K. a. Fitch. Retinal pigment epithelial lipofuscin and melanin and choroidal melanin in human eyes. *Investigative Ophthalmology & Visual Science*, 27(2):145–52, 1986.
- W. M. Wells, P. Viola, H. Atsumi, S. Nakajima, and R. Kikinis. Multi-modal volume registration by maximization of mutual information. *Medical image analysis*, 1(1):35–51, 1996.
- J. S. Werner, S. K. Donnelly, and R. Kliegl. Aging and human macular pigment density. *Vision Research*, 27(2):257–268, 1987.
- J. S. Werner, M. L. Bieber, and B. E. Scheffrin. Senescence of foveal and parafoveal cone sensitivities and their relations to macular pigment density. *Journal of the Optical Society of America A*, 17(11):1918–1932, 2000.

- D. R. Williams, D. Brainard, M. McMahon, and R. Navarro. Comparison of noninvasive measures of the optical quality of the eye. In *Vision Science and its Applications*, volume 2, pages 68–71, 1994.
- B. R. Wooten and B. R. Hammond. Macular pigment: Influences on visual acuity and visibility. *Progress in Retinal and Eye Research*, 21(2):225–240, 2002.
- B. R. Wooten, B. R. Hammond, R. I. Land, and D. M. Snodderly. A practical method for measuring macular pigment optical density. *Investigative Ophthalmology & Visual Science*, 40(11):2481–2489, 1999.
- G. Wyszecki and W. S. Stiles. High-level trichromatic color matching and the pigment-bleaching hypothesis. *Vision Research*, 20(1):23–37, 1980.
- E. Yamada. Some structural features of the fovea centralis in the human retina. *Archives of ophthalmology*, 82(2):151–159, 1969.
- N. P. A. Zagers, J. van de Kraats, T. T. J. M. Berendschot, and D. van Norren. Simultaneous measurement of foveal spectral reflectance and cone-photoreceptor directionality. *Applied Optics*, 41(22):4686–4696, 2002.

Appendix A

Monte Carlo simulation

The input files used for the 4 different simulations can be seen below. Run 1 and Run 3 simulate light propagation in the fundus at 550nm and 650nm respectively, with the values extracted from Hammer et al. (1995). Run 2 and Run 4 simulate the same phenomenon at the same wavelengths with the choroidal absorption coefficient increased by a factor of 2, simulating an increase in the choroidal melanin for subjects with higher melanin pigmentation.

```
#####
# Input file for MCML.
# Lengths are in cm, mua and mus are in 1/cm.
#####
1.0 # version
4 # number of runs
#### RUN 1 #####
green.mco A # output file
10000000 # No. of photons
0.000115 0.001 # dz, dr [cm]
1000 350 30 # dz, dr, da
4 # Number of layers
#n mua mus g d
1.36 # n for medium above
1.47 4.5 310 0.97 0.02 # layer 1
1.47 1000 1200 0.84 0.001 # layer 2
1.47 230 800 0.94 0.025 # layer 3
1.47 4 910 0.9 0.07 # layer 4
1.36 # n for medium below
### RUN 2 #####
green2.mco A # output file
10000000 # No. of photons
```

```

0.000115    0.001          # dz, dr [cm]
1000      350 30          # No. of dz, dr, da.
4          # Number of layers
#n      mua      mus      g          d
1.36          # n for medium above
1.47      4.5      310      0.97    0.02    # layer 1
1.47      1000    1200    0.94    0.001   # layer 2
1.47      460     800     0.84    0.025   # layer 3
1.47      4      910     0.9     0.07    # layer 4
1.36          # n for medium below
#### RUN 3 #####
red.mco      A          # output file
10000000     # No. of photons
0.000115    0.001          # dz, dr [cm]
1000      350 30          # dz, dr, da
4          # Number of layers
#n      mua      mus      g          d
1.36          # n for medium above
1.47      1.5     250     0.97    0.02    # layer 1
1.47      530    1200    0.84    0.001   # layer 2
1.47      50     500     0.94    0.025   # layer 3
1.47      2      750     0.9     0.07    # layer 4
1.36          # n for medium below
#### RUN 4 #####
red2.mco     A          # output file name, ASCII.
10000000     # No. of photons
0.000115    0.001          # dz, dr [cm]
1000      350 30          # dz, dr, da.
4          # Number of layers
#n      mua      mus      g          d
1.36          # n for medium above
1.47      1.5     250     0.97    0.02    # layer 1
1.47      530    1200    0.84    0.001   # layer 2
1.47      100    500     0.94    0.025   # layer 3
1.47      2      750     0.9     0.07    # layer 4
1.36          # n for medium below

```

Camera calibration

For the optical setup, it was essential to have a precise measurement of the amount of captured light at low light conditions, rather than a fast, high resolution image. Therefore the camera needed primarily to be sensitive and to have a low signal to noise ratio and secondly to have a resolution that would allow us to identify retinal features such as blood vessels etc at the given magnification. The camera LUCA R camera (Andor, Belfast, Ireland) was chosen, which features a monochrome megapixel frame EMCCD sensor, with single photon detection sensitivity and unrestrained QE, with a maximum of 65% at about 600nm wavelength. The Quantum Efficiency¹, or else the camera's ability to capture photons, of the LUCA R with respect to wavelength is shown in fig. B.1.

Since fundus reflectance depends heavily on the wavelength, ranging from practically zero for shorter wavelengths at the fovea to up to 10% for longer wavelengths (Delori and Pflibsen, 1989), and with a large variability amongst individuals, meant that in order to have an adequate signal for all spectrum range, the exposure time for each measurement had to change accordingly. The first and most important thing therefore, was to calibrate the camera at different exposure times and investigate its linearity for all its dynamic range. The calibration was done as follows

1. The luminance in cd/m^2 of 25 levels of gray of a 191V Philips monitor (Philips INC) were measured, using the LS-100 (Konica Minolta) photometer. The different gray levels were presented using a MATLAB script. The monitor calibration is shown in fig. B.2.
2. Once the monitor was calibrated, the camera's response for different

¹as given by the manufacturer. Not tested in the present work since it wasn't necessary due to the calibration of the reflectance with a 99% white flat spectrum reflector.

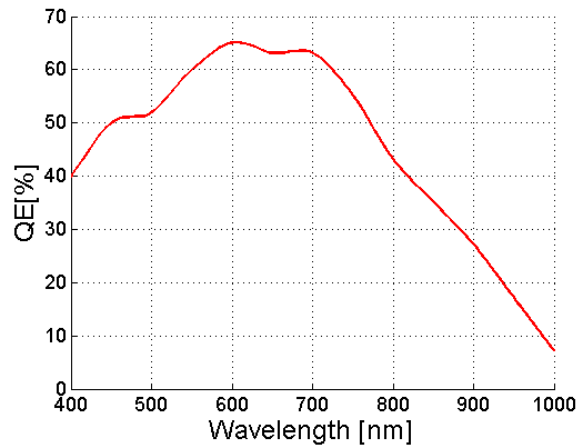


Figure B.1: Quantum Efficiency (QE) for LUCA R with respect to wavelength.

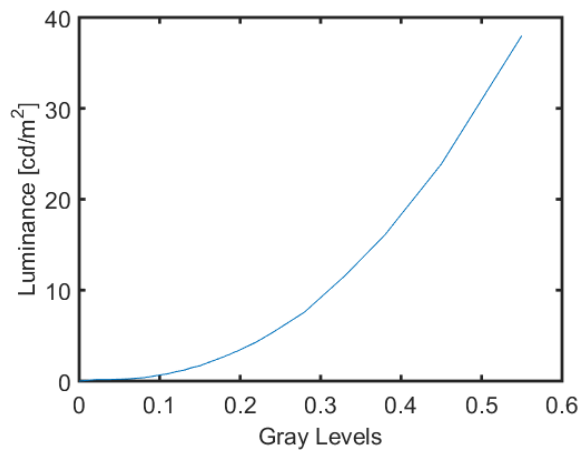


Figure B.2: Monitor luminance measured at a site against gray levels.

exposure times at luminance levels was recorded, using a MATLAB script. The monitor site used in both cases was the same.

3. A fit was performed for each exposure time and a luminance value was found for each camera pixel value. The fitting function was assumed to be piecewise: linear between 0 and the first luminance value and polynomial from the first luminance value and on. Overall, 15 fitting for 15 different exposure times were performed and 15 different sets of parameters were extracted. The function and the parameters were stored in a MATLAB function which took as arguments the exposure time and the pixel value as read by the camera and returned a luminance value. The fits for five different exposure times are shown in fig. B.3.

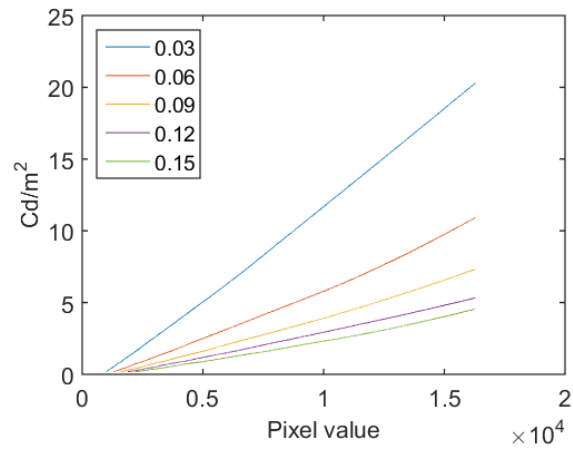


Figure B.3: Interpolation fits for 5 different exposure times.

The fitting function was chosen over a lookup table in order to minimize computation time.

Appendix C

Scripts

In this appendix, some of the scripts written throughout the thesis are shown. For more scripts contact the author.

C.1 Point Spread Function CIE simulation

MATLAB script for the simulation of the double pass PSF_{CIE} and the corresponding intensities (see chapter 4) for the different ages and pigmentation. The complete expression for the single pass PSF_{CIE} can be seen on 30.

```
%number of total pixels-points in our PSF
res=1023;
%Maximum angle of the PSF
maxTheta=20;
%create angle space
imageaxis=linspace(-maxTheta, maxTheta, res);
[x,y]=meshgrid(imageaxis,imageaxis);
radfield=hypot(x,y);
%pixel size in degrees
dpx=maxTheta/res;
%PSF CIE has 2 parameters - age and pigmentation
%The simulation will go for all ages from 0 to 120
%and three different pigmentations: 0, 0.5 and 1
age=0; %initial age
p=0; %initial pigmentation
stepnumber=22; %number of intensities to be created
%matching the ones measured experimentally
%create disks of increasing radius
ix=res;
iy=res;
cx=round(ix/2);
```

```

cy=round(iy/2);
iradius=linspace(0,6/dpx,stepnumber);
for icountsize=1:stepnumber
    [xx,yy] = ndgrid((1:ix)-cx,(1:iy)-cy);
    mask(icountsize, :, :) = (xx.^2 + yy.^2)<iradius(icountsize)^2;
    angle(icountsize)=iradius(icountsize)*dpx;
end
for i=1:120
    %single pass PSF CIE.
    spPSF2d=PSF_cie(radfield,age,p);
    %Autoconvolution for the double pass PSF
    spfour=fft2(spPSF2d);
    spfour2=spfour.*spfour;
    dpPSF2d=real(fftshift(iff2(spfour2)));
    %find the intensity at the center of the disk
    for icountsize=1:stepnumber
        intensities(icountsize)=sum(sum(mask.*dpPSF2d));
    end
    intensities=intensities/max(max(intensities));
    figure(1)
    plot(radfield(round(res/2),1:end),...
        log10(spPSF2d(round(res/2),:)), 'r')
    hold on
    plot(radfield(round(res/2),1:end),...
        log10(dpPSF2d(round(res/2),:)), 'g')
    figure(2)
    plot(angle,intensities)
    hold on
    age=age+1;
end

```

C.2 Diffraction-limited Modulation Transfer Function for square aperture

MATLAB script for the calculation of the Diffraction-limited MTF of a square aperture.

```

%Create frequency domain
nyquist=(1/4)*(res/maxangle);
freqaxis=linspace(-nyquist,nyquist,length(MTF));
[xf,yf]=meshgrid(freqaxis);
ksi=hypot(xf,yf); %frequency space
lambdamm=550*10^-6; %wavelength
Dapert=3.5 %aperture diameter
mm2va=2*rad2deg(atan(0.5/35)); %millimetres to degrees

```

```
ksi0=1/(lambdamm*35/Dapert)/mm2va; %cutoff frequency in cpd
MTFdiff=1-ksi/ksi0; %diff. limited PSF
```

C.3 Determination of the centroid of a fundus image

MATLAB script for the extraction of the centroid of a disk projected on the fundus. Threshold is provided by MATLAB's *graythresh* function, which uses Otsu's algorithm (Otsu, 1979).

```
function [centre,area]=findcentroid(im0,threshold)
%Script that finds centroid of an image
%scale image
im0=im0/max(max(im0));
normalizedThreshold = graythresh(im0)
figure(666);
imshow(im0);
waitforbuttonpress;
%turn to black and white.
BW = im2bw(im0, threshold);
%figure(667);
imshow(BW);
%discard small areas
BW = bwareaopen(BW,3000);
%fill gaps
BW = imfill(BW,'holes');
%find boundaries
[B,L] = bwboundaries(BW,'noholes');
%find area and centroid
stats = regionprops(L,'Area','Centroid')
area=stats(1).Area;
centre=round(stats(1).Centroid);
hold on
plot(centre(1),centre(2),'r+')
hold off
waitforbuttonpress;
end
```

C.4 Macular Pigment Optical Density using Heterochromatic Flicker Photometry

```

/*
Heterochromatic Flickering Photometry Arduino program for the
extraction of MPOD. A MATLAB wrapper was build for the interface
with the computer.
*/

int led1 = 5;
int led2 = 6;
char b;
char a;
int n;
//initialize Intensity and Duration
int Ints=150;
int Duration=16;
int DurStep=1;
int IntStep=5;
String fin=String(Ints);
unsigned long t0=0;
unsigned long t1;

void setup() {
  //Baud rate 9600
  Serial.begin(9600);
  Serial.println(fin);
  //Wait for communication with MATLAB
  while(Serial.available() == 0){
    b=Serial.read();
    delay(2);
  }
  // initialize the digital pin as an output and
  // test LEDs
  pinMode(led1, OUTPUT);
  pinMode(led2, OUTPUT);
  digitalWrite(led1,HIGH);
  delay(3000);
  digitalWrite(led1,LOW);
  digitalWrite(led2,HIGH);
  delay(3000);
  digitalWrite(led2,LOW);
}

// the actual loop (the equivalent to C's main):
void loop() {
  //t0=micros();
  if (Serial.available() > 0) {
    a=Serial.read();
    if (a=='r')
    {

```

```
    Ints=Ints+IntStep;
  }
  else if (a=='l')
  {
    Ints=Ints-IntStep;
  }
  else if (a=='u')
  {
    Duration=Duration-DurStep;
  }
  else if (a=='d')
  {
    Duration=Duration+DurStep;
  }
}
analogWrite(led1,255);
delay(Duration);
analogWrite(led1,0);
analogWrite(led2,Ints);
delay(Duration);
analogWrite(led2,0);
//t1=micros()-t0;          // uncomment this to measure
                          // the time of one period
//Serial.println(t1);
}
```


Appendix **D**

Pulse Width Modulation with the Arduino

The Arduino microcontroller provides solely digital outputs and does not have the capability of providing real analog pulses in the traditional sense. Although this might seem as a serious defect of the device, when it comes to LEDs analog pulses are not recommended due to the fact that LEDs do not behave linearly with voltage, causing color shifts and dropouts. So even if the microprocessor was capable of providing variable voltage output, it would still be unsuitable for LED driving. Nevertheless, there is a workaround that one could do in order to fake analog output without altering the voltage: the Pulse Width Modulation (PWM) technique. The principle of operation of the PWM technique is to adjust the proportion of ON time to OFF time over a specific time interval. Changing the ON to OFF time, or else the Duty cycle, within a specific period, one can produce an pseudo-analog pulse which, when driving an LED, can be perceived as dimming. The output voltage will then be given according to the formula

$$V_{out} = \frac{T_{ON}}{T_{OFF}} * V_{max} \quad (D.1)$$

An example of simulating a voltage using PWM is shown in fig. D.1.

In order for this flickering, not to be perceived, the PWM frequency needs to be high enough so that it is below the temporal summation threshold of the visual system, but low enough in order of the electronics to pick. The Arduino microcontroller UNO, based on the Atmega328 chip, uses three different timers, two with a base frequency of 31.250kHz and one with 62.500kHz, for 8-bit resolution. Each of these three timers has a prescaler that generates the

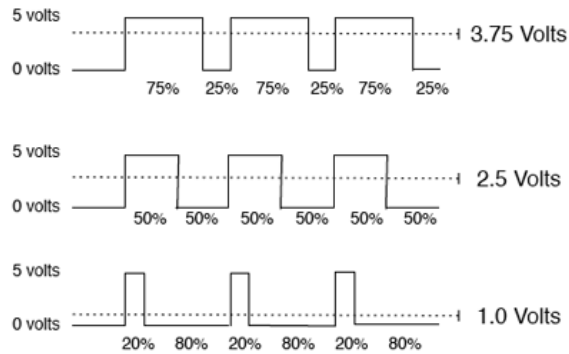


Figure D.1: Pulse Width Modulation example: Simulation of 3 different voltage values using different duty cycles.

timer clock by dividing the base frequency by a specific factor¹. Depending on the prescaler and the dimming "resolution" one wants to achieve, the controller can give up to 100.000 times higher PWM frequency of what the visual system is capable of summing. Assuming that a relatively fast LED driver has a rise time at the range of μs , for a PWM frequency of about 1kHz, which is the default value provided by Arduino UNO for pins 5 and 6, the shortest pulse for 8-bit time resolution would be less than $5\mu s$.

There is a very direct way to control the PWM frequency of a specific pin on the Arduino. In order to do so, one simply needs to alter the value of the prescalers. This will also affect the behavior of the `delay()` and `millis()` function since there are controlled by the same clock. For the needs of our experiment and after performing some preliminary tests with different frequencies, Arduino's pins 5 and 6 were finally used which have a default prescaler of 64, giving a cycle frequency of about 1kHz.

¹In reality, the Arduino usually has a system clock frequency of 16MHz. This in practice means that one could sacrifice resolution to increase frequency, reaching values upto 8MHz for 1-bit

Acknowledgments

A few pages for acknowledgments at the end of my thesis are surely not enough to express my gratitude to all those who have helped me for its realization. If I had to fairly attribute the contribution of all those involved directly or indirectly in this thesis, the acknowledgments would be as long as the thesis itself, and even then, I wouldn't be able to find the right words.

That being said, the first person I would like to thank is my supervisor and mentor Pablo Artal. Pablo gave me the freedom to explore on my own, and a hand to recover when my steps faltered. He taught me how to think as an independent scientist, to take risks and try new ideas but always stay focused on the objective. Having a natural tendency for "scattering", I am sure it took a lot of patient and effort to keep me on the right track. I could not have imagined having a better adviser.

I am glad to have had the opportunity to work under Haris Ginis, co-supervisor of this thesis and my role model in science. It was a pleasure to work with this all-around scientist with a deep knowledge of his field -and almost every field of physics, a remarkable scientific integrity, and above all a great teacher.

I can't thank enough my friend and colleague Alexandros Pennos. He stood for me both academically and personally and I would never have done it without him. Alex has the unique ability to give the best piece of advice when you most need it, and having him as a friend proved to be extremely handy when my project -or life- wasn't going as planned. I am also grateful to Alex's partner and my friend Kleoniki Chaidaki for putting up with me during my last month in Murcia.

Special thanks to all LOUM members that made those four years exciting and stimulating. The 11 o'clock coffee break had always been the highlight of my day. In particular I would like to thank Juan Tabernero Silvestre Manzanera, Christina Schwarz, Pedro Prieto, Josua Fernandez, Eloy Ville-

gas, Lucia Hervella, Andrian Gambin, Carmen Martinez, Juan Mompean, Benjamin Lochocki, Fran Avila, Alejandro Mira and Antonio Benito. They have all helped me greatly, each one of them in a different way. Special mention to Esther Berrio for her motivation and her advice especially during the stressful last months, Astrid Duque, who helped me during my first days in Spain, and Juan M. Bueno for all his help with the thesis paperwork especially in the beginning. It goes without saying that the contribution of my fellow PhDs, Manu Chirre and Martin Skorsetz and Augusto Arias, was detrimental. Their input and help was really important and it was great having them around. Above all, I want to thank them for all the fun we had in and out of LOUM.

It would be unfair not to mention Bart Jaeken and Luis Blanco from Voptica. Special thanks to Guillermo Perez for his extremely important input during this project.

Throughout these years, a number of people came to the lab and, although they only stayed for a short period, they became a vital part of the every day life of the lab. I would like to thank Eva Acosta, the great Kazuhiko Ohnuma, Alexandru Iosif and Geovanni Hernandez.

I would like to acknowledge Susana Marcos and her group at the Visual Optics and Biophotonics Lab for the great time I had during my short visit to her lab. Special thanks to Aiswaryah Radhakrishnan for the warm welcome and extensive lab tour.

I would also like to acknowledge Linda Lundstrom and Simon Winter for having me at KTH in Stockholm. I learned a lot during my short stay there.

I am also deeply indebted to Onurcan Sahin from the University of Crete for his help on my project but also for making the conferences fun. I just need to remember to bring earplugs to the next conference!

I am also grateful to the European commission for funding me as part of the Marie Curie ITN OpAl network, and particularly to Frank Schaeffel, Sigrid Diether and Michaela Bitzer for putting all this together. A Marie Curie scholarship is by no means an ordinary scholarship. It truly reflects the very essence of the European Union, the open borders, the collaboration between different institutions and it promotes perfectly the founding values of the EU.

Special thanks to all of my fellow Marie Curie researchers Ulrich Wildenmann, Yohann Benard, Mengchan Sun, Yun Chen, Mohammad Fathi and Abinaya Priya Venkataraman for all the fun we had at the meetings.

From my life outside the lab, there have been many people who helped me in various ways. Jason Blair, my first friend in Murcia and one of my closest friends, is one of them. I am thankful for the numerous discussions (most of them scientific) over *tapa y caña*. Special mention to my dear

friend Sarah Heath Howe for putting up with me and my constant moaning. I am particularly grateful to Giannis Ntalianis, one of my oldest friends, for helping me stay sane through these intense years. Additional thanks to them for wasting their time looking for typos and ambiguities in the manuscript.

I also need to thank the entire GB team Murcia and particularly Kike for all the amazing time we had. Finally, I thank James, Akis, Kostas, Nikolas, Antonis, Myrsini, Voula and every single one of my friends for their help and support.

Special thanks to my cousin Vaggelis Siminos, fellow physicist, who's academic steps I have been trying hard to follow. I am grateful for his overall advice and his comments on the thesis.

I would also like to thank Makis and Lida, my godparents and mentors. Every time I took an academy step, I always consulted with them first.

Finally, none of this would have been possible without the unconditional love and support of my parents Stella and Giorgos, and my brother Vasilis. This thesis belongs to them as much as it belongs to me. With them, a simple *ευχαριστω* will be more than enough.

So long, and thanks for all the fish.